TÜRK-ALMAN ÜNİVERSİTESİ
TÜRKISCH-DEUTSCHE UNIVERSITÄT

ENERGY CALCULATIONS 2020

PROCEEDINGS OF INTERNATIONAL 2ND CONFERENCE ON SUSTAINABLE ENERGY AND ENERGY CALCULATIONS 2020

Editor Şahin Uyaver

PUBLICATIONS OF
TURKISH-GERMAN UNIVERSITY

ICSEEC: Sustainable Energy and Energy Calculations
Proceedings of International Conference on Sustainable Energy and Energy Calculations
Organized by Turkish-German University, Beykoz, Istanbul, Turkey

Online Conference Dates: 4-5 September 2020

Editor:
Sahin Uyaver

Book Cover Design: Turkish-German University, Press and Public Relations Office
Published by: Turkish-German University
www.tau.edu.tr
Sahinkaya Cad. No: 86 34820 Beykoz, Istanbul, Turkey
October 2020

ISBN: 978-605-65842-3-7
DOI: 10.5281/zenodo.4084573

Organized by

TÜRK-ALMAN ÜNİVERSİTESİ
TÜRKISCH-DEUTSCHE UNIVERSITÄT

Turkish-German University
Department of Energy Science and Technologies
Beykoz, Istanbul, Turkey

PREFACE

This book highlights some of the latest advances in the fields of energy materials, energy issues in biophysical systems, sustainable energy and energy calculations. It features contributions presented at the International 2nd Conference on Sustainable Energy and Energy Calculations (ICSEEC2020), which was held on September 4-5 2020, as an online international conference, and was organized by the department of Energy Science and Technologies of Turkish - German University, Istanbul, Turkey. Many researchers from Turkey and abroad shared their knowledge and key findings on the energy technologies, energy materials and so on. The research papers of the book have been reviewed by the scientific committee of the conference.

We appreciate all the individual works.

Best Regards,

The Editorial Board
Istanbul, Turkey October 2020

Contents

Investigation of Burhaniye Wind Energy Potential

Asiye Aslan
aaslan@bandirma.edu.tr, Department of Electricity and Energy, Bandirma Onyedi Eylul University, Balikesir, Turkey

Abstract

With the growing population and developing industry, increasing energy need every day has brought the search for energy that is less likely to be exhausted and environmentally safe in its train. Today, wind energy, which is an alternative energy source, has gained importance. Balikesir province takes place in the top in the wind energy field in Turkey. Many power plants have been established in the province and continue to be established. In this study, after giving information about wind energy potential and production in Turkey, wind energy potential of Burhaniye, one of Balikesir's districts, was investigated. By analysing wind data, monthly speed and direction distribution were investigated in detail. Wind power density was received monthly. Weibull parameters and wind speed data for different heights were calculated using the extrapolation method. Data of 2011-2018 years taken from the Turkish State Meteorological Service were used. Annual average wind speed was obtained as 2.80 m/s and wind power density was 32 W/m^2. The region was determined as a poor location according to the classification made in terms of power potential.

Keywords: Burhaniye, renewable energy, wind energy.

Introduction

Fossil fuels, renewable energy, and nuclear power are three different categories of energy sources. Renewable energy can never get exhausted because it is constantly renewed. Moreover, it can be directly used or converted into other forms of energy. Wind energy is the most widely used renewable energy source [1–3].

One of the most widely used renewable energy sources is wind energy in Turkey. According to the Turkish State Meteorological Service's data, when wind speeds of 6.5 m/s and above are evaluated, it is known that the land wind potential is 131 756,4 MW and sea wind potential 17 393,2 MW in Turkey. In order for wind turbine power plants to be economic investments, the average wind speed at a height of 50 m on the land where the turbine will be installed should be minimum 7 m/s. Therefore, when land wind potential of Turkey at 7 m/s and above, it is seen that Turkey's land wind potential is 48 000 MW and sea wind potential is

5300 MW [4]. In 2019, the total capacity reached 8056 MWh with an increase of 9.32%.

Balikesir province is one of the most important production centres in Turkey. Nearly 19% of the wind energy investments in Turkey is made in Balikesir. All of these investments are active and have an installed power capacity of 969,75 MW. The total installed power capacity of wind energy investment under construction is 97,4 MW and this value represents 65% of the wind energy investments under construction in Turkey. The total area for the wind power plant that can be installed is approximately 3000 km^2. Total installed power capacity that can be installed was determined as approximately 14 000 MW [5].

Burhaniye is a district of Balikesir province on the Aegean Sea coast. Located in the Aegean Region, the district is located in the Edremit Gulf region, between Kazdagi in the north and Madra Mountain in the south. The district center and the north of the district are located to the south of the Edremit Coastal Plain. The rest of the district is on the north of Madra Mountain and on the low hills of the mountain extending towards the sea. Baglar headland on the shore is the southwestern border of the district. In this study, Burhaniye wind energy potential was investigated. Wind speed, wind direction and wind power values were determined monthly using 2011-2018 data and presented graphically. The region was determined as a poor location according to the classification made in terms of power potential.

Materials And Methods

Wind Data Analysis. The hourly wind speed data from 2011 to 2018 was obtained from the Turkish State Meteorological Service, Burhaniye Station. At this meteorological station, wind speeds are measured using a cup anemometer at a height of 10 m above ground level. The station is located at 39°49' N and 26°97' E.

Weibull Distribution of Wind Speed. The most common density function that are used to describe the wind speed data is the Weibull function. The Weibull function is a special case of the generalized gamma distribution and it is a two parameter distribution [6].

The Weibull distribution function can be described as;

$$f_w(\nu) = \frac{k}{c}\left(\frac{\nu}{c}\right)^{k-1} e^{-\left(\frac{\nu}{c}\right)^k} \tag{1}$$

where v is the wind speed, c is a Weibull scale parameter and k is a dimensionless Weibull shape parameter. The cumulative probability function of the Weibull distribution is given as follows [7,8].

$$F_w(v) = 1 - e^{-\left(\frac{\nu}{c}\right)^k} \tag{2}$$

Over the last few years, numerous methods have been offered in order to estimate Weibull k and c parameters. In this study, mean wind speed-standard deviation method has been used to determine the two parameters [9–11]. In this method, Weibull factors can be obtained by using the following formulas:

$$k = \left(\frac{\sigma}{\nu_m}\right)^{-1{,}086} \quad 1 \le k \le 10 \tag{3}$$

$$c = \frac{\nu_m}{\Gamma(1 + 1/k)} \tag{4}$$

where v_m and σ are mean wind speed and standard deviation of the wind speed for any specified periods of time, respectively and can be calculated by using the following formulas:

$$\nu_m = \frac{1}{n}\left[\sum_{i=1}^{n} \nu_i\right] \tag{5}$$

$$\sigma = \left[\frac{1}{n-1}\sum_{i=1}^{n}(\nu_i - \nu_m)^2\right]^{1/2} \tag{6}$$

And also γ(x) is the gamma function and is defined as follows:

$$\Gamma(x) = \int_0^\infty e^{-u}u^{x-1}dx \tag{7}$$

The most probable wind speed and the wind speed carrying maximum energy can be easily obtained by calculating the scale and shape parameter. The most probable wind speed denotes the most frequent wind speed for a given wind probability distribution and is formulated by [11, 12]:

$$V_{MP} = \left(1 - \frac{1}{k}\right)^{\frac{1}{k}} \tag{8}$$

The wind speed carrying maximum energy represents wind speed which carries maximum amount of wind energy and can be formulated as follows [11, 12]:

$$V_{ME} = c\left(1 + \frac{2}{k}\right)^{\frac{1}{k}} \tag{9}$$

Wind Power Density. The wind power density per unit area is calculated by:

$$P = \frac{1}{2}\rho\nu^3(W/m^2) \tag{10}$$

where ρ is the density of air at sea level with mean temperature of 15 °C and 1 atmospheric pressure that is 1225 kg/m^3 depending on altitude, air pressure and temperature [13]. The wind power density using Weibull probability density function can be calculated as follows [12]:

$$\frac{P}{A} = \frac{1}{2}\rho\int_0^\infty \nu^3 f_w(\nu)d\nu = \frac{1}{2}\rho c^3\Gamma\left(1 + \frac{3}{k}\right) \tag{11}$$

Extrapolation of Wind Data. If the Weibull parameters are known for a particular height, the following equations can be used to estimate the Weibull parameter for different heights at the same location [14];

$$k_h = k_o \left[1 - 0.088 \ln\left(\frac{h_o}{10}\right)\right] / \left[1 - 0.088 \ln\left(\frac{h}{10}\right)\right] \tag{12}$$

$$c_h = c_o \left(\frac{h}{h_o}\right)^n \tag{13}$$

where c_o is Weibull scale parameter and k_o is shape parameter at known h_o The exponent n can be computed as;

$$n = [0.37 - 0.088 \ln(c_o)] / \left[1 - 0.088 \ln\left(\frac{h}{10}\right)\right] \tag{14}$$

Results and Discussion

In this study, wind energy potential was determined by using the data measured at Burhaniye meteorology station. In Figure 1, monthly distribution of 8-years average wind speed of Burhaniye station between 2011-2018 is given. While the highest average speed was obtained in August at 3.8 m/s in 2011, the lowest speed was obtained in November at 2 m/s in 2017. In Figure 2, 8-years average wind speed seasonal distribution between 2011-2018 is given. While the highest average speed was obtained in Summer season with 3.29 m/s in 2013, the lowest speed was obtained in Autumn season with 2.40 m/s in 2017.

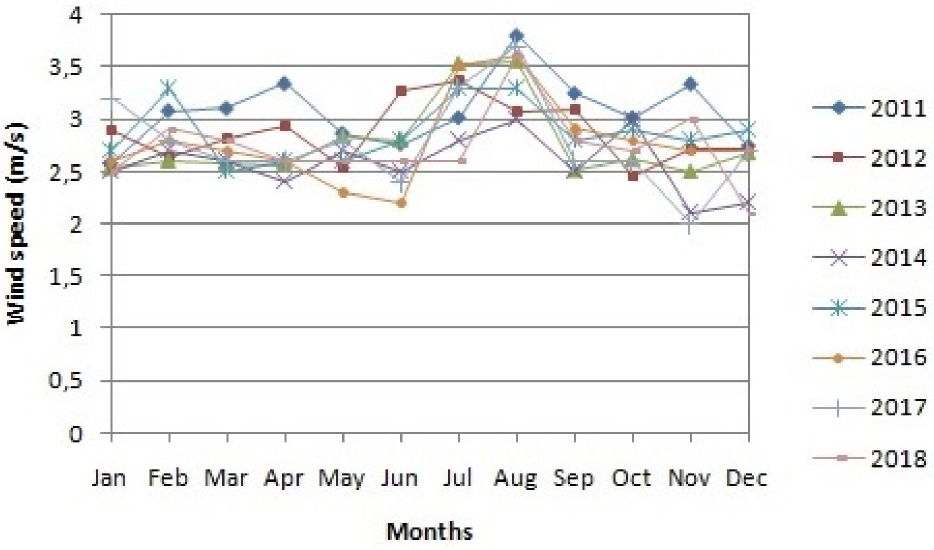

Figure 1: Monthly variation of the mean wind speed.

In Figure 3, 8-years average wind speed daily distribution between 2011-2018 is separately given for each month. In the figures, it is observed that the wind speeds start to increase after 7:00 o'clock, get the maximum value between 11:00 and 15:00

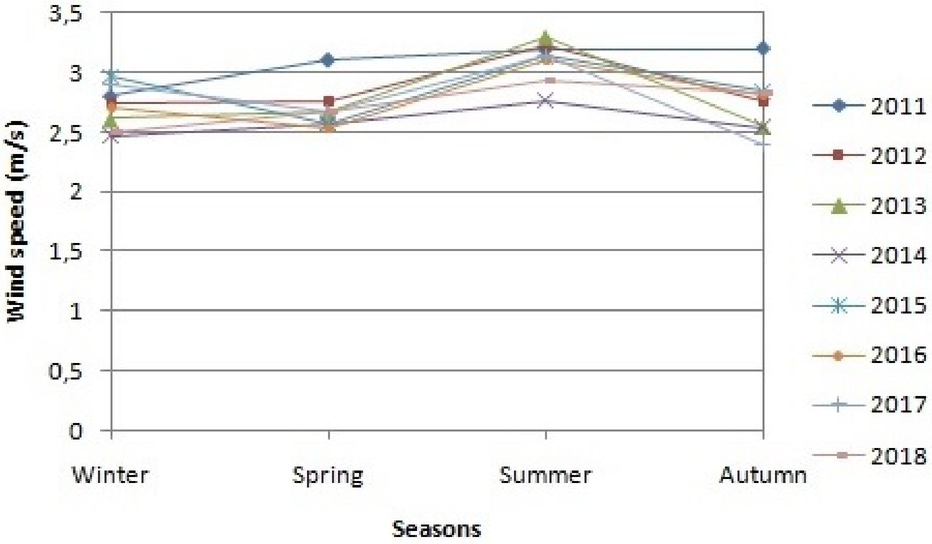

Figure 2: Seasonal variations of the mean wind speed.

o'clock and then decrease again towards the end of the day. While the maximum average wind speed is obtained at 4.00 m/s in July at 14:00, the minimum average wind speed is obtained at 1.73 m/s in March at 21:00. When assessing the wind-energy potential, wind direction is as important a factor as wind speed. In Figure 4, wind direction distributions of Burhaniye station are shown monthly.

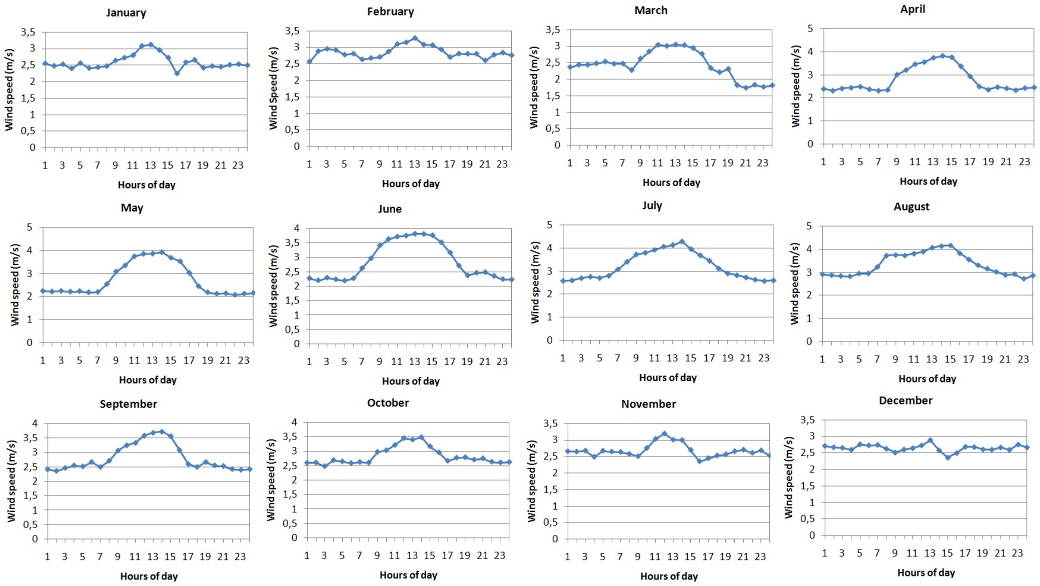

Figure 3: Wind speed profile by months.

The prevailing wind directions were as follows: 19% ENE (67.5°) and 16% ESE (122.5°) at January, 21% ENE (67.5°) and 19% NE (45°) at February, 15% ENE (67.5°) and 15% NE (45°) at March, 14% ESE (270°) and 12% ENE (67.5°) at April, 14% ENE (67.5°) and 12% NE (45°) at May, 20% ENE (67.5°) and 15% NE (45°) at June, 25% NE (45°) and 24% ENE (67.5°) at July, 33% ENE (67.5°)

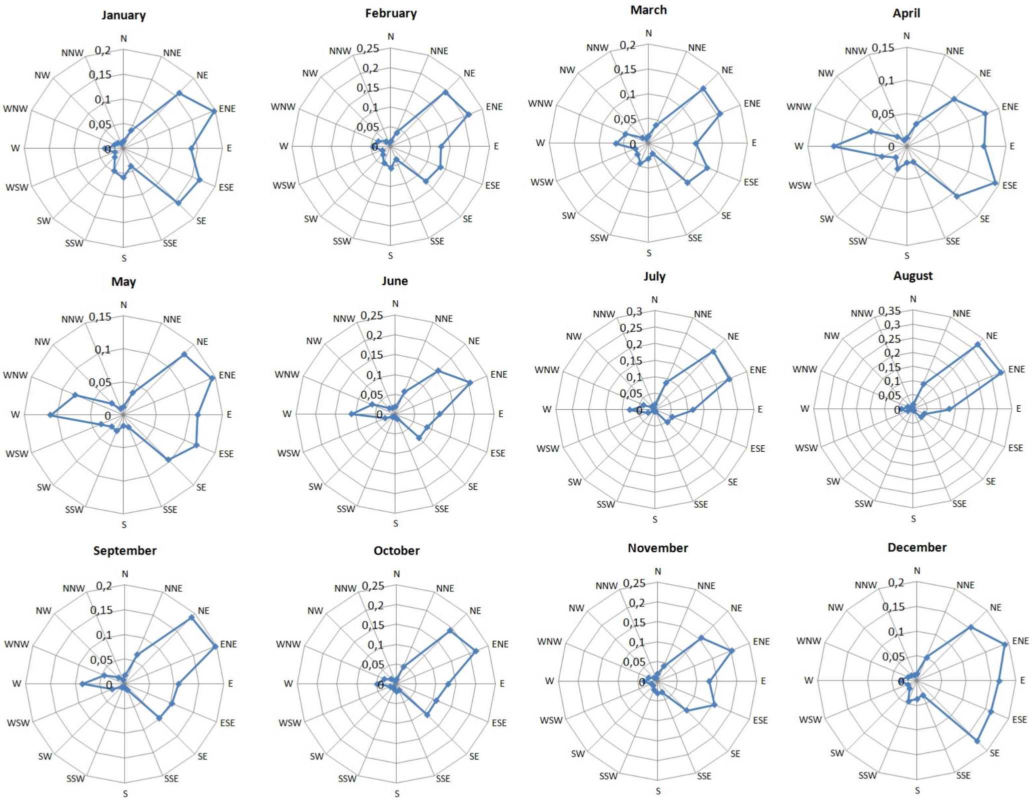

Figure 4: Wind frequency roses.

and 32% NE (45°) at August, 19% ENE (67.5°) and 18% NE (45°) at September, 21% ENE (67.5°) and 19% NE (45°) at October, 20% ENE (67.5°) and 15% NE (45°) at November, 19% ENE (67.5°) and 16% E (90°) at December. In all months, the prevailing wind directions are mainly ENE (67.5°) and NE (45°), whereas the weakest wind directions are N (0°) and S (180°).

In Figure 5, monthly average wind power density values obtained from wind speed data are given. It can be seen in the figure that the highest power density values were obtained in parallel with the highest wind speed values in August. This is followed by the months of February and July. The lowest value was obtained in March.

Table 1 shows the monthly wind speed and Weibull parameters according to the 2011-2018 average. The highest monthly average wind speed was obtained as 3.45 m/s at August. The power density was obtained as 32.2 W/m^2 in August. Wind speed and Weibull parameters for different heights were calculated using the method of extrapolation and are given in Table 2.

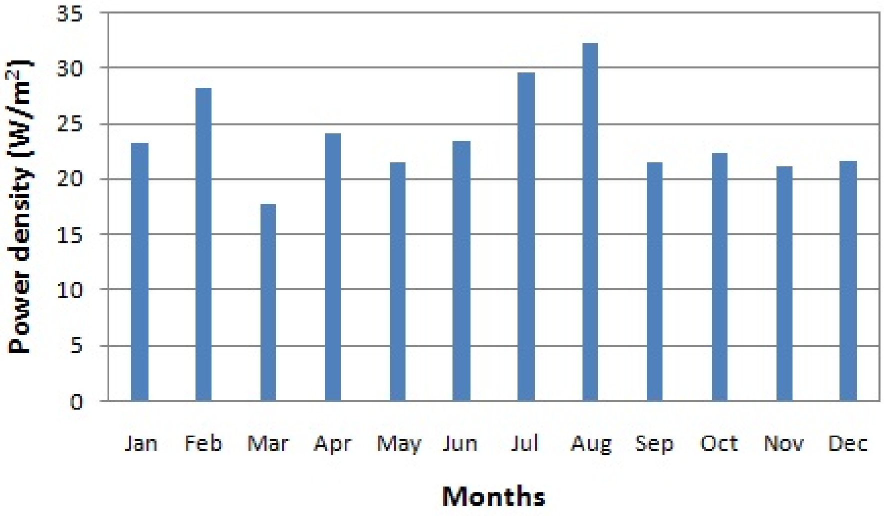

Figure 5: Annual variations of the mean wind power density in Burhaniye.

Table 1: Wind speed and Weibull parameters at between 2011-2018.

Months	$\nu(m/s)$	k	c (m/s)	P(W/m^2)	V_{MP}	V_{ME}
Jan	2.68	1.76	2.91	23	1.81	4.47
Feb	2.85	1.88	3.18	28	2.13	4.68
Mar	2.71	1.96	2.79	17	1.94	3.99
Apr	2.70	2.09	3.13	24	2.29	4.32
May	2.75	2.12	3.05	21	2.26	4.17
Jun	2.66	2.50	3.21	23	2.62	4.07
Jul	3.17	2.81	3.62	29	3.09	4.38
Aug	3.45	3.05	3.76	32	3.30	4.43
Sep	2.80	2.52	3.17	21	2.59	4.00
Oct	2.76	2.46	3.20	22	2.59	4.07
Nov	2.64	2.11	3.01	21	2.22	4.13
Dec	2.59	1.97	2.97	21	2.07	4.23

Table 2: Wind speed and Weibull parameters at different heights.

Heights	$\nu(m/s)$	k	c (m/s)	P(W/m^2)	V_{MP}	V_{ME}
10	2.80	1.73	3.24	32	1.97	5.04
20	3.47	1.84	3.94	55	2.58	5.87
30	3.88	1.91	4.48	76	3.05	6.5
40	4.21	1.97	4.93	98	3.45	7.03
50	4.48	2.01	5.34	125	3.80	7.51
60	4.71	2.05	5.71	146	4.13	7.94
70	4.91	2.09	6.06	170	4.44	8.35
80	5.10	2.12	6.38	196	4.73	8.73
90	5.27	2.14	6.70	288	5.00	9.10
100	5.43	2.17	6.99	256	5.27	9.44
110	5.57	2.20	7.32	289	5.56	9.83
120	5.71	2.21	7.56	318	5.77	10.10

The Pacific Northwest Laboratory (PNL) wind power classification establishes seven different categories from lowest to highest for wind power at 10 m and 30 m [14]. In Burhaniye, the annual wind power was calculated to be 32 W/m^2, 76 W/m^2, and 318 W/m^2 at 10 m, 30 m, and 120 m. Based on the 10 m PNL wind power classification, the wind resources at Burhaniye fall into class 1. It can be pointed out that the resources of wind energy in Burhaniye can be a poor location.

References

[1] Erdogdu, E. (2009). A snapshot of geothermal energy potential and utilization in Turkey. Renewable and Sustainable Energy Reviews, 13(9), 2535–2543. `https://doi.org/10.1016/j.rser.2009.06.020`

[2] Keskin Citiroglu, H., & Okur, A. (2014). An approach to wave energy converter applications in Eregli on the western Black Sea coast of Turkey. Applied Energy, 135, 738–747. `https://doi.org/10.1016/j.apenergy.2014.05.053`

[3] BoroumandJazi, G., Rismanchi, B., & Saidur, R. (2013). Technical characteristic analysis of wind energy conversion systems for sustainable development. Energy Conversion and Management, 69, 87–94. `https://doi.org/10.1016/j.enconman.2013.01.030`

[4] Koc E, Kaya K, "Enerji Kaynaklari-Yenilenebilir Enerji Durumu", Muhendis ve Makina, cilt 56, sayi 668, s 36-47, 2015

[5] Balikesir'de Yatirim. (2020). `http://www.investinbalikesir.com/` Last Access: 19.09.2020

[6] Johnson GL, "Wind energy systems", Electronic edition, Manhattan, KS, 2001.

[7] Adaramola, M. S., & Oyewola, O. M. (2011). Evaluating the performance of wind turbines in selected locations in Oyo state, Nigeria. Renewable Energy, 36(12), 3297–3304. `https://doi.org/10.1016/j.renene.2011.04.029`

[8] Akpinar, E. K. (2006). A Statistical Investigation of Wind Energy Potential. Energy Sources, Part A: Recovery, Utilization, and Environmental Effects, 28(9), 807–820. `https://doi.org/10.1080/009083190928038`

[9] Ucar, A., & Balo, F. (2009). Investigation of wind characteristics and assessment of wind-generation potentiality in Uludag-Bursa, Turkey. Applied Energy, 86(3), 333–339. `https://doi.org/10.1016/j.apenergy.2008.05.001`

[10] Gokcek, M., Bayulken, A., & Bekdemir, S. (2007). Investigation of wind characteristics and wind energy potential in Kirklareli, Turkey. Renewable Energy, 32(10), 1739–1752. `https://doi.org/10.1016/j.renene.2006.11.017`

[11] Mohammadi, K., & Mostafaeipour, A. (2013). Using different methods for comprehensive study of wind turbine utilization in Zarrineh, Iran. Energy Conversion and Management, 65, 463–470. `https://doi.org/10.1016/j.enconman.2012.09.004`

[12] Akpinar, E. K., & Akpinar, S. (2005). An assessment on seasonal analysis of wind energy characteristics and wind turbine characteristics. Energy Conversion and Management, 46(11–12), 1848–1867. `https://doi.org/10.1016/j.enconman.2004.08.012`

[13] Islam, M. R., Saidur, R., & Rahim, N. A. (2011). Assessment of wind energy potentiality at Kudat and Labuan, Malaysia using Weibull distribution function. Energy, 36(2), 985–992. `https://doi.org/10.1016/j.energy.2010.12.011`

[14] Mohammadi, K., & Mostafaeipour, A. (2013a). Economic feasibility of developing wind turbines in Aligoodarz, Iran. Energy Conversion and Management, 76, 645–653. `https://doi.org/10.1016/j.enconman.2013.06.053`

A New Hybrid System Integrating A Solar Parabolic Trough Collector with A Cylindrical Thermoelectric Generator

Abderrahim Habchi[1], B. Hartiti[2], H. Labrim[3], N. Belouaggadia[4]
[1]isohb2015@gmail.com, 1ERDyS laboratory, MEEM & DD Group, Hassan II University of Casablanca, Mohammedia, Morocco
[2]bhartiti@gmail.com, 1ERDyS laboratory, MEEM & DD Group, Hassan II University of Casablanca, Mohammedia, Morocco
[3]hichamlabrim@yahoo.fr, Materials Science Unit / DERS / CNESTEN National Centre for Energy, Sciences and Nuclear Techniques, Rabat, Morocco
[4]n.belouaggadia@gmail.com, Laboratory of Signals, Distributed Systems and Artificial Intelligence, ENSET, Hassan II University, Mohammedia, Morocco

Abstract

Nowadays, exploitation and production of maximum energy from the solar spectrum is a major concern. In the present paper, a numerical study of a new hybrid system consisting of a solar parabolic trough collector integrated with thermoelectric modules is performed using the Gauss-Seidel iterative method. A realistic climatic conditions are used (sun irradiation and ambient temperature). The effect of thermoelectric generator thickness, the hot/cold fluid flow-rates and load resistance is analysed in order to improve the thermal and electrical performance of the hybrid system. We found that the optimum value of the hot and cold fluid flow-rates is 0.25 Kg/s corresponding to 60.646% as a overall efficiency while the thermoelectric generator efficiency reached to 9.72%. The additional electrical power of the thermoelectric generator can be reach 273.15 W.

Keywords: Parabolic Trough collector, thermoelectric generator, Electrical efficiency, Electrical power.

Introduction

The petroleum industries are widely used in the world to produce electrical power, but due to its negative effect on the environment and the accumulation of toxic gases (CO_2, N_2O, CH_4...) on the atmosphere level [1, 2], for this reason, the researchers start looking for clean and renewable energies that will allow us to generate the electrical power without any negative effect on our planet. According to [3, 4]: the main renewable energy systems and technologies include solar energy (Parabolic Trough Collector (PTC), Photovoltaic system (PV), Solar water heater (SWH)), wind energy, hydropower and biogas. Based on the statistics carried out by the International Renewable Energy Agency (IRENA) [5], the electrical power produced by renewable systems show a significant development, so that the overall power generated by solar systems worldwide is 8,594 GW, while that produced by wind power is approximately 622,704 GW. The global production of hydropower and biogas significantly increases during 2010-2019, so that these systems produce an overall power output of 1024,833 GW and 9,518 GW respectively in 2010, while they increase to 1310,292 GW and 19,453 GW in 2019. Although the significant amount of energy produced by these renewable systems, the petroleum systems remain the world's largest source of electrical power generation [6], For this reason, the researchers have developed renewable systems to produce more energy than petroleum technologies. In this context, we only mention the developments related to the solar systems: parabolic trough concentrator and photovoltaic systems, which are developed by integrating standard parabolic trough and photovoltaic systems with thermoelectric modules [7,8]. Among these hybrid systems, we have found a standard parabolic trough collector, integrated with a photovoltaic cells and a thermoelectric module (PV/TEG-PTC)(tri-generation system) [9]. The obtained results indicate that the electrical efficiency of the hybrid system reached to 240 W corresponding to 57% as a maximum overall efficiency. Also, they have also found that the TEG maximum efficiency reached to 0.5% corresponding to 2.3 W as a maximum power output. Another work [10] studied a hybrid photovoltaic/thermoelectric system with five different cooling methods, namely natural cooling, forced air cooling, water cooling, SiO_2/water nanofluid cooling, and Fe_3O_4/water nanofluid cooling. They observed that the highest power and efficiency was achieved by SiO_2/water nanofluid cooling, so that the maximum power output of the hybrid system reached to 12.7 W corresponding to 14.4% as the overall efficiency of the new system. In the same way, in the present paper, a new hybrid parabolic trough collector is proposed and studied for the first time worldwide, consisting of a parabolic trough collector integrated with tubular thermoelectric generator to cogenerate the thermal and electrical power simultaneously. A 0-D mathematical model is introduced to evaluate the thermal and electrical efficiency respectively of the hybrid system and the thermoelectric generator. Six non-linear algebraic equations are solved by the Gauss-Seidel technique. The effect of cooling and hot mass flow rates, the thermoelectric generator thickness, the load resistance have been studied.

Experiments and Methods

According to Figure 1, the new parabolic trough system is divided into two main circuits: the primary and the secondary circuit. The primary circuit consists of the solar reflector (mirror) (1), the hybrid collector (2) which includes the glass cover (3), the absorber tube (4), the tubular thermoelectric generator (5), the heat transfer fluid (6) and the cooling water (7). In this circuit, the reflected sunlight from the mirror (1) is concentrated at the glass cover (3) and it is partially transmitted to the absorber tube (4). The amount of radiation reached to the absorber tube is absorbed directly by it due to its high absorptivity value (α_{ab}). Then, the heat transfer fluid (Therminol VP[1]) (6) absorbs a significant amount of thermal power from the absorber tube due to the convective heat transfer between the heat transfer fluid and the inner surface of the absorber. On the other hand, when the heat transfer fluid is heated, the thermoelectric generator hot side (top surface) is also heated by convective heat transfer due to direct contact between the TEG hot side and the heat transfer fluid. To create a significant temperature difference at the TEG sides, a cooling water (7) flows beside the TEG cold side. The both fluids movement requires two pumps (8) (9) which permit to maintain the fluids circulation throughout the hybrid system (PTC/TEG). For this purpose, the present system is equipped with a pump (8) attached to the heat transfer fluid and another one (9) associated with the cooling fluid. During the PTC/TEG functioning, the heat-transfer fluid temperature exceeds 100 °C, which is enough to evaporate the cold water in the main tank (10) via a heat exchanger. The water steam is mainly used to rotate the turbine (11) at high pressure (secondary circuit). Consequently, a large amount of electrical power is produced. In addition, the cooling fluid (cold water) (7) passes beside the TEG's inner side to create temperature difference in order to produce a significant amount of additional electrical power, then it exits from the hybrid collector to another tank (12) (intermediate tank) where it can be used for sanitary water or other applications.

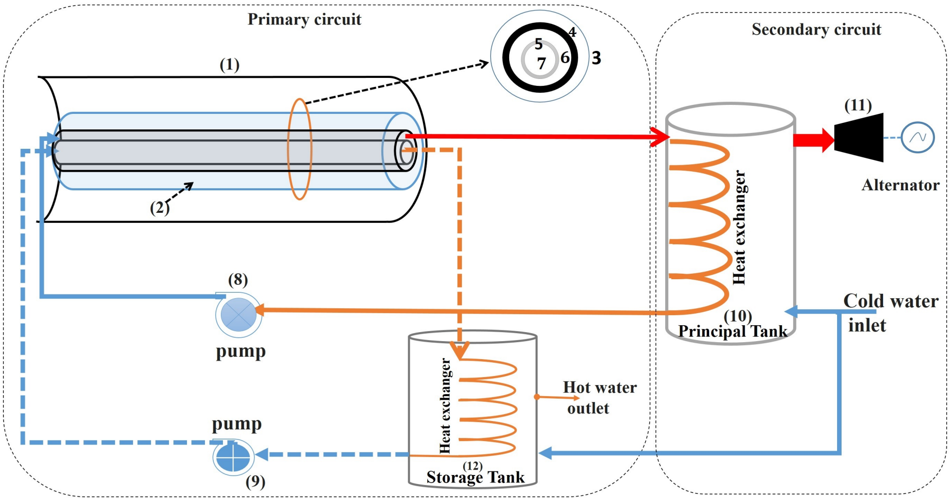

Figure 1: Descriptive diagram of the hybrid PTC system.

The performance study of the majority of solar systems is mainly based on the energy balance of all components of these systems. In the same way, we based on the first law of thermodynamics, the nonlinear thermal equations for the present system can be written as follows:

Glass cover:

$$\rho_g C_g A_g \frac{dT_g}{dt} = I\rho\alpha_g \omega K G_d + A_g k_g \frac{d^2T_g}{d^2x} + \Pi D_{ab}^{ou} h_{ab-g}^{c}(T_{ab}-T_g)+ \Pi D_{ab}^{ou} h^{r}_{ab-g}(T_{ab}-T_g) + \Pi D_g^{ou} h^{c}_{g-am}(T_g - T_{am)} - \Pi D_g^{ou} h^{r}_{g-sky}(T_g-T_{sky}) \tag{1}$$

Absorber:

$$\begin{aligned}\rho_{ab}C_{ab}A_{ab}\frac{dT_{ab}}{dt} = I\rho\alpha_o\omega KG_d + A_{ab}k_{ab}\frac{d^2T_{ab}}{d^2x} - \Pi D^{ou}_{ab}h^c_{ab-g}(T_{ab}-T_g)- \\ \Pi D^{ou}_{ab}h^r_{ab-g}(T_{ab}-T_g) - \Pi D^{in}_{ab}h^c_{ab-hf}(T_{ab}-T_{hf)})\end{aligned} \tag{2}$$

Hot fluid:

$$\begin{aligned}\rho_{hf}C_{hf}A_{hf}\frac{dT_{hf}}{dt} = \Pi D^{in}_{ab}h^c_{ab-hf}(T_{ab}-T_{hf}) + A_{hf}k_{hf}\frac{d^2T_{hf}}{d^2x}- \\ \Pi D^{ou}_{TEG}h^c_{hf-TEG}(T_{hf}-T_{TEGh}) - \dot{m}_{hf}C_{hf}\frac{dT_{hf}}{dx})\end{aligned} \tag{3}$$

TEG hot side:

$$\rho_{TEG}C_{TEG}A_{TEG}\frac{dT_{TEGh}}{dt} = \Pi D^{ou}_{TEG}h^c_{hf-TEGh}(T_{hf}-T_{TEGh}) - \frac{T_{TEGh}-T_{TEGI}}{R_{TEGh}} \tag{4}$$

TEG cold side:

$$\rho_{TEG}C_{TEG}A_{TEG}\frac{dT_{TEGc}}{dt} = \frac{T_{TEGI}-T_{TEGc}}{R_{TEGc}} - \Pi D^{in}_{TEG}h^c_{TEGc-hf}(T_{TEGc}-T_{cf}) \tag{5}$$

Cold fluid:

$$\rho_{cf}C_{cf}A_{cf}\frac{dT_{cf}}{dt} = A_{cf}k_{cf}\frac{d^2T_{cf}}{d^2x} + \Pi D^{in}_{TEG}h^c_{TEGc-cf}(T_{TEGc}-T_{cf}) - \dot{m}_{cf}C_{cf}\frac{dT_{cf}}{dx} \tag{6}$$

To solve the six nonlinear equations (1-6), we discretized the spatiotemporal differential operators using the finite difference method as shown in Table 1. Then, we used the Gauss-Seidel technique to solve iteratively the set of discretized equations.

Table 1: Discretization schemes used.

Discretization schemes Differential Operators	Backward difference	Central difference	Forward difference
$\frac{dT_i}{dt}$	**	**	$\frac{T^{t+\Delta t}_{i,j} - T^{t}_{i,j}}{\Delta t}$
$\frac{dT_i}{dx}$	$\frac{T^{t+\Delta t}_{i,j} - T^{t+\Delta t}_{i,j-1}}{\Delta x}$	**	**

Results and Discussion

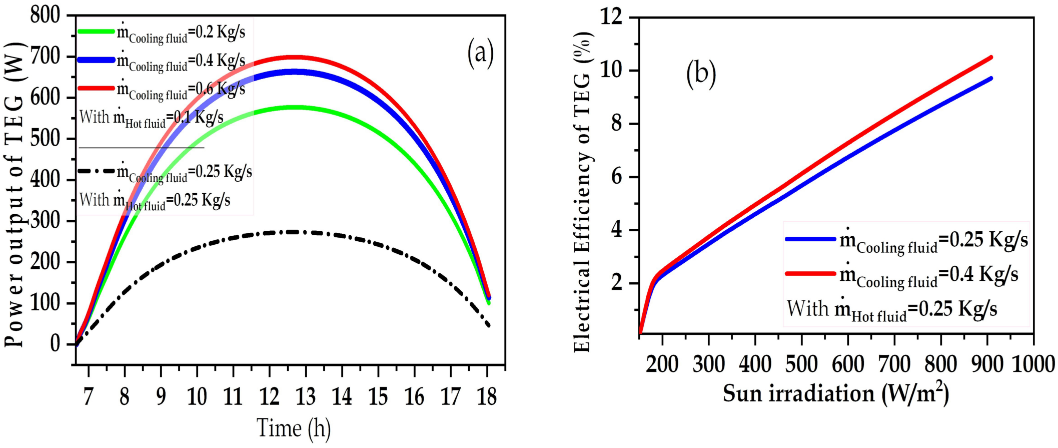

Figure 2: TEG power output (a) and electrical efficiency (b) at various cooling fluid mass flow rate during the day.

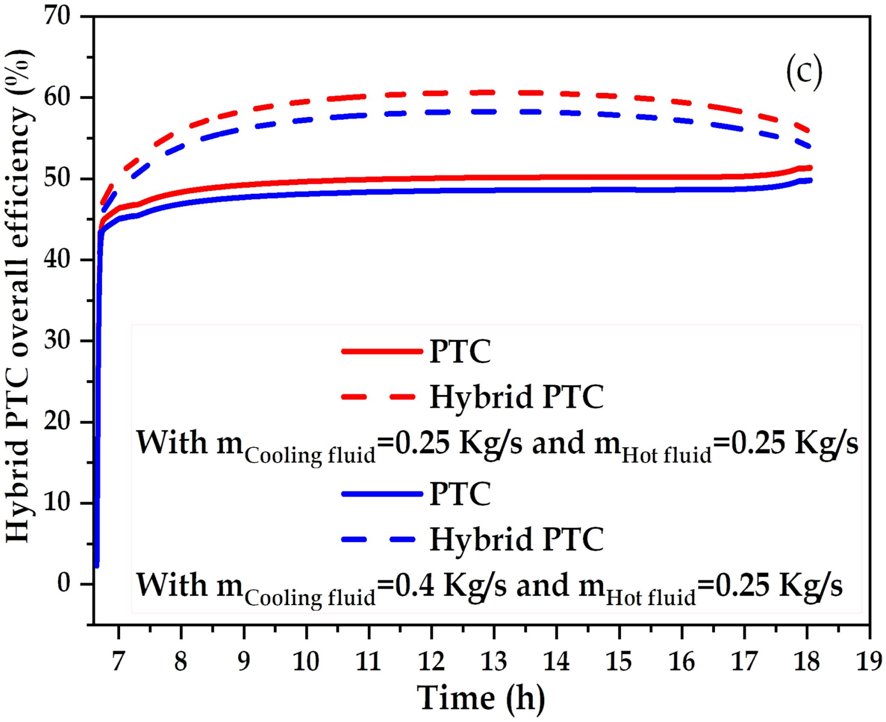

Figure 3: Hybrid PTC efficiency variation at different cooling fluid flow rate.

The TEG power output variation at different cooling fluid flow-rate values is calculated and plotted in Figure 2a. Based on Equation 7 [11], we noticed that the power output of the TEG increases with increasing of cooling fluid flow rate value, due to the rising of the TEG's temperature difference with increasing of cooling flow rate value. The electrical power corresponding to $m_{coolingfluid}$=$m_{hotfluid}$=0.25 kg/s represents the optimal power output of TEG which is reached to 273.15 W.

$$P_{TEG,max} = \frac{n(S\Delta T)^2}{4R_{in}} \tag{7}$$

Where, n, S, ΔT, R$_{in}$, are respectively, the total number of the thermocouples, Seebeck coefficient, temperature difference, internal resistance.

Figure 2b shows the variation of the electrical efficiency of the TEG as a function of sun irradiation. The cooling fluid flow rate was varied from 0.25 to 0.4 Kg/s with m$_{hotfluid}$ is fixed at 0.25 kg/s. Based on Equation 8 [11], we noticed that the electrical efficiency increases with increase of sun irradiation, due to the TEG temperature difference increases with increase of sun irradiation.

$$\eta_{TEG} = \left(\frac{T_{TEGh} - T_{TEGc}}{T_{TEGh}}\right) \frac{\sqrt{1 + ZT_{AV}} - 1}{\sqrt{1 + ZT_{AV}} + \frac{T_{TEGc}}{T_{TEGh}}} \tag{8}$$

Where Z, T$_{Av}$, T$_{TEGh}$, T$_{TEGc}$ are respectively, the merit factor, the TEG average temperature, the hot and cold side temperature of the TEG.

Figure 3 shows the evolution of the thermal efficiency of the new system. The cooling fluid flow rate values were varied from 0.25-0.4 Kg/s with m$_{hotfluid}$=0.25 kg/s. Based on Equation 9 [12], we noticed that the thermal efficiency decreases slightly with increase of cooling fluid flow rate due to the decrease of heat gain under cooling effect.

$$\eta_{PTC} = \frac{\phi_{th}}{A^{PTC}G_d} \tag{9}$$

Where, Φ $_t h$ is the useful flow, A^{PTC} is the PTC aperture area, G$_d$ sun irradiation.

Based on Equation 10 [13], the overall efficiency of the hybrid system is significantly improved due to the combination of the TEG with the PTC, so that the maximum efficiency value of the new system reached to 60.646%. The optimum thermal efficiency is 60.646% corresponding to 273.15 W as optimum power output of TEG, which can be achieved with a m$_{coolingfluid}$ =0.25 kg/s with m$_{hotfluid}$=0.25 kg/s.

$$\eta_0 = \eta_{PTC} + \eta_{TEG} \tag{10}$$

Summary

In this paper, the thermal and electrical performance of the new parabolic trough concentrator are investigated. A 0-D mathematical model is introduced to evaluate the thermal and electrical efficiency of the new system and the thermoelectric generator, respectively. Six non-linear equations are solved by the Gauss-Seidel method. The main results showed that the electrical efficiency efficiency reach 9.72% corresponding to 273.15 W. Also, the overall efficiency of the new system is up to 60.646%, which means that the new hybrid system is able to generate both thermal and additional electrical power simultaneously, which is very promising for future parabolic trough collector developments.

References

[1] Kakaei, K., Esrafili, M. D., & Ehsani, A. (2018). Graphene Surfaces: Particles and Catalysts (Volume 27) (Interface Science and Technology (Volume 27)) (1st ed.). Academic Press.(p. 387–437)

[2] Badr, O., & Probert, S. D. (1995). Sinks and environmental impacts for atmospheric carbon monoxide. Applied Energy, 50(4), 339–372. `https://doi.org/10.1016/0306-2619(95)98803-a`

[3] Bal, J.-L., & Chabot, B. (2001). Les énergies renouvelables. État de l'art et perspectives de développement. Comptes Rendus de l'Académie Des Sciences - Series IIA - Earth and Planetary Science, 333(12), 827–834. `https://doi.org/10.1016/s1251-8050(01)01720-7`

[4] Abdulhamed, A. J., Adam, N. M., Ab-Kadir, M. Z. A., & Hairuddin, A. A. (2018). Review of solar parabolic-trough collector geometrical and thermal analyses, performance, and applications. Renewable and Sustainable Energy Reviews, 91, 822–831. `https://doi.org/10.1016/j.rser.2018.04.085`

[5] Adrian W, Sonia R, Dennis A, Nazik E, Gerardo E, Lana A. Renewable Capacity Statistics 2020. (2020). IRENA. `https://www.irena.org/publications/2020/Mar/Renewable-Capacity-Statistics-2020`

[6] Daugy M. Monthly electricity statistics – Analysis. (2020). IEA. `https://www.iea.org/reports/monthly-electricity-statistics`

[7] Sundarraj, P., Maity, D., Roy, S. S., & Taylor, R. A. (2014). Recent advances in thermoelectric materials and solar thermoelectric generators – a critical review. RSC Adv., 4(87), 46860–46874. `https://doi.org/10.1039/c4ra05322b`

[8] Sahin, A. Z., Ismaila, K. G., Yilbas, B. S., & Al-Sharafi, A. (2020). A review on the performance of photovoltaic/thermoelectric hybrid generators. International Journal of Energy Research, 44(5), 3365–3394. `https://doi.org/10.1002/er.5139`

[9] Soltani, S., Kasaeian, A., Sokhansefat, T., & Shafii, M. B. (2018). Performance investigation of a hybrid photovoltaic/thermoelectric system integrated with parabolic trough collector. Energy Conversion and Management, 159, 371–380. `https://doi.org/10.1016/j.enconman.2017.12.091`

[10] Soltani, S., Kasaeian, A., Sarrafha, H., & Wen, D. (2017). An experimental investigation of a hybrid photovoltaic/thermoelectric system with nanofluid application. Solar Energy, 155, 1033–1043. `https://doi.org/10.1016/j.solener.2017.06.069`

[11] Rowe, D. M. (1995). CRC Handbook of Thermoelectrics (1st ed.). CRC Press.

[12] Duffie, J. A., & Beckman, W. A. (2013a). Solar Engineering of Thermal Processes (4th ed.). Wiley.

[13] Mohsenzadeh, M., Shafii, M. B., & Jafari mosleh, H. (2017). A novel concentrating photovoltaic/thermal solar system combined with thermoelectric module in an integrated design. Renewable Energy, 113, 822–834. `https://doi.org/10.1016/j.renene.2017.06.047`

Synthesis of Thiophene-Based Hole Transport Material for Perovskite Solar Cells

Busra Cuhadar[1], Ayfer Kalkan Burat[2], Esra Ozkan Zayim[3], Nilgun Karatepe[4]
[1]cuhadarb@itu.edu.tr, Department of Chemistry, Istanbul Technical University, Istanbul, Turkey
[2]kalkanayf@itu.edu.tr, Department of Chemistry, Istanbul Technical University, Istanbul, Turkey
[2]ozesra@itu.edu.tr, Department of Chemistry, Istanbul Technical University, Istanbul, Turkey
[2]kmnilgun@itu.edu.tr, Energy Institute, Istanbul Technical University, Istanbul, Turkey

Abstract

In this study, 2,6-disubstituted dithienothiophene (DTT) derivative was synthesized. The DTT derivative was synthesized in several steps using a convenient route starting with thiophene. At each step, the obtained compounds were purified using chromatographic methods, and the yields of intermediate products were quite high. However, the final product was obtained in a very low yield. Characterization of the compounds was carried out using ^{1}H NMR, ^{13}C NMR, and FT-IR spectroscopic techniques.

Keywords: Thiophene, dithienothiophene, hole-transport material, perovskite.

Introduction

The need for energy has become even more important due to the rapid growth of the planet's population and the increase in energy consumption. Since traditional energy sources such as fossil fuels are limited and cause environmental pollution; alternative energy sources are critical. Solar energy stands out as a clean, reliable and renewable energy source, unlike traditional energy sources. Electricity generation from solar energy is provided by solar cells or photovoltaic cells with the photovoltaic effect of semiconductors. In recent years, a wide variety of solar cell technologies including dye sensitized solar cells, bulk heterojunction solar cells, hybrid organic-inorganic solar cells have been researched and developed [1–3].

Recently, perovskite solar cells (PSCs) appear to be promising new generation photovoltaic technology due to high efficiency, low cost and easy fabrication. Despite the low PCE and poor stability of the first PSCs, an increase of over 20% has been achieved in PCE today [4]. The reason for this rapid increase in PCEs is the development of novel perovskite materials and manufacturing techniques. Although perovskite solar cells have high PCEs, they still tend to degrade when exposed to moisture and heat. Therefore, each layer has been investigated in detail to increase the stability of PSCs. One of these layers, the hole transport layer (HTM), not only extract holes, but also protects the perovskite layer from air and improves the stability of the device. 2,2',7,7'-tetrakis-(N,N-di-4-methoxyphenylamino)-9,9'-spirobifluorene (Spiro-OMeTAD) is the most widely used HTM in PCSs [5]. Due to the disadvantages of Spiro-OMeTAD such as low mobility, low life cycle and high cost, interest in low cost and stable HTMs such as small organic molecules, polymeric or inorganic compounds have increased [6, 7].

Organic semiconducting materials are very attractive as a low-cost alternative to conventional silicon transistors for various electronic applications due to their high mobility and stability [8]. Thiophene-based materials have been considered as promising candidates for organic semiconductors, and they have been successfully used as key cores in organic field effect transistors (OFETs), organic light-emitting diodes (OLEDs), and photovoltaic cells [9]. The performance of fused-thiophene is associated with the role of sulphur d-orbitals, which mix well with aromatic π-orbitals, such that electron-transfer across the π-center to the acceptor unit is facilitated, thereby enabling prolonged injection efficiency. Furthermore, fused thiophene derivatives exhibit excellent photo and thermal stability, affording improved performance as photosentitizers. Because of the potential applications and various properties of thiophene derivatives, such as unique chemical stability, excellent electronic configuration, and incredible synthetic versatility, they have been employed as hole transporting materials (HTMs) in perovskite solar cells (PSCs) [10].

Dithienothiophene derivatives (DTT) are also important building blocks of a wide variety of materials for electronic and optical applications due to their considerable mobility [11]. From this point of view, we report herein the synthesis and characterization of 2,6-disubstituted dithienothiophene. The HOMO-LUMO energy levels, and thin film properties of DTT derivative will be investigated for possible application in PSCs as HTM.

Experimental

Tetraiodothiophene (1)

Thiophene (4.2 g, 49.9 mmol), iodine (22 g, 87.3 mmol) and iodic acid (7.9 g, 44.9 mmol), 20 mL water, 42.5 mL acetic acid, 16.25 mL carbon tetrachloride and 1.125 mL sulfuric acid were added to a mixture. The reaction was stirred at 120 °C for 7 days. The product formed during this time precipitated into the reaction medium. The precipitate formed was first filtered, then washed with $Na_2S_2O_3$ and plenty of water and dried in vacuum. The light cream coloured substance was crystallized in dioxane. Yield: 25 g (88%). (C_4I_4S, 587.7 g/mol). M.P. 211 °C. FT-IR, ν (cm^{-1}): 1433 (C=C), 1360, 1219, 817, 695 (C–S–C); No peaks were seen in ^{1}H NMR (DMSO-d_6, 500 MHz) (there are only solvent peaks). ^{13}C NMR (DMSO-d_6, 500 MHz) δ: 108,49 (C-I), 91,26 (S-C-I).

3,4-Diiodo-2,5-bis[2-(trimethylsilyl)ethynyl] thiophene (2)

Tetraiodothiophene (4 g, 6.8 mmol) was added to a solution of CuI (0.06 g, 0.33 mmol), trans-dichloro(triphenylphosphine)palladium (0.23 g, 0.33 mmol), triphenylphosphine (0) (0.08 g, 0.3 mmol), 2 mL of trimethylsilyl acetylene (1.5 g, 14.9 mmol), and 30 mL of diisopropylamine. The reaction mixture was stirred for 21 hours at room temperature, then heated to reflux for 1 hour. After cooling to room temperature, the mixture was filtered and the precipitate was washed with dichloromethane (DCM). The solvent was removed under vacuum and the remaining solid was purified by column chromatography with silica gel using hexane: DCM (4:1) as fluent. Yield: 2.5 g (69%). ($C_{14}H_{18}I_2SSi_2$, 528.3 g/mol). M.P. 85 °C. FT-IR, ν (cm_{-1}): 2954 (aliphatic CH), 2148 (C≡C), 1459 (C=C), 1248 (C-Si), 836, 757, 698 (C–S–C); ^{1}H NMR ($CDCl_3$, 500 MHz) δ: 0.3 (s, 18H, CH). ^{13}C NMR ($CDCl_3$, 500 MHz) δ: 126.46 (S-C), 104.70 (Si-C), 101.09 (I-C), 97.87(C≡C), 0.29 ($Si\text{-}CH_3$).

Dithieno[3,2-b: 2’, 3’-d]thiophene (3)

A solution of compound **2** (1 g, 2.0 mmol), sodium sulphite (2.90 g, 12.12 mmol), CuI (0.076g, 0, 40 mmol) and tetramethylethylenediamine (TMEDA) (0.09 g, 0.80 mmol) in 30 mL of dry DMF was stirred at 80 °C for 24 hours under nitrogen atmosphere. After cooling to room temperature, the reaction mixture was filtered off and then the solvent was removed under vacuum. The yellowish product is purified by column chromatography with silica gel by using hexane:DCM (4: 1) as fluent. Yield: 0.17 g (45%). ($C_{18}H_4S_3$, 195.5 g/mol). M.P. 63 °C. FT-IR, ν (cm^{-1}): 3098-3076 (Ar-H), 2921,1359 (C=C), 1178, 1079, 894, 794, 672 (C–S–C); ^{1}H NMR ($CDCl_3$, 500 MHz) δ: 7.41 (d, 2H, S–CH), 7.40 (d, 2H, C–CH). $_{13}$C NMR ($CDCl_3$, 500 MHz) δ: 141.56, 130.84, 125.80, 120.77.

2,6-Dibromodithieno[3,2-b: 2’, 3’-d]thiophene (4)

To a solution of 0.3 g dithieno[3,2-b: 2 ’, 3’-d]thiophene **(3)** (1.53 mmol) in a 16 mL of $CHCl_3$: CH_3COOH (1:1) mixture was added N-bromosuccinimide (0.68 g, 3.821 mmol) slowly. After stirring for 24 h at room temperature, the mixture was extracted with DCM. The organic layer separated and washed with brine and water, respectively, and dried over Na_2SO_4. The solvent was removed under vacuum and the white solid was purified by column chromatography with silica gel by using petroleum ether as an fluent. Yield: 0.40 g (75%). ($C_8H_2Br_2S_3$, 354.09 g/mol). M.P. 164 °C; FT-IR, ν (cm^{-1}): 3084, 1470, 1353, 1101, 945, 805; ^{1}H NMR ($CDCl_3$, 500 MHz) δ: 7.28 (s, 2H). ^{13}C NMR ($CDCl_3$, 500 MHz) δ: 139.07, 130.83, 123.19, 112.35.

2,6-Bis[di(4-metoxypheny)amino]dithieno[3,2-b: 2’, 3’-d]thiophene (5)

To a Schlenk flask containing anhydrous deoxygenated toluene (5 mL) was added Pd_2dba_3 (0.01 g, 0.040 mmol) and $PtBu_3$ (10% wt. solution in toluene, 0.1 mL). After stirring for 25 min, compound **4** (0.10 g, 0.30 mmol), di(4-methoxyphenyl) amine (0.16 g, 0.70 mmol), and sodium tert-butoxide (0.07 g, 0.70 mmol) were added. The reaction mixture was heated to reflux for 48 h. After cooling to room temperature, the mixture was extracted with DCM The organic layer separated and washed with water, and dried over Na_2SO_4. The solvent was removed under vacuum and the yellow oily product was obtained.

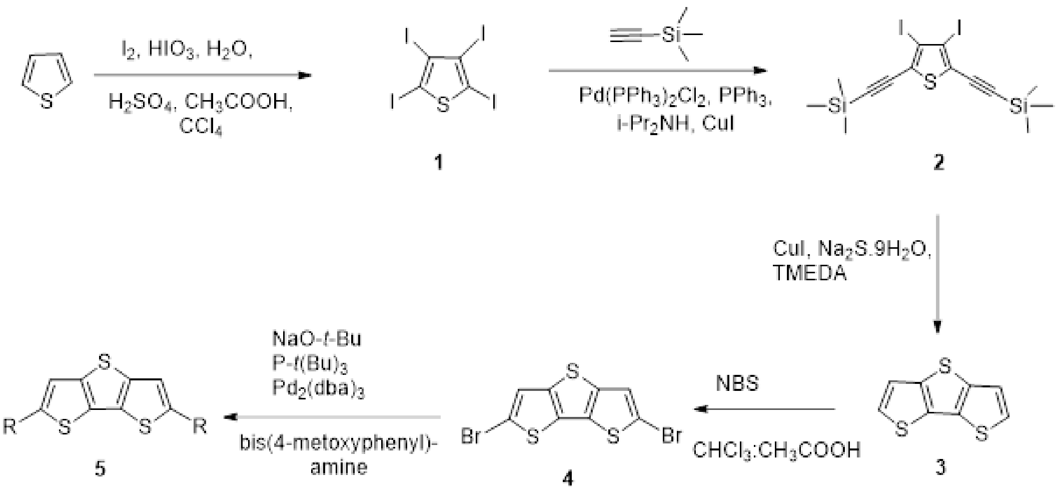

Figure 1: Synthesis of DTT derivative.

Results and Discussion

There are different procedures for the synthesis of DTT derivatives in the literature. In this study, thiophene was used as the starting material and DTT derivative was synthesized in five steps (Figure 1). In the first step, tetraiodothiophene **(1)** was obtained from the reaction of thiophene with iodine after 7 days according to the literature [12]. The reaction was carried out at 120 °C and the compound was obtained in high yield. Since there is no proton in the structure of compound **1**, only solvent peaks were observed in the ^{1}H NMR spectrum, and two peaks were observed in the ^{13}C NMR spectrum. In the second step trimethylsilyl acetylene groups were attached to the 3,5 positions of compound **1**. The reaction was carried out under palladium catalysis in the presence of CuI and triphenylphosphine [12]. In the ^{1}H NMR spectrum of **2** in CDCl$_3$, the aliphatic protons appeared at 0.3 ppm. The ^{13}C NMR spectrum of **2** indicated C atoms at 126.46, 104.70, 101.09, 97.87, and 0.29 ppm, respectively. In the third step dithieno[3,2-b: 2 ', 3'-d]thiophene **(3)** was prepared from compound **2** according to the literature [12]. The yield of this step was lower than the first two steps. In the ^{1}H NMR spectrum of **3**, protons of thiophene ring were observed at 7.41 and 7.40 ppm as doublet. The ^{13}C NMR spectrum of the compound also confirmed the structure. Bromination of DTT at 2,6- positions were carried out in chloroform acetic acid mixture in the presence of NBS under mild conditions [13]. The reaction was carried out in high yield and the white product was purified by chromatographic method. Two protons in the structure **(4)** were observed as singlets at 7.28 ppm. In addition, in the ^{13}C NMR spectrum, four carbon atoms were detected between 139-112 ppm. The synthesis of 2,6-disubstituted DTT derivative was accomplished by the reaction of 2,6-dibromodithienothiophene with di(4-methoxyphenyl)amine in the presence of palladium catalyst. Since the reaction is sensitive to oxygen, nitrogen gas was passed through the reaction, but the desired product was obtained in a very low yield. The optimization of the reaction conditions are ongoing in order to make electrochemical measurements of compound **5** and to perform cell studies.

Conclusions

In this work, 2,6-disubstituted dithienothiophene (DTT) derivative was prepared and characterized with spectral methods. The intermediate products were synthesized with high yields. However, the desired product was obtained with low yield due to the sensitivity of the last step to air. Therefore, the reaction conditions will be optimized to increase the yield of desired compound. In the next part of the study, our aim is to determine the HOMO-LUMO energy levels of the DTT derivative by cyclic voltammetry (CV) and to investigate the properties of the DTT derivative as a HTM in perovskite solar cells.

Acknowledgements

This work was supported by TUBITAK (Project No: 218M110).

References

[1] Dualeh, A., Moehl, T., Nazeeruddin, M. K., & Gratzel, M. (2013). Temperature Dependence of Transport Properties of Spiro-MeOTAD as a Hole Transport Material in Solid-State Dye-Sensitized Solar Cells. ACS Nano, 7(3), 2292–2301. `https://doi.org/10.1021/nn4005473`

[2] Laban, W. A., & Etgar, L. (2013). Depleted hole conductor-free lead halide iodide heterojunction solar cells. Energy & Environmental Science, 6(11), 3249. `https://doi.org/10.1039/c3ee42282h`

[3] Stranks, S. D., Eperon, G. E., Grancini, G., Menelaou, C., Alcocer, M. J. P., Leijtens, T., Herz, L. M., Petrozza, A., & Snaith, H. J. (2013). Electron-Hole Diffusion Lengths Exceeding 1 Micrometer in an Organometal Trihalide Perovskite Absorber. Science, 342(6156), 341–344. `https://doi.org/10.1126/science.1243982`

[4] Best Research-Cell Efficiency Chart. (2019). [Graph]. `https://www.nrel.gov/pv/cell-efficiency.html` Last Access: 21.09.2020

[5] Li, X., Bi, D., Yi, C., Decoppet, J.-D., Luo, J., Zakeeruddin, S. M., Hagfeldt, A., & Gratzel, M. (2016). A vacuum flash–assisted solution process for high-efficiency large-area perovskite solar cells. Science, 353(6294), 58–62. `https://doi.org/10.1126/science.aaf8060`

[6] Zhang, P.-P., Zhou, Z.-J., Kou, D.-X., & Wu, S.-X. (2017). Perovskite Thin Film Solar Cells Based on Inorganic Hole Conducting Materials. International Journal of Photoenergy, 2017, 1–10. `https://doi.org/10.1155/2017/6109092`

[7] Bakr, Z. H., Wali, Q., Fakharuddin, A., Schmidt-Mende, L., Brown, T. M., & Jose, R. (2017). Advances in hole transport materials engineering for stable and efficient perovskite solar cells. Nano Energy, 34, 271–305. `https://doi.org/10.1016/j.nanoen.2017.02.025`

[8] Xu, X., Cai, P., Lu, Y., Choon, N. S., Chen, J., Hu, X., & Ong, B. S. (2012). Synthesis and characterization of thieno[3,2-b]thiophene-isoindigo-based copolymers as electron donor and hole transport materials for bulk-heterojunction polymer solar cells. Journal of Polymer Science Part A: Polymer Chemistry, 51(2), 424–434. `https://doi.org/10.1002/pola.26400`

[9] Calio, L., Kazim, S., Gratzel, M., & Ahmad, S. (2016). Hole-Transport Materials for Perovskite Solar Cells. Angewandte Chemie International Edition, 55(47), 14522–14545. `https://doi.org/10.1002/anie.201601757`

[10] Zimmermann, I., Urieta-Mora, J., Gratia, P., Arago, J., Grancini, G., Molina-Ontoria, A., Orti, E., Martín, N., & Nazeeruddin, M. K. (2016). High-Efficiency Perovskite Solar Cells Using Molecularly Engineered, Thiophene-Rich, Hole-Transporting Materials: Influence of Alkyl Chain Length on Power Conversion Efficiency. Advanced Energy Materials, 7(6), 1601674. `https://doi.org/10.1002/aenm.201601674`

[11] Yi, W., Zhao, S., Sun, H., Kan, Y., Shi, J., Wan, S., Li, C., & Wang, H. (2015). Isomers of organic semiconductors based on dithienothiophenes: the effect of sulphur atoms positions on the intermolecular interactions and field-effect performances. Journal of Materials Chemistry C, 3(41), 10856–10861. `https://doi.org/10.1039/c5tc02287h`

[12] Zong, K., Park, K., & Park, J. (2016). A Convenient Synthesis of Dithieno[3,2-b:2',3'-d]thiophenes from Thiophene. Synthesis, 48(23), 4126–4130. `https://doi.org/10.1055/s-0035-1562531`

[13] Zhu, M., Luo, H., Wang, L., Guo, Y., Zhang, W., Liu, Y., & Yu, G. (2013). The synthesis of 2,6-dialkylphenyldithieno[3,2-b:2',3'-d]thiophene derivatives and their applications in organic field-effect transistors. Dyes and Pigments, 98(1), 17–24. `https://doi.org/10.1016/j.dyepig.2013.02.007`

A Study on Energy Audit and Project to Increase Energy Efficiency for a University Campus Buildings

Ismail Ekmekci
iekmekci@ticaret.edu.tr, Engineering and Design Faculty, Istanbul Commerce University, Istanbul, Turkey

Abstract

Energy Audit is very important to determine energy saving potentials and also of great importance to create a road map in terms of energy efficiency investments in both buildings and industry. Energy Audit study of the Istanbul Commerce University campus building in Kucukyali is established by evaluating the natural gas and electricity bills and 3 years of energy consumption data and the required costs. Energy invoices for three years have been analysed for the study of energy audit of Istanbul Commerce University Kucukyali Campus. By converting natural gas and electrical energy consumption values into TEP values in these invoices, heat and electrical energy are combined under a single unit. In terms of being an example as an educational institution, necessary tables and statistical tables and graphs were prepared for the university campus. In this campus, energy consumption related to heating, cooling, ventilation and lighting systems in buildings are examined in details. Required measurements and calculations were made in this university campus. The heating, cooling systems and the related energy consumption rates are investigated in this study. Measurement and calculations of the current uninsulated state of the campus buildings are accomplished then CO_2 emissions rates for the existed and insulated conditions are compared; annual energy savings rates computed for each of specific consumptions per m^2 and m^3 utilization spaces; the payback period of the required investments and in house profitability rates are also computed and also required comparisons are conducted.

Keywords: Building Energy Performance; Energy Audit; Energy Saving Project; Energy Efficiency.

Introduction

In this study, energy efficiency possibilities were investigated by obtaining data for the years 2009, 2010 and 2011 in the Kucukyali Campus of Istanbul Commerce University and by examining the equipment in the campus buildings. Energy consumption information of the buildings is given in summary, especially consumption and cost information is supported by graphics and tables. Also; the purpose of the study, its scope, the dates it was conducted, the areas where the study was conducted and the findings and suggestions in these areas were briefly and concisely presented to the senior management, and also detailed where necessary. In this campus, within the scope of the energy study, the heating, cooling, ventilation and lighting systems in the buildings and the related energy consumption were examined. These systems have been examined and evaluated in terms of energy saving and energy efficiency. The energy consumption and cost values of the buildings in this campus for the years 2009, 2010 and 2011 were determined by the records kept by the university administration and also by the documents obtained from the distribution companies. In the light of consumption information, monthly analyses are made and processed in tables and graphics. It was recommended to make insulation in accordance with TS 825 standards with the Building Energy Performance Regulation (BEP-TR) published in the official newspaper dated 01.04.2010 and numbered 27539 and the calculations were renewed accordingly [1]. Energy saving values on annual basis are calculated as specific values per building-m^2 usage area [2].

Purpose of the Study

With the energy efficiency study within the scope of this study, the current situation was determined by evaluating the measurements and data in the buildings in the campus; suggestions and projects were created by examining the results; efforts have been made to use energy more efficiently; the uses of alternative and renewable energy sources were examined; analyses were conducted to investigate energy saving opportunities for uninsulated campuses and outbuildings and to prepare efficiency enhancing projects (VAP). This study aimed at:

- To make building insulations in compliance with TS_825 and energy performance regulation in buildings.
- To reduce annual energy consumption without compromising comfort conditions
- Reducing greenhouse gases and CO_2 emissions.
- To establish energy efficiency awareness.
- To choose economical devices and equipments used in energy sources used in heating, cooling and lighting.
- By examining the work schedule of the educational institution, making an automation scenario and implementing an automation program that provides optimum solutions with the least energy consumption.
- To reduce the specific energy consumption per unit square meter or cubic meter.

Scope of the Study

Within the scope of the energy efficiency study, measurements and analyses were carried out in sections such as the boiler room, pumps, chiller groups, lighting systems in the campus. With the study, it is aimed to ensure that the function of the institution continues with optimum energy without compromising the service quality and comfort of the institution. It was observed that the buildings on the campus did not have sufficient thermal insulation; therefore the savings to be achieved were determined by extracting the necessary insulation details according to the TS825 standard. The savings to be obtained as a result of the Energy Survey study are calculated in terms of the amount and cost of energy per unit square meter or cubic meter. In addition, the results of the thermal insulation application in the campus are calculated as TEP/year and TL/m^2.

Investigation of Heating-Cooling Mechanical Installation Equipment in Campus:

The capacities of heating and hot water boilers used for heating in the campus are as follows:

- New building heating hot water boiler 475 000 kcal/h
- Engineering Faculty 1st hot water boiler 150 000 kcal/h
- Engineering Faculty 2nd hot water boiler 250 000 kcal/h
- Faculty of Engineering 3rd Hot Water Boiler 425 000 kcal/h
- Hot Water boiler 425 000 kcal/h
- Total 1 725 000 kcal/h

1 725 000 / 17 888 = 96.4 kcal/h-m^2 = 112 W/m^2.

The following measurements were taken in order to determine the efficiency values of the boilers:

Measurement of Flue Gas Emissions; Measuring Fuel Consumption; Measurement of Boiler Return Water Temperature; Measurement of Boiler Surface Temperatures; Control of Boiler Temperatures with Thermal Camera; Measuring the Ambient Temperature of the Boiler Room as of the Season.

Inspection of Heating, Cooling Equipments and Electrical Installation, Electrical Motors and Lighting Systems on Campus

The buildings on the campus are not insulated and the project was prepared in accordance with TS 825 and heat losses were examined [1,3] and existing non-insulated and insulated energy consumption values can be seen at Table 1. A cost-benefit analysis has been carried out for placing an economizer between the flue and the boiler in order to increase the boiler efficiency by utilizing the flue gas waste heat of the boilers; the insulation conditions of the installation pipes have been examined [2]. The locations and spaces of the cooling groups, the capacities of the cooling systems and the efficiency of the cooling devices were also examined. Analysis of the electrical installation; study of electric motors; examination of frequency inverter requirement of pumps and analysis of building lighting system were made.

By converting natural gas and electricity consumption to TEP equivalent, total yearly energy consumption and annual total costs were analysed and monthly changes of electricity and natural gas consumption by years in the campus and monthly changes of TEP equivalents of these consumption by years are given in the relevant tables; additionally graphically the changes in electrical energy consumption and costs in the relevant figures given graphically then natural gas consumption and cost changes in other relevant figures; also in other figures total energy consumptions and changes with TEP values are given graphically. When looking at these tables, it is seen that the electrical energy consumption equivalents vary between 63% and 76%; on the other hand, it was seen that the electricity cost rates varied between 78% and 89%; it was found that the high share of electricity cost is due to the higher unit price of electricity.

Examination of the applicability of the trigeneration system; examination of the absorption cooling system; wind energy system implementation; the application of the solar energy system and the application of the ground source water to water heat pump have been studied.

In the energy audit study, calibrated and labelled devices by accredited national or international organizations were used.

Energy Consumption and Costs

For the energy audit study, energy consumption and cost analyses for the years 2009-2010-2011 were made. The following tables and graphics were prepared with the values obtained; accordingly required analysis and comments have been made.

Table 1: Comparison of insulated and non-insulated cases.

	Noninsulated	Insulated
TOTAL HEATING LOAD (kW)	1532	1330
TOTAL HEATING LOAD (kcal/h)	1317417	1143663
HEATED SITE AREA (m^2)	17888	17888
HEATED SITE VOLUME(m^3)	53664	53664
SPECIFIC HEAT REQUIREMENT (kWh/m^2)	56	0.0743
SPECIFIC HEAT REQUIREMENT(kWh/m^3)	0.0285	0.0248
ENERGY SAVINGS TO BE ACHIEVED(kcal/h)	173754	
NATURAL GAS SAVING(m^3/h)	23.4012	
ANNUAL BOILER BURNING TIME(h)	2160	
ANNUAL FUEL SAVING (m^3/year)	50546	
FUEL PRICE (TL/m^3)	0.85	
ANNUAL PROFIT (TL)	42965	
SAVING RATE (%)	13.19	

In 2009, natural gas consumption was 37% and electrical energy used was 63%; when analysed in terms of cost, the cost of natural gas was 21% and the cost of electricity was 79%. High share of electricity in cost; it is due to the high unit price of electricity.

In 2010, the natural gas consumption was 23% and the electrical energy used was 77%. When examined in terms of cost, natural gas was 11% and electricity was 89%. Considering the tables, the use of natural gas has increased by 2.4% with an addition of 1109 m^3 to 46 905 m^3; It was observed that electricity consumption increased by 49% from 781 595 kWh to 1 491 320 kWh.

In 2011, the natural gas consumption was 23% and the electrical energy used was 77%. When examined in terms of cost, natural gas was 10% and electricity was 90%. Considering the tables, the use of natural gas has increased by 19.1% with an addition of 9190 m^3 to 48014 m^3; It was observed that electricity consumption decreased by 11% from 1 491 320 kWh to 1 341 125 kWh compared to 2010.

Energy Audit Study Results and Analysis

In the energy audit study and analysis, the energy value to be saved, the projected expenditure amount, the payback period, with measures such as general findings and the insulation of external façade and plumbing pipes in accordance with the regulation, the use of economizers in the boilers, the use of more efficient equipment in motors and lighting systems in order to achieve energy efficiency and energy savings. Information such as the amount of reduction in energy consumption and the envisaged implementation plan are summarized in Table 1.

In the study we conducted, energy expenses for the years 2009-2010-2011 were recorded in the tables and graphs were obtained. When the tables in Table 2, 3, 4 are examined, it is seen that natural gas consumption is balanced according to seasonal conditions. In the electricity consumption, sharp increases were observed in February, March and April in 2011; in our examination, it was seen that the reason for this increase in electricity consumption was due to the revision and renovation works carried out for the commissioning of the additional building.

As a result of the energy audit study specific energy consumption values for three years with respect to TEP values by months have been analysed in details and those values were given at following Table 6. Energy efficiency increasing project (VAP) calculations were also made for the energy saving measures and according to our VAP studies, 15.40 TEP annual energy saving amounts and 15 770 TL cost saving can be obtained and 73705 TL investment and also 4.67 years payback period will be required and summarized values of VAP results can be seen at Table 5.

Table 2: 2009 Energy consumption and costs.

Energy Type	Consumption				Cost		Unit Cost
	Amount	Unit	TEP	% Total	TL	% Total	TL/TEP
Electricity	781.595	kWh	67.22	63.46	214965.60	78.87	3198.08
Natural Gas	46.905	Sm^3	38.70	36.54	57607.00	21.13	1488.68
TOTAL			105.91		272572.60		

Table 3: 2010 Energy consumption and costs.

Energy Type	Consumption				Cost		Unit Cost
	Amount	Unit	TEP	% Total	TL	% Total	TL/TEP
Electricity	1491.320	kWh	128.25	76.40	390552.84	89.25	3045.16
Natural Gas	48.014	Sm^3	39.61	23.60	47.024.00	10.75	1187.13
TOTAL			167.87		437576.84		

Table 4: 2011 Energy consumption and costs.

Energy Type	Consumption				Cost		Unit Cost
	Amount	Unit	TEP	% Total	TL	% Total	TL/TEP
Electricity	1.341.126	kWh	115.34	71	374113	87	3243.66
Natural Gas	57.204	Sm^3	47.19	29	56672	13	1200.85
TOTAL			162.53		430785		

Table 5: Summary of energy efficieny increasing project information.

Project Information						
Energy Saving Project Components	Energy Type	Annual Saving Amount			Cost	Payback Period
		Orginal Unit	TEP/Year	TL/Year	TL	Year
Exterior Insulations	Natural Gas	Sm^3	14.10	14437.21	67855.00	4.7
Placing Economizer at Boiler Outlets	Natural Gas	Sm^3	1.3	1332.14	5850.00	4.39
TOTAL			**15.40**	**15769.35**	73705.00	4.67

Table 6: Specific energy consumption values between 2009-2011.

Month	2009		2010		2011	
	$x10^5TEP/m^2$	kWh/m^2	$x10^5TEP/m^2$	kWh/m^2	$x10^5TEP/m^2$	kWh/m^2
January	7.6420	8.8842	7.1904	8.3593	6.5786	3.5143
February	6.1272	7.1233	7.8337	9.1071	10.2665	7.0812
March	7.5583	8.7870	6.4271	7.4721	10.7880	6.7277
April	6.3260	7.3545	5.7750	6.7141	9.7172	6.8281
May	5.3834	6.2589	7.6439	8.8875	7.2207	6.6157
June	4.2675	4.9622	5.7363	6.6700	5.8706	5.3274
July	3.9977	4.6484	7.6702	8.9189	6.2785	7.2893
August	3.3351	3.8780	7.1713	8.3387	6.1179	7.1138
September	2.8763	3.3445	4.3823	5.0957	4.5224	5.2516
October	2.9820	3.4674	4.3554	5.0645	5.5193	5.8799
November	3.4052	3.9594	6.8746	7.9929	7.7073	6.4849
December	5.3087	6.1722	7.2360	8.4132	10.2729	6.8597
Average	4.9341	5.7367	6.5247	7.5862	7.5717	6.2478

Conclusions

In the university campus where energy studies were conducted, natural gas consumption increased during the winter season due to the heating season; fell during the summer season. However depending on the use of air conditioning systems, it has been observed that electricity consumption increases in summer and there is not much change throughout the year. Average energy consumption percentage values with TEP conversion for natural gas 30% and for electricity consumption 70%. In addition, due to the high electricity unit prices, in terms of cost, on an annual basis natural gas cost was 15% and electricity was 85%. Accordingly, electricity constitutes the largest proportion in energy costs. When the relevant measures are taken, it is seen that there will be a decrease of 643.05 tons/year in CO_2 emission and it means 1.929 trees can be saved to the nature. Energy saving will bring also advantage both in terms of cost in continuing the activities of the institution; it will also pollute the environment less.

References

[1] TS 825, "Guidelines for Heat Insulation in Buildings" Standard

[2] Kedici O., "Enerji Yonetimi" Elektrik Isleri Etut Idaresi Genel Mudurlugu Enerji Kaynakları Etut Dairesi Baskanligi, 1993, Ankara, 2018.

[3] Genceli O.F., "Kalorifer Tesisati" TMMOB Makine Muhendisleri Odasi Yayin No: MMO/352/5 Istanbul, Mayis 2008

Boundary Layer Stability Impact on Wind Power

Fuat Berke Gul[1], Sevinc Asilhan Sirdas[2]
[1]fuat.gul@tau.edu.tr, Department of Energy Science & Technologies, Turkish-German
University, Istanbul, Turkey & Energy Institute, Istanbul Technical University,
Istanbul, Turkey
[2]sirdas@itu.edu.tr; ssirdas@gmail.com, Department of Meteorological Engineering,
Istanbul Technical University, Ayazaga Campus, Istanbul, Turkey

Abstract

Turbulence calculation is important in terms of the amount of energy the turbines will produce and the resistance of the turbines to extreme loads. Turbulence is the deviations of regular flow. Friction faced by flow and chaotic changes in velocity and pressure cause turbulence. There are many theorems and methods used for turbulence calculation. Some of these are K-theory (Eddy Diffusivity) and Power Law Expression. Calculation of turbulence is of great importance in order to improve wind forecasts. Thus, the amount of energy obtained from the wind can be calculated with higher accuracy and the regions where the wind energy farm will be established can be determined more precisely. Along with this study, wind turbulence calculation was carried out by wind data obtained from MILRES (National Wind Power Plant) turbine in Terkos, Istanbul region at different heights. In the light of these data, the distribution of energy output, wind speed, and wind direction was calculated both mathematically and by simulation. Based on the National Wind Power Plant (MILRES) turbine data, turbulence calculation was performed using Eddy Diffusivity and Power Law Expression methods. The results obtained were compared and the atmospheric stability of the region was examined using these results. During the considering period, each month was examined separately and the relationship between seasonal anomalies and turbulence was observed. Daily, monthly and seasonal deviations and changes were determined.

Keywords: Eddy Diffusivity, Reynolds Decomposition, Monin-Obukhov Similarity Theory, Boundary Layer.

Introduction

The energy obtained with coal, natural gas, and petroleum raw materials in the process to date; has led to the emergence of greenhouse gases, carbon emission formation, and global warming effects. These effects, which have emerged with the consumption of these resources, have caused the ecological balance to deteriorate and the emergence of a difficult world to live. The growing populations and developing economies of the countries have led to the rapid depletion of these energy raw materials and thus the search for alternative energies. The search for alternative energies that started in the late 19th century and continues today has shown mankind that it is possible to benefit from the sun, wind, water, and hydrogen. Solar and wind energy potential provide convenient installation and operating conditions for Turkey are frequently used in Turkey and their use is increasing year by year. Due to the geological structure and abundance of meteorological conditions including altitude, wind energy investments in Turkey are increasing day by day. When it comes to wind, making wind speed and direction estimates is very important [1].

The most challenging issue in wind prediction is turbulence. Wind speeds, which change rapidly, make estimation difficult, and can damage the blades and tower inside the turbine. In light of this information, it is very necessary to know and predict the turbulence created by the wind. Although there is no precise definition of turbulence, it is also difficult to predict when it will occur. Turbulence caused by fluctuations in the flow is related to the flow itself, not fluid [2]. The first 1000-2000 m layer of the atmosphere above the earth's surface is called the atmospheric or planetary boundary layer. Atmospheric conditions in this layer are determined by the vertical temperature gradient, vertical wind profile, and atmospheric stability. Atmospheric Stability describes the condition in which the atmosphere is located depending on the saturation, temperature, and movement of air parcels. An unstable atmosphere causes turbulence and severe weather conditions [3].

This study was carried out using methods such as Eddy Diffusivity, and Power Law Expression purposed to determine the effects of turbulence on wind and wind energy production. The methods that were revealed in the calculation of turbulence and the most frequently used methods in the literature were combined and calculations were made and compared. Thus, it was investigated which method gives more certain results about turbulence. Another aim of the study is to make energy production prediction in wind farms more consistent. Thus, it is aimed to reveal the production capacity, atmospheric stability, and turbulence effects of the region where the Wind Farm will be established. This study was realized as there are shortcomings regarding this subject in the literature. Unlike other studies in the literature, in this study, turbulence information was obtained using multiple turbulence calculation methods and the methods used were compared with each other. Thus, the advantages and disadvantages of these methods were evaluated.

Location and Data

MILRES (National Wind Power Plant) selected as the study area is located within the borders of the Terkos district and Istanbul province. It is located in the Marmara Region. The station is located at 41°18'N and 28°39'E coordinates. Measurements were made at 20, 40, 65, 80, and 81 meters with an anemometer. The height of the measuring location above sea level is 51 meters. Wind data are obtained with 10 minutes of measurement: temperature, pressure, relative humidity, potential temperature, wind speed intensity, and direction at five height levels and power generation. The measurement data includes the period between 1 August 2012 and 30 April 2013. The measuring station is a turbine project and power generation is also carried out. The area around this station consists of dense forest, city settlement, and a lake. There is a lake in the northern part and a small settlement in the eastern part (Figure 1). The station height from the standard pressure level is 51 meters. With the data obtained from the turbine, the histogram of the wind speeds for different levels was drawn and their parameters were determined by adapting to the Weibull distribution. The dominant wind directions and time series have been plotted for different levels by both statistical and analysis of wind data. The analysis shows that average wind speeds are higher in winter than in other seasons. The daily analysis shows that the average wind speed at night is higher than the daytime. The result of this analysis is valid every month.

Figure 1: MILRES measurement field and location.

Methods and Analysis

Eddy Diffusivity

Eddy Diffusivity Theory is one of the first-degree turbulent transport theories, also known as K-Theory. This theory is used to investigate small eddies. Wind energy estimation and sustainability depends on the correct modeling of atmospheric flows in the planetary boundary layer. Energy behaves like large vortices during turbulence flow. Over time, these vortices are divided into small vortices. Small vortices are divided into smaller vortices. The formation of these small eddies continues until the eddies reach the molecular scale. The energy obtained is converted into motion and heat in molecular form by the effect of viscosity [4].

$$\overline{\theta' w'} = -K \frac{\overline{\partial \theta}}{\partial z} \tag{1}$$

$$K = k^2 z^2 \mid \frac{\overline{\Delta M}}{\Delta z} \mid \tag{2}$$

Potential temperature gradient (θ) and Prandtl mixing length (K) are used to calculate the heat flow at different vertical heights (z). The turbulent flow rate is related to the K parameter and is called Eddy Diffusivity or Eddy Viscosity. k is the constant von Karman equal to 0.4. ΔM / Δz is a horizontal mean wind shear (M). θ 'and w' are expressed as to potential temperature gradient (θ) and vertical wind (w) turbulent or gust portions. This equation arises in windy conditions in the air, where the vortex is formed and the vortices are very small.

Power Law Expression

Mathematical models are often used to model the vertical profile of wind speed in homogeneous, flat terrain regions in wind energy studies. One of these models is the power-law equation. The power-law approach is exposed to uncertainties caused by the variable, complex nature of turbulent flows. The power-law expression provides information about wind shear between wind speeds at two different heights. Wind shear is shown as exponent (α) alpha in power-law expression. The alpha (α) value is called the power exponent. It is important that shear calculations are made only where upper and lower wind speed measurements are available for a given time interval. The value of α (alpha) varies depending on the time of day, season, temperature, altitude, atmospheric stability, and measurement zone [5].

$$u(z) = u_R \left(\frac{z}{z_R}\right)^{\alpha} \tag{3}$$

As a result of mathematical calculations, α value is considered as $1/7 \approx 0{,}14$ in many studies. When creating models, predictions are made using this value. However, 0.14 value in measurement data is not valid for many times. The fact that α value is different than 0.14 gives us ideas about turbulence.

WAsP

WAsP is a topological and meteorological simulation program used in wind farm modeling, revealing the effects of land conditions on wind potential. In this study, the power exponent and eddy diffusivity values were calculated by simulating the data obtained from the MILRES meteorology station and turbine in the WAsP program[6].

Results

Between 1 August 2012 - 30 April 2013, 10-minute wind speed measurements were made. As a result of these measurements, monthly average wind speeds were calculated. In order to calculate the effect of heat flux on turbulence in the atmospheric boundary layer, monthly eddy diffusivity values were calculated for heights of 65 and 40 meters (Figure 2). In some cases, wind measurements may have been made for a single height. For measurements that are not made at different heights, the Power Law is used to find the desired wind speed. Thus, wind speed estimations can be made for different heights based on wind speed data from a certain height. In this case, a mathematical model is created by accepting a value of α approximately 0.14 for a stable atmosphere. The fact that α takes values other than 0.14 and each deviation in this value gives information about instability and turbulence. Since α is found by giving wind speeds at different heights in the study, α values between successive heights have been calculated to have information about turbulence.

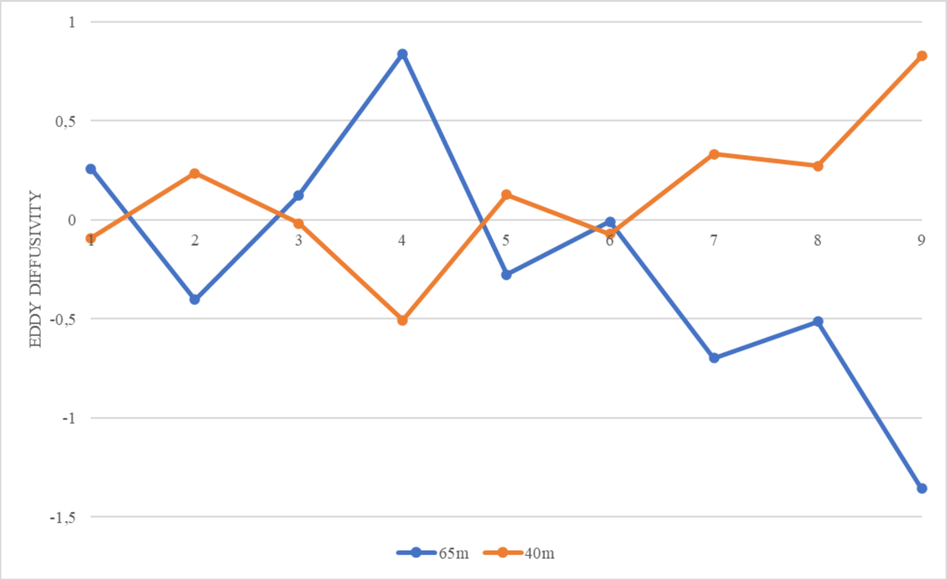

Figure 2: Monthly Eddy diffusivity at 65 and 40 meters.

After the performed calculations, the monthly average of the α value in December 2012, monthly in daytime hours, and monthly average in night-time hours were negative. Wind speed increases with increasing height, but the negative value of α indicates that the wind speed decreases with increasing height based on the power expression. This gives information about turbulence. For 81 and 80 meters measurements, the wind speeds at 81 meters are less than the wind speed at 80 meters during December 2012 (Figure 3).

Conclusion

In the analyses created by using wind speed data of different heights; According to the power expression law, it has been observed that the power exponent (α) taken as 1/7 in the literature is different from this value and in some cases it can exceed or decrease well below this value. Negative values of α indicate that turbulence is intense at this height and period. According to this, in December 2012, 80 meters of high turbulence was experienced. The neutral atmosphere is the most ideal of the five-atmosphere profiles in terms of the life cycle of the rotor. Because it has the lowest wind slip. However, in terms of the amount of power, an unstable atmosphere is more advantageous with higher wind intensity. The very stable atmosphere is the least advantageous of the five profiles due to the increased slip on the rotor diameter as well as the reduction in wind intensity. After Eddy Diffusivity and wind shear exponent calculation and WAsP simulation, it has been revealed that turbulence has a decreasing effect on the average wind speed for the measured heights. The decrease in wind speed reduced the power produced by

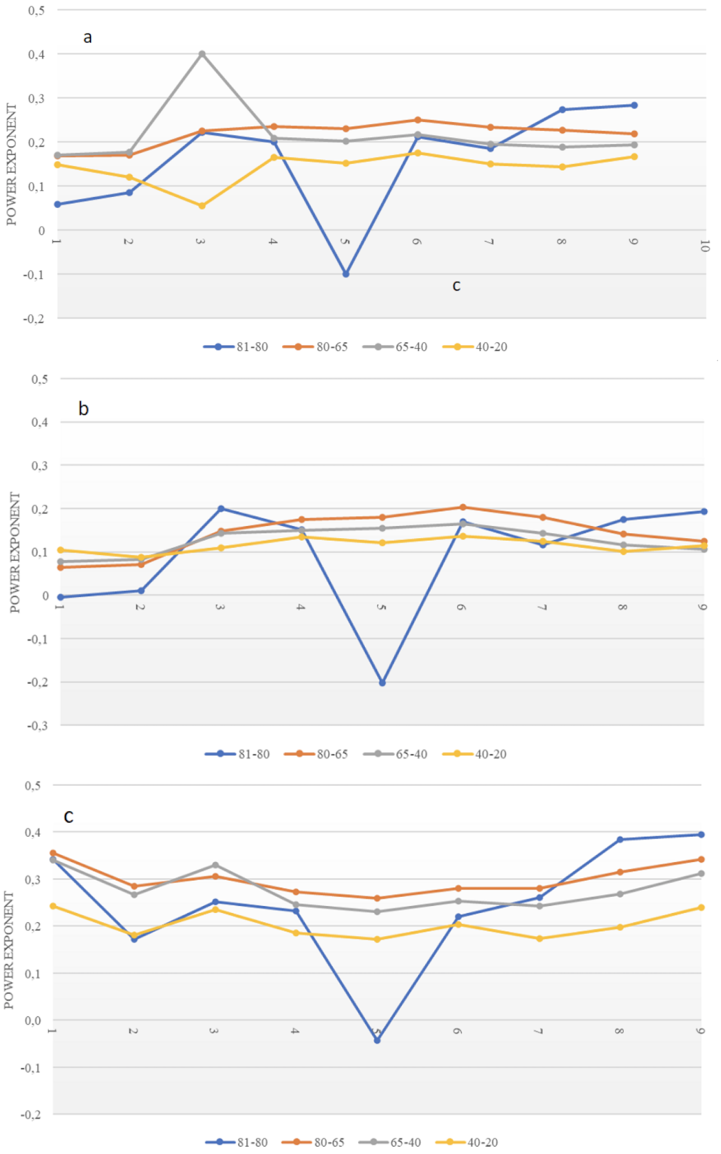

Figure 3: Power exponent a) monthly, b) monthly in daylight, c) monthly at night (August 2012 – April 2013).

the turbine. Wind power production values are needed to reveal the impact of turbulence on wind energy. Since we do not have wind power production data in this field of study, theoretical wind power values are taken into account. The instantaneous wind gust and speed-increasing turbulences that occurred during the period under consideration caused the turbine to be strained and the efficiency of the turbine to decrease by applying stress to the blades and the tower of the turbine.

References

[1] Asilhan, S. S. (2017). Eddy-Diffusion Turbulent Transport Theory for Wind Energy Application. IEEES-9

[2] Englberger, A., & Dornbrack, A. (2016). Impact of Neutral Boundary-Layer Turbulence on Wind-Turbine Wakes: A Numerical Modelling Study. Boundary-Layer Meteorology, 162(3), 427–449. `https://doi.org/10.1007/s10546-016-0208-z`

[3] Wharton, S., & Lundquist, J. K. (2012). Atmospheric stability affects wind turbine power collection. Environmental Research Letters, 7(1), 014005. `https://doi.org/10.1088/1748-9326/7/1/014005`

[4] Siebesma, A. P., Soares, P. M. M., & Teixeira, J. (2007). A Combined Eddy-Diffusivity Mass-Flux Approach for the Convective Boundary Layer. Journal of the Atmospheric Sciences, 64(4), 1230–1248. `https://doi.org/10.1175/jas3888.1`

[5] Farrugia, R. N. (2002). The wind shear exponent in a Mediterranean island climate. Renewable Energy, 28(4), 647–653. `https://doi.org/10.1016/s0960-1481(02)00066-6`

[6] Mortensen, N.G., D.N. Heathfield, L. Myllerup, L. Landberg and O. Rathmann (2007). Wind Atlas Analysis and Application Program: WAsP 9 Help Facility. Risø National Laboratory, Technical University of Denmark, Roskilde, Denmark. 353 topics. ISBN 978-87-550-3607-9.

Synthesis of Poly (methyl methacrylate) with Borax Decahydrate Addition for Energy Applications

Fuat Berke Gul[1], Nilgun Baydogan[2]
[1]fuat.gul@tau.edu.tr, Department of Energy Science & Technologies, Turkish-German University, Istanbul, Turkey & Energy Institute, Istanbul Technical University, Istanbul, Turkey
[2]dogannil@itu.edu.tr, Energy Institute, Istanbul Technical University, Ayazaga Campus, Istanbul, Turkey

Abstract

The modified polymer composites can be included as the substrate for the utilization at the photovoltaic-thermal collectors to generate solar electricity and heat in solar energy systems. Poly (methyl methacrylate) seems a suitable thermoplastic polymer due to high strength, high heat and abrasion resistance, and good mechanical properties. Chemical and physical properties of the poly (methyl methacrylate) can be improved by adding different filler materials. Borax decahydrate known as sodium tetraborate decahydrate is a soft, alkaline salt with excellent buffering and flow properties. In this study, the synthesis of polymer composite was performed by Atom Transfer Radical Polymerization for its use as a substrate at solar energy systems. Two different types of borax decahydrate ($Na_2B_4O_7.10H_2O$) (refined in both powder and crystal form from tincal ore) were used to increase the usage area of borax decahydrate in this study. Hence, borax decahydrate was added in poly (methyl methacrylate) as the filler material to improve surface properties with the enhancement of self-cleaning feature at composite surfaces, disposal of heavy contamination, removal of oil stains on polymer composite surface.

Keywords: Thermoplastic, Poly (methyl methacrylate), Sodium Tetraborate Decahydrate, Borax decahydrate, Atom Transfer Radical Polymerization, Polymer composite.

Introduction

Polymers are materials that are used in almost every area of the industry and have many advantages. PMMA is a type of thermoplastic polymer with high-temperature resistance, high strength, and good mechanical performance [1]. The characteristic structure of PMMA was given in Figure 1. In order to add new advantages to the positive features of PMMA, composite structures are created by combining them with different types of materials. Polymer composites are frequently used in areas requiring high strength, lightness, high temperature, and toughness such as automotive, energy, aviation, and aerospace [2].

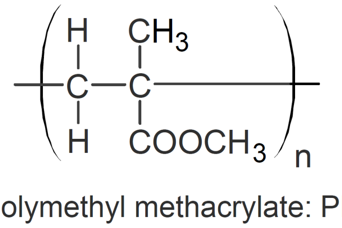

Figure 1: The structure of PMMA.

The ATRP technique is one of the well-known and easiest techniques among polymer production techniques. ATRP is an effective method for the preparation of polymers with controlled functionalities, topologies, and compositions. In this study, the ATRP method was used to make the polymerization process better and many times more adaptable than other polymerization methods with its functional groups. Thus, high quality polymerized PMMA/Borax polymer nanocomposites were produced [3, 4].

This study was carried out with the aim of determining the characteristic properties of PMMA/Borax composite synthesized by adding different amounts of Borax to the PMMA polymer material and gaining deep insight about polymer composites such as preparation and characterization methods. Besides, the other purpose of this study is understanding the influence of Borax on Poly(methyl methacrylate) (PMMA) polymer matrix such as interactions with the polymer matrix and the corresponding improvements of surface morphology. Because the surface morphology affects the mechanical, thermal, and electrical properties of PMMA.

Experiments

1. Synthesis of PMMA/borax polymer composites

The used chemicals were $C_5H_8O_2$ Methyl Methacrylate (MMA) as a monomer, CuBr Copper Bromide as a catalyst, $C_{16}H_{36}BrN$ Tetra-n-butylammonium Bromide (Bu_4NBr) as solvent, $C_6H_{11}BrO_2$ Ethyl 2-bromoisobutyrate (EBIB) as initiator, $C_9H_{23}N_3$ 1,1,4,7,7- Pentamethyldiethylenetriamine (PMDETA) as Ligand and Multi-Walled Carbon Nanotubes (MWCNTs) as nanoparticles. The chemicals were prepared and a two-handed Atmos-Bag filled with Argon gas. All chemicals were weighed separately in two-handed Atmos-Bag. Then, the solvent Bu_4NBr (3.76 mmol, 1.211 g) and the catalyst CuBr (0.47 mmol, 0.067 g) were added to MMA monomer (0.282 mol, 28.2 g) with different quantity of Borax such as 7,5% wt. with Crystal Bu_4NBr and 7.5% wt. with Powder Bu_4NBr. All of these chemicals were in solid form and were mixed in two-handed Atmos-Bag. After adding Borax, this mixture was removed from Atmos-Bag and was transferred to another Atmos-Bag. This Atmos-Bag also was filled with Argon gas.

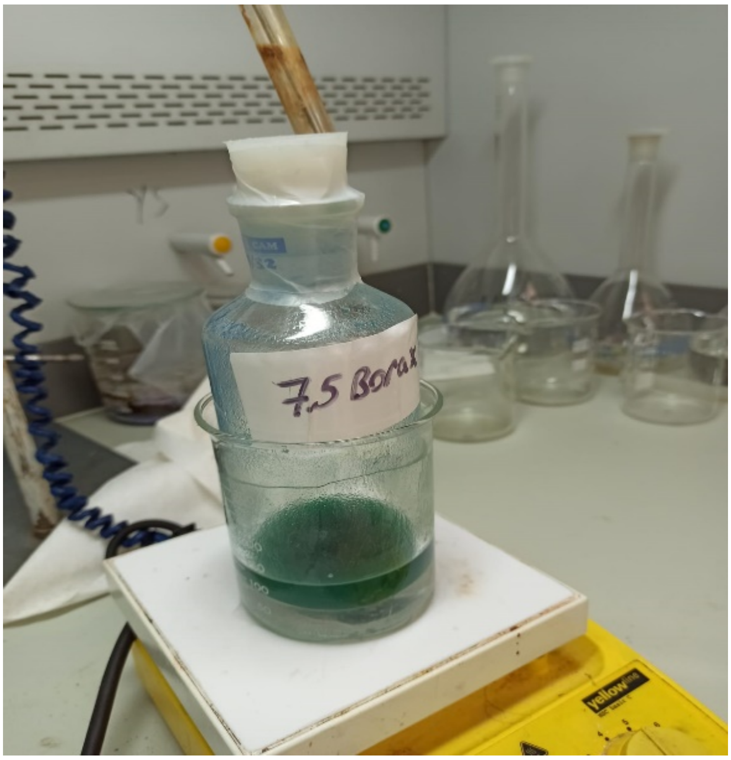

Figure 2: PMMA/borax composite on magnetic stirrer.

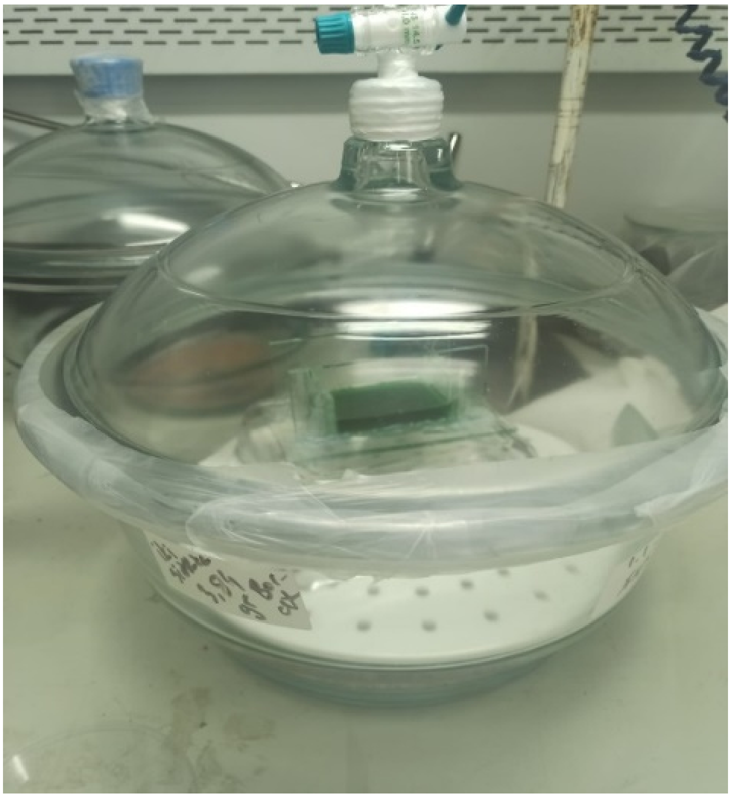

Figure 3: PMMA/borax composite in desiccator.

After that, Pentamethyldiethylenetriamine (PMDETA) (0.47mmol, 0.081 g), was inserted to the admixture and the admixture was degassed. The gas-tight syringe was utilized to realize the degas process for 5 minutes. Then Ethyl 2-bromoisobutyrate (EBIB) was added to this mixture. The polymerization process started after the addition of EBIB (0.47 mmol, 0.092 g) into the tubes. A magnetic stirrer with a silicone bath was utilized to provide better conditions for mixing. The mixture was removed from Atmos-Bag and placed in this stirrer in Figure 2. This magnetic stirrer allowed the temperature to be adjusted manually, keeping temperature characteristics under control. This mixing has been continued until the polymerization was completed. After polymerization, the sample is taken from the magnetic stirrer and placed into the desiccator (Figure 3).

2. Stereo microscope imagination

A Stereo Microscope was used to view the surface topographies of the samples in 3D (Figure 4). Thus, information about the surfaces of the samples was obtained.

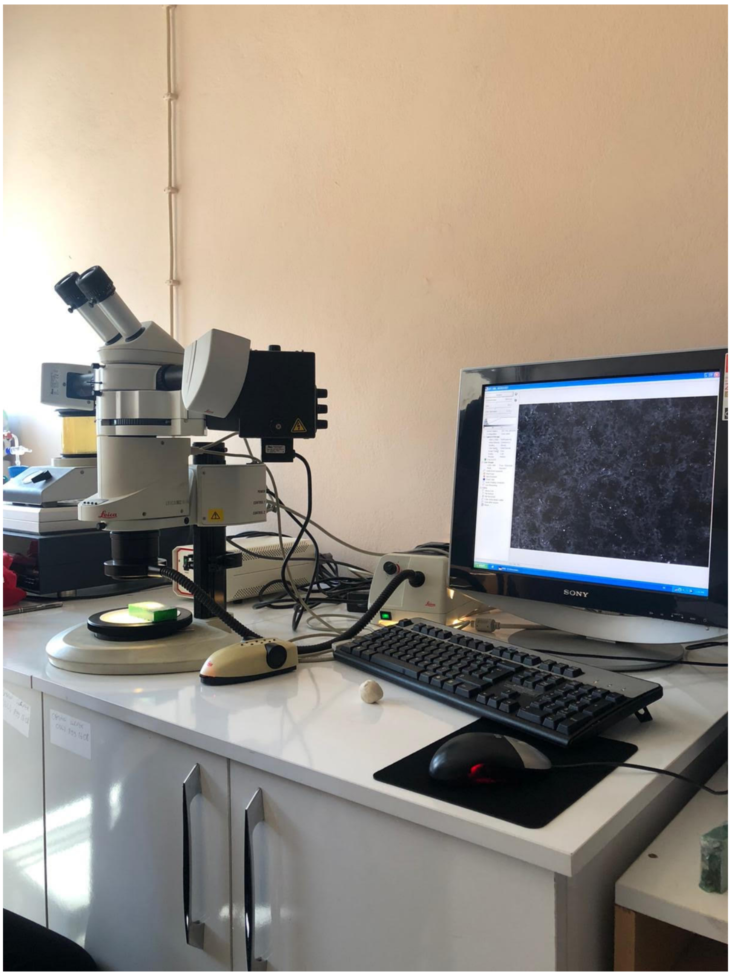

Figure 4: Stereo-microscope measurement.

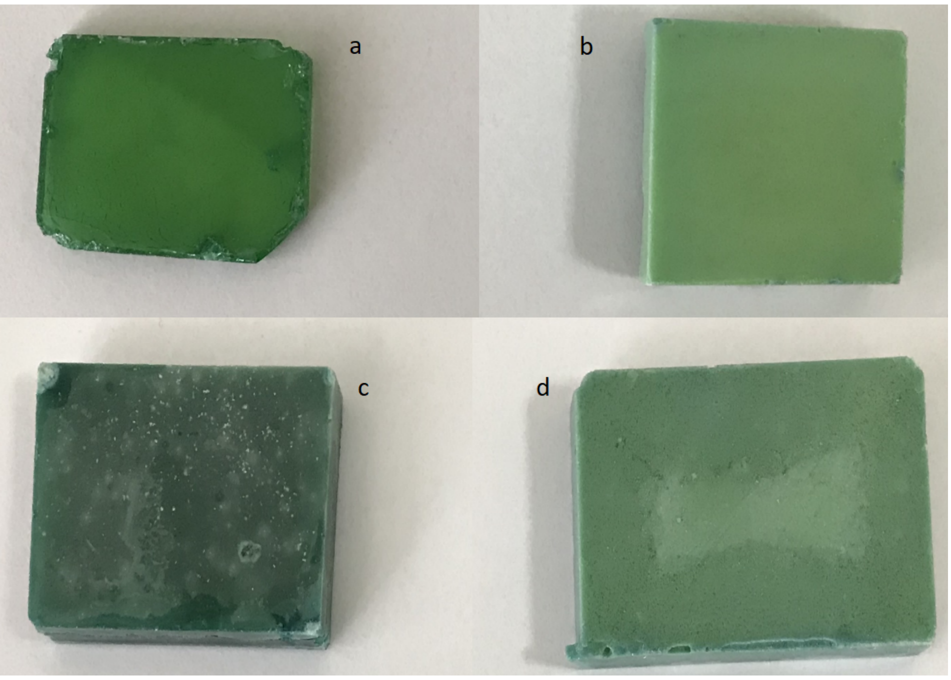

Figure 5: a) Base PMMA with crystal Bu_4NBr, b) base PMMA with powder Bu_4NBr, c) 7,5% wt. borax with crystal Bu_4NBr, d) 7,5% wt. borax with powder Bu_4NBr.

Results and Discussion

Four different PMMA samples were produced in this study (Figure 5). Two different base PMMAs were produced with the crystal and powder Bu_4NBr (Figure 5a and 5b). In addition, PMMA/Borax polymer composites containing 7,5% wt. Borax were also produced with crystal and powder Bu_4NBr (in Figure 5c and 5d).

The surface morphologies of PMMA/Borax samples in Stereo Microscope images were shown in Figures 6 and 7 with different magnifications that are 10x, 20x, and 50x. Stereo Microscope image of 7,5% wt. Borax with crystal Bu_4NBr PMMA/Borax provides to understand how the addition of Borax affects the surface morphology comparing with base PMMA. Besides, the Stereo Microscope image of base PMMA with crystal Bu_4NBr provides to understand how the physical structure of Bu_4NBr affects the surface morphology comparing with base PMMA with powder Bu_4NBr.

Conclusions

Base PMMA and 7,5% wt. Borax included PMMA/Borax composites were synthesized. Two different types of Bu4NBr were used and the differences between optical properties and surface qualities were determined. ATRP method was used for the synthesis of PMMA/Borax composite samples. Stereo microscope images of each sample were taken and their surface morphologies were examined.

The optical properties of Base PMMA produced with Crystal Bu_4NBr and

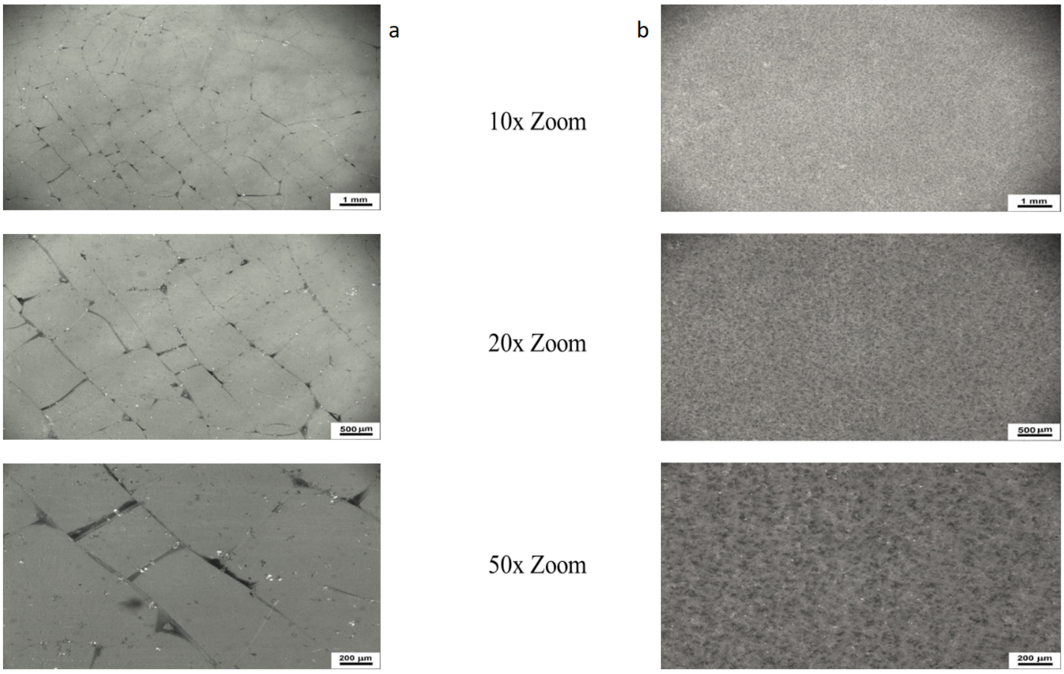

Figure 6: Base PMMA with a) crystal Bu_4NBr, b)powder Bu_4NBr.

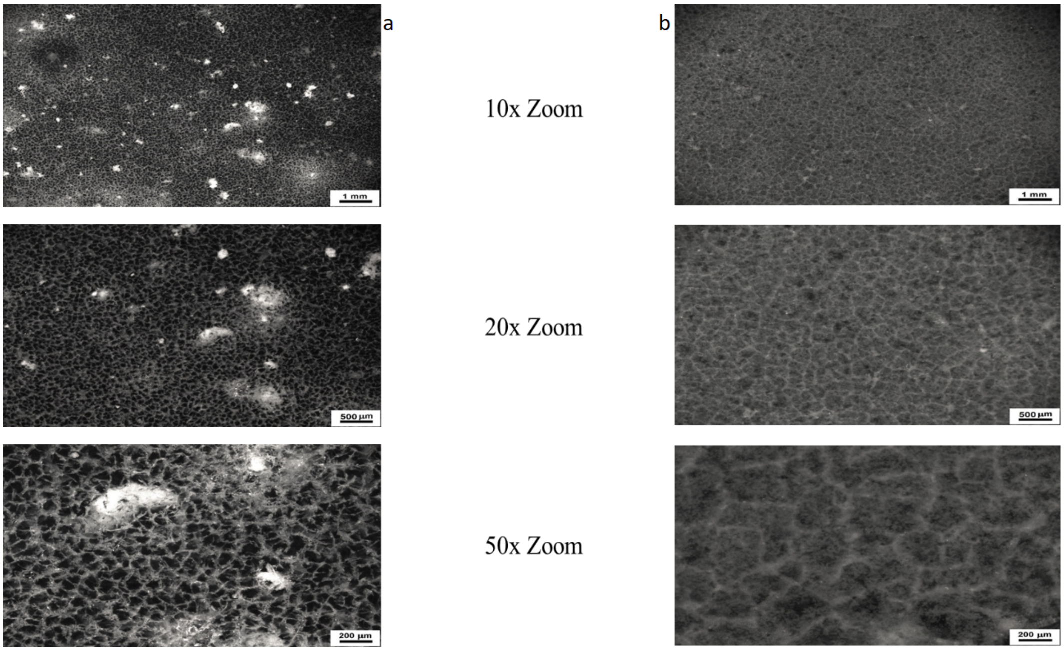

Figure 7: 7,5% wt. borax/PMMA with a) crystal Bu_4NBr, b) powder Bu_4NBr

Powder Bu_4NBr were different from each other. Samples produced with the crystalline Bu_4NBr are optically more permeable and transparent, while the samples produced with powder Bu_4NBr are opaque. The results are the same for both 7,5% wt. Borax included PMMA/Borax composites. It was determined that Borax material was homogeneously dispersed in PMMA by PMMA/Borax synthesis. There is no crack at the surface morphology of all samples.

References

[1] Khan, W.S., Hamadneh, N.N., Khan, W.A. (2017). Polymer nanocomposites–synthesis techniques, classification and properties, Science and Applications of Tailored Nanostructures, One Central Press, USA, 2017.

[2] Sahoo, N. G., Rana, S., Cho, J. W., Li, L., & Chan, S. H. (2010). Polymer nanocomposites based on functionalized carbon nanotubes. Progress in Polymer Science, 35(7), 837–867. `https://doi.org/10.1016/j.progpolymsci.2010.03.002`

[3] Bel, T., Yahya, N., Cimenoglu, H., Arslan, C., & Baydogan, N. (2018). The Examination of the Changes in the Magnetic Properties of the Poly(methyl methacrylate). Journal of Physics: Conference Series, 1123, 012005. `https://doi.org/10.1088/1742-6596/1123/1/012005`

[4] Liao, W., Gu, A., Liang, G., & Yuan, L. (2012). New high performance transparent UV-curable poly(methyl methacrylate) grafted ZnO/silicone-acrylate resin composites with simultaneously improved integrated performance. Colloids and Surfaces A: Physicochemical and Engineering Aspects, 396, 74–82. `https://doi.org/10.1016/j.colsurfa.2011.12.044`

Using of Renewable Energy System to Heat a Private Swimming Pool in Gaziantep

Reyhan Ilgaz[1], Recep Yumrutas[2]
[1]reyhan-ilgaz@hotmail.com, Department of Mechanical Engineering, Gaziantep University, Gaziantep, Turkey
[2]yumrutas@gantep.edu.tr, Department of Mechanical Engineering, Gaziantep University, Gaziantep, Turkey

Abstract

Swimming pools are considered as high energy demand sport facilities. The development of new heating systems to reduce the energy consumption of the heated swimming pools is important (i.e. using of renewable energy). The present work illustrates the thermal analysis of heating system for a private swimming pool located in Gaziantep, Turkey. The heating system consists of solar collector, energy storage tank, heat pump and swimming pool. The swimming pool heating system is suggested to be worked thought the four seasons of the year. Based on computer simulation, an analytical model is introduced to predict the performance of heating operation for several years. The analysed results show that the system can attain an annually periodic operating condition. Furthermore, the coefficient of performance (COP) of heat pump significantly influenced by collector area and TES tank volume.

Keywords: Swimming pool, heat pump, solar energy, thermal energy storage tank.

Introduction

Swimming pools, representing significant sports facilities, are very intensive in the use of energy. This great energy demand limits the financial viability of these high-demand installations, mainly for public swimming pools where fair prices for users result in a deficit balance that requires public spending to keep them open.

In general, a great amount of energy in the world is consumed for heating applications such as space and swimming pool heating, industrial heating processes. The utilization of large scale consumption of fossil fuels causes reduction of natural sources such as fossil fuels, increment of CO_2, SO_x and NO_x emissions to the atmosphere and expenditure of money for countries importing fossil fuels [1, 2]. For these details, researches are focused on utilization of renewable energy sources and waste energy. Thermal energy storage (TES) systems can be a good solution due to the possibility of their wide utilization. There are some advantages of the TES systems which can reduce the initial investment and operating costs [3].

The storage of solar energy is an alternative type of renewable energy sources. Solar energy is the most important energy source. Utilization of the solar energy for heating applications is very significant. But, there is less or no heating requirement for heating of the swimming pools although the solar energy is plenty during summer season. Great energy is necessary for heating of the swimming pools in winter. That is, there is a mismatch situation between solar energy supply and energy requirement of the swimming pools. In order to solve this problem, the solar energy can be stored during whole year, and it can be used as heat source of a heat pump during winter season. Since, heating systems with heat pumps are the energy efficient and saving systems [4–6].

Ground Coupled Heat Pump (GCHP) systems have been gaining popularity as they reduce energy consumption compared to conventional air source heat pump systems [7, 8]. Since the temperature in deep earth is very stable, the soil is an ideal heat sink in the summer and an ideal heat source in the winter [9]. However, compared to air source heat pump systems, GCHP systems have not been widely used. This may be attributed to comparatively higher installation costs and ground area requirements.

Various theoretical and experimental studies have concentrated on the analysis and optimization of swimming pool heating systems. Kincay et al. [10] examined the technical and economic performance of solar energy utilization in swimming pools. They calculated the optimum collector surface area for swimming pools. Chow et al. [11] observed a solar-assisted heat pump system for heating indoor swimming pools and spaces. Li et al. [12] developed a computer simulation platform to optimize the volume of a phase change material storage tank. A thermal analysis and modelling of the system which consisted of an ice rink and a swimming pool coupled by a chiller unit were conducted by Kuyumcu and Yumrutas [13].

Due to the multiple advantages, a theoretical model for the solar assisted heat pump swimming pool (SAHP) heating system with underground TES tank is investigated in the present study. The mathematical model for the pool heating system is developed in MATLAB program by using different input data to find performance parameters for swimming pool heating system. These parameters are temperature of water in the TES tank, Coefficient of performance of the heat pump.

Description of Heating System

The heating system is shown schematically in Figure 1. SAHP swimming pool heating system consist of four main sections; flat plate solar collectors, an underground energy storage tank, a Ground Source Heat Pump (GSHP), and a swimming pool to be heated in winter season. The solar collectors are used to charge solar energy into the water in the TES tank during the entire year; also the solar collectors operate during the useful solar energy is available. TES tank is the most important part of the heating system providing energy savings and contributing to the reduction of environmental pollution. The heat pump is another part of the system is coupled to the TES tank. Heat pump supplies the swimming pool with heat. The swimming pool is located at private residential in the city of Gaziantep in Turkey, which lies between 37° 4' latitude N and 37° 29' longitude E and has a Mediterranean climate.

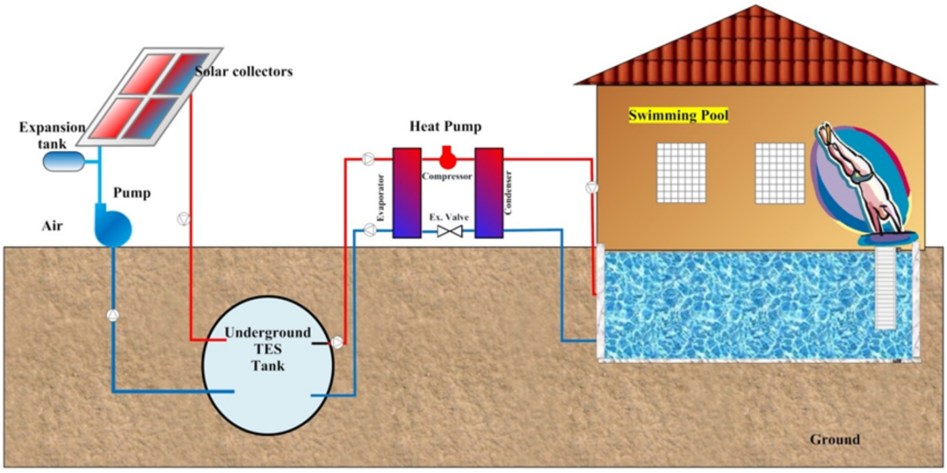

Figure 1: Schematic of the swimming pool heating system.

Mathematical Modelling

1. Unsteady heat transfer problem around the TES tank

The considered TES tank for the thermal modelling is spherical in shape and filled with water. The water in TES tank is primarily considered at the deep ground temperature T_∞ and water temperature varies with a spatially lumped time varying temperature $T_w(t)$. In addition, the water is supposed to be fully mixed in the tank. The TES tank is suggested to be surrounding by a soil having homogeneous texture and specific thermal properties.

The mathematical formulations of the unsteady heat transfer problem related with spherical TES tank are given by a differential equation as a function of initial and boundary conditions. These are as the following illustration:

$$\frac{\partial^2 T}{\partial r^2} + \frac{2}{r}\frac{\partial T}{\partial r} = \frac{1}{\alpha}\frac{\partial T}{\partial t} \tag{1}$$

$$T(R,t) = T_w(t) \tag{2}$$

$$T(\infty,t) = T_\infty \tag{3}$$

$$T(r,0) = T_\infty \tag{4}$$

The dimensionless net heat input rate to the TES tank [14, 15]:

$$q(\tau) = q_u(\tau) - q_{sp}(\tau) + \frac{w(\tau)}{\gamma} \tag{5}$$

where $q_u(\tau)$ denotes the dimensionless energy collection rate by solar collectors. $q_{sp}(\tau)$ and $w(\tau)$ are designations of dimensionless heat demand of the swimming pool and the GSHP work, respectively. γ is the dimensionless parameter, $\gamma = 4\pi\mathrm{Rk}/(\mathrm{UA})_{sp}$.

2. Hourly useful solar energy collection rate

The collector efficiency is a function of the solar tilted radiation and temperature difference between inlet fluid and ambient air temperatures:

$$\eta_c(t) = 0.72 - 6.4\frac{[T_w(t) - T_a(t)]}{I_T(t)} \tag{6}$$

3. Heat requirement of the swimming pool

Total energy requirements for a swimming pool are yielded from the convection, conduction, evaporation, radiation, and renovated feed water heat loss components. Total energy can be expressed as:

$$Q = Q_{conv} + Q_{con} + Q_{eva} + Q_{rad} + Q_{ren} \tag{7}$$

4. Energy requirement of the heat pump

By using the dimensionless variables, the heat pump COP can be obtained as follows:

$$COP = \eta_c \frac{u_{sp}[\varphi_p - \varphi_a(\tau)] + \varphi_p + 1}{u_{sp}[\varphi_p - \varphi_a(\tau)] + \varphi_p - \varphi_w(\tau)} \tag{8}$$

The dimensionless compressor work requirement can be expressed as:

$$w = \frac{[\varphi_p - \varphi_a(\tau)][u_{sp}[\varphi_p - \varphi_a(\tau)] + \varphi_p - \varphi_w(\tau)]}{\eta_c[u_{sp}[\varphi_p - \varphi_a(\tau)] + \varphi_p + 1]} \tag{9}$$

Computation of performance parameters

In the calculations, by using data for hourly solar radiation and outside ambient temperature the useful solar energy gain is calculated using Equation (6), the proper expression for collector efficiency recommended by Yumrutas and Kaska [16], winter design indoor and outdoor temperature is 20 °C and -9 °C respectively, pool water temperature taken as 26 °C, Carnot efficiency was taken as 0.4, storage volume is taken as different values. Proposed swimming pool area is 25 m^2. In addition, COP of the heat pump is calculated hourly, monthly and yearly using the inside design air temperature, and the hourly outside temperatures. These determinations were performed on an hourly basis for sufficient number of years until the annual temperature distribution of the TES tank attains annually periodic operating conditions.

Results and Discussion

Long term variation of water temperature of the TES tank during the first year of operation for the three different types of earth (coarse gravel, limestone, and granite) is shown in Figure 2. It is seen from this figure that the water temperatures in the TES tank are highest at the end of summer and lowest at the end of winter. Regarding the ground type that surrounding TES tank, it can be inferred from these results that the highest stored temperature belongs to coarse gravelled earth, whilst the lowest belongs to granite. Such behaviour is attributed to thermophysical properties of earth type, which are identified by thermal conductivity, specific heat, density, heat capacity and thermal diffusivity.

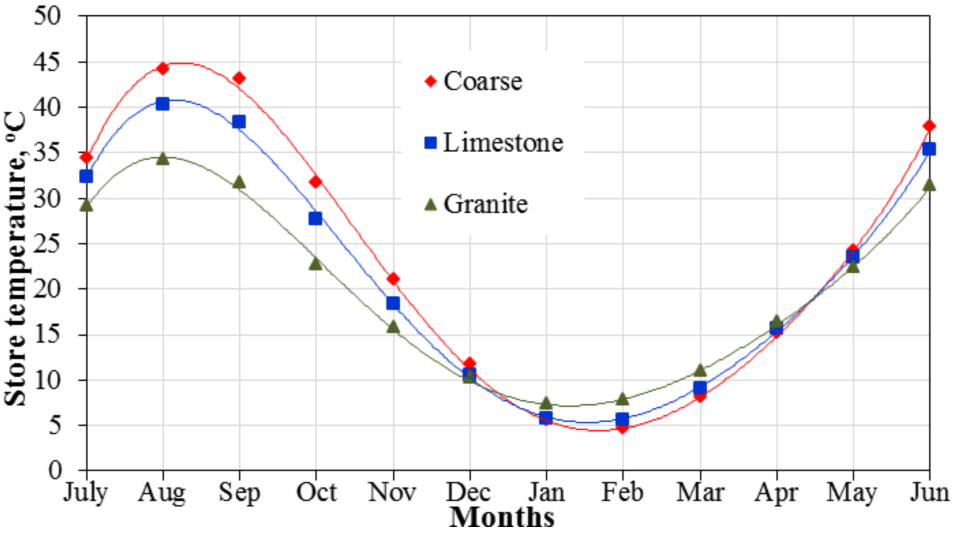

Figure 2: Monthly temperature variation of water in the TES tank during the first year.

The effect of solar collector surface area on heat pump COP values with respect to pool surface area of 25 m^2 during the first year of system operation is presented in Figure 3. It is observed that the COP values increases with the collector area.

With respect to first, second, fifth and sixth years of operation the annual variation of water temperature in the TES tank buried in limestone type earth is presented in Figure 4. It is clearly seen that the annually periodic operating conditions are achieved after the fifth year of operation.

Conclusion

In this study, mathematical model of heating system for a swimming pool having area of 25 m^2 is developed to investigate the long-term thermal performance parameters for the heating system. Performance parameters are hourly, monthly and yearly temperatures of water in the TES tank, and coefficient of performance of the heat pump (COP). The following important conclusions are drawn:

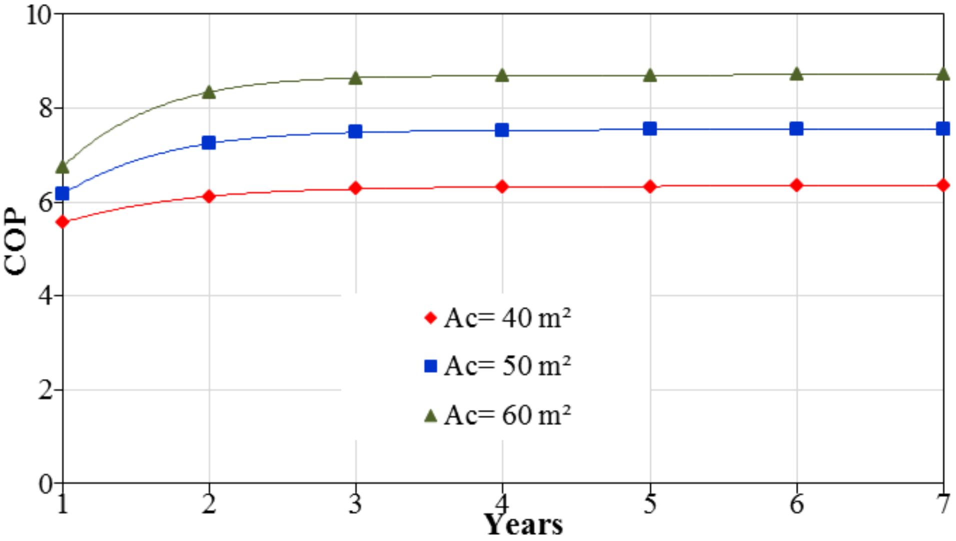

Figure 3: Effect of solar collector area on the heat pump COP.

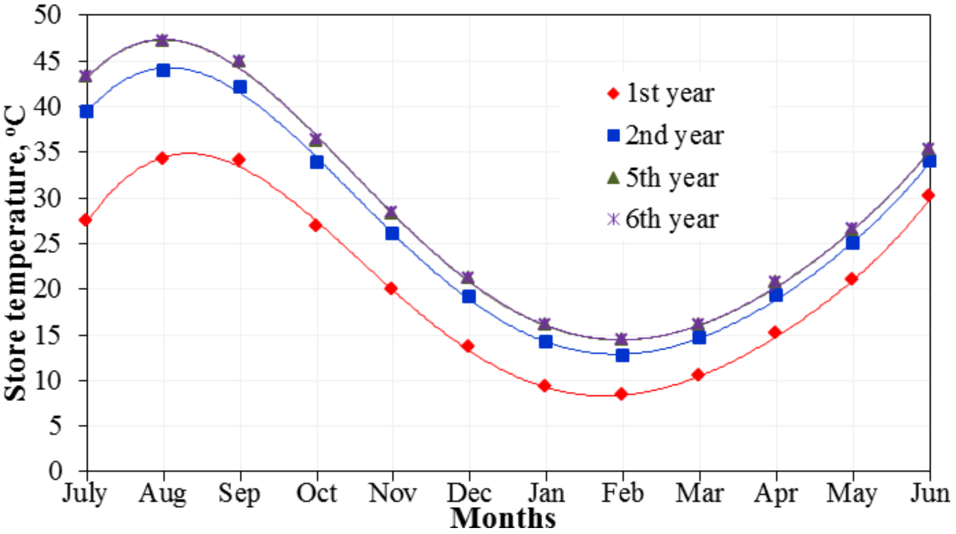

Figure 4: Temperature variation of water in the TES tank ($A_{sp} = 25$ m^2, $A_c = 50$ m^2, V = 200 m^3).

1. Results indicate that 5-7 years will be sufficient for the swimming pool heating system under investigation to reach an annually periodic operating condition.
2. The highest storage temperature occurs when the TES tank is embedded in coarse gravelled earth and the lowest water temperature occurs when the storage is buried in granite.
3. The ideal design parameters of the heating system are obtained as 50 m^2 collector area and 300 m^3 storage tank volume.

References

[1] Novo, A. V., Bayon, J. R., Castro-Fresno, D., & Rodriguez-Hernandez, J. (2010). Review of seasonal heat storage in large basins: Water tanks and

gravel–water pits. Applied Energy, 87(2), 390–397. https://doi.org/10.1016/j.apenergy.2009.06.033

[2] Rahman, S. (2010). Energy, economics and environmental analysis for chillers in office buildings. Energy Education Science and Technology Part A: Energy Science and Research, 25, 1-16.

[3] Basaran, T. Sumbul, N. (2011).The performance of a cool storage system in various operation conditions and its economic analysis. Energy Education Science and Technology Part A: Energy Science and Research. 26(2), 251-264.

[4] Kuyumcu, M. E., Tutumlu, H., & Yumrutas, R. (2016). Performance of a swimming pool heating system by utilizing waste energy rejected from an ice rink with an energy storage tank. Energy Conversion and Management, 121, 349–357. https://doi.org/10.1016/j.enconman.2016.05.049

[5] Unsal, M., Yumrutaş, R. (2012). Modeling and performance analysis of a solar assisted house heating system with heat pump and energy storage tank. Solar Energy. 86, 983-993.

[6] Forsstrom, J. P., Lund, P. D., & Routti, J. T. (1987). Economic analysis of heat storage in energy systems. International Journal of Energy Research, 11(1), 85–94. https://doi.org/10.1002/er.4440110108

[7] Hepbasli, A. (2002). Performance evaluation of a vertical ground-source heat pump system in Izmir, Turkey. International Journal of Energy Research, 26(13), 1121–1139. https://doi.org/10.1002/er.839

[8] Hepbasli, A., Akdemir, O., Hancioglu, E. (2003). Experimental study of a closed loop vertical ground source heat pump system. Fuel and Energy Abstracts, 44(4), 254. https://doi.org/10.1016/s0140-6701(03)82141-0

[9] Zhang, H.-F., Ge, X.-S., & Ye, H. (2007). Modeling of a space heating and cooling system with seasonal energy storage. Energy, 32(1), 51–58. https://doi.org/10.1016/j.energy.2006.02.007

[10] Kincay, O., Utlu, Z., & Akbulut, U. (2011). Technical and Economic Performance Analysis of Utilization of Solar Energy in Indoor Swimming Pools, An Application. Journal of Solar Energy Engineering, 134(1), 014502. https://doi.org/10.1115/1.4005106

[11] Chow, T. T., Bai, Y., Fong, K. F., & Lin, Z. (2012). Analysis of a solar assisted heat pump system for indoor swimming pool water and space heating. Applied Energy, 100, 309–317. https://doi.org/10.1016/j.apenergy.2012.05.058

[12] Li, Y., Ding, Z., & Du, Y. (2020). Techno-economic optimization of open-air swimming pool heating system with PCM storage tank for winter applications. Renewable Energy, 150, 878–890. https://doi.org/10.1016/j.renene.2020.01.029

[13] Kuyumcu, M. E., Tutumlu, H., & Yumrutas, R. (2016). Performance of a swimming pool heating system by utilizing waste energy rejected from an ice rink with an energy storage tank. Energy Conversion and Management, 121, 349–357. `https://doi.org/10.1016/j.enconman.2016.05.049`

[14] Yumrutas, R., & Unsal, M. (2000). Analysis of solar aided heat pump systems with seasonal thermal energy storage in surface tanks. Energy, 25(12), 1231–1243. `https://doi.org/10.1016/s0360-5442(00)00032-3`

[15] Yumrutas, R., Kunduz, M., & Ayhan, T. (2003). Investigation of thermal performance of a ground coupled heat pump system with a cylindrical energy storage tank. International Journal of Energy Research, 27(11), 1051–1066. `https://doi.org/10.1002/er.932`

[16] Yumrutas, R., & Kaska, O. (2004). Experimental investigation of thermal performance of a solar assisted heat pump system with an energy storage. International Journal of Energy Research, 28(2), 163–175. `https://doi.org/10.1002/er.959`

Effect of Mixing Ratio of Binary Mixtures on Heat Transfer Characteristics of a Pulsating Heat Pipe

Burak Markal[1], Ramazan Varol[2]
[1]burak.markal@erdogan.edu.tr, Department of Energy Systems Engineering, Recep Tayyip Erdogan University, Rize, Turkey
[2]rmznvaroll@gmail.com, Department of Energy Systems Engineering, Recep Tayyip Erdogan University, Rize, Turkey

Abstract

This study deals with investigation of heat transfer and flow characteristics in an asymmetrical PHP charged by binary mixtures with different mixing ratios. The PHP has sixteen parallel rectangular channels, in other words, it consists of eight turns. One of the channels in a turn has 2 mm x 2 mm; while the neighbouring one has 1 mm x 2 mm cross section. In the mixture, ethanol (E) and hexane (H) are used as fluids. The experiments are conducted at a constant filling ratio of 40%; but different mixing ratios (E:H = 1:1, 1:4 and 4:1) and inclination angles are studied, too. At each test condition, heating power gradually increases up to nearly 110 °C (as evaporator temperature), and then relevant experiment is terminated. Flow images are also taken; and they are used in the discussion of the results (as flow patterns and dynamics of flow components). Important conclusions are obtained through the study. Increasing volume ratio of ethanol in the mixture adversely affects thermal performance at both the inclination angles. Generally, dependence of thermal resistance trend on the inclination angle is not significant; this dependence is relatively more obvious for E:H = 1:1 mixture compared to the other mixing ratios. However, in terms of heat input range, it may be stated that thermal performance at vertical position is better than the horizontal one due to higher maximum achievable heating power.

Keywords: Heat transfer, mixing ratio, pulsating heat pipe, binary mixture.

Introduction

In today's world, technology rapidly progresses, and thermal control becomes a critical case in terms of sustainability and advancement of electro-mechanical systems. In this context, heat pipes, more specifically, pulsating heat pipe (PHP) as a member of that family, draw the much attention. Passive operational characteristics and wickless structure make the PHPs promising devices among advanced thermal management methods. As stated in literature [1], PHPs have wide range of application fields such as desalination systems, cooling of electro-mechanical systems, solar collectors, etc. There are many efforts dealing with pulsating heat pipes.

Khandekar et al. [2] experimentally studied a copper PHP having 2 mm inner tube diameter. Three different fluids (ethanol, water and R-123) were utilized in heat pipe. It was concluded that system charged with any of fluids did not work at horizontal orientation as a result of less turn number. Optimum filling ratio interval was defined as 25-65%. Qu et al. [3] focused on oscillation behavior of wall temperature via non-linear analysis. They stated that minimum independent variable number is four to describe PHP heat transfer characteristics. Fumoto et al. [4] performed experiments with a pulsating heat pipe (PHP) filled with a self-rewetting fluid (1-butanol-1-pentanol-water mixture). By means of self-rewetting fluid, heat transport ability increased nearly four times. The basic underlying reason is prevention of the dryout. Saha et al. [5] investigated PHPs for four different working fluids as acetone, methanol, water and 2-Propanol. A constant filling ratio (50%) is preferred for horizontal and vertical orientations. At vertical orientation water was decided as the best working fluid; while when the PHP is placed horizontally, methanol showed best performance. Pachghare and Mahalle [6] conducted experiments via a capillary type PHP having ten turns. Pure (acetone, ethanol, methanol, water) and their binary mixtures were used as fluids during the tests. Pure acetone was determined as the best working fluid; and binary and pure fluids presented similar thermal performance. Han et al. [7] basically focused on fluids' thermo-physical properties, and experimentally investigated thermal characteristics of a PHP charged with ethanol, water, acetone and methanol. Dynamic viscosity was stated as dominant property at low heat loads. On the other hand, latent heat and specific heat gained importance at relatively higher heat loads. Yang et al. [8] conducted experiments to examine thermal characteristics of a non-uniform micro PHP filled with methanol or water. Only the PHP having methanol with filling ratio of 80% presented pulsating flow. Cui et al. [9] focused on binary mixtures formed by mixed acetone, water or ethanol with methanol. General results were grouped depending on filling ratio; such that, water and methanol mixture showed efficient performance against dryout at low filling ratio (45%). However, at greater filling ratios than 45%, binary mixture and single fluids presented similar behaviour. Another study focusing on working fluid role on the performance of a closed loop PHP was conducted by Patel et al. [10]. Pure fluids, binary mixture and water-based surfactant solutions were used as working fluid (ethanol, water, acetone, methanol, sodium dodecyl sulphate). Filling ratio and orientation were constant as 50% and vertical (bottom heat mode), respectively. Among pure fluids acetone was the best fluid. Performance of binary mixtures was amid the relevant components. Wang at al. [11] experimentally studied closed loop PHP performance by modifying surface of flow passages with aim of obtaining different wettability. Hydrophobic surface provided superior thermal characteristics at relatively low heat inputs; while hydrophilic one was better at high heating powers.

The aim of the present study is to report and discuss experimental results (heat transfer and flow analysis) obtained for an asymmetrical PHP charged by binary mixtures with different mixing ratios. Experiment range covers novel parametric combination, and experiments are conducted at different mixing ratios and inclination angles for a constant filling ratio of 40%. Flow is visualized and flow patterns are presented for different conditions.

Experimental Setup, Data Reduction and Details

The experimental apparatus designed to make experiments is demonstrated via Figure 1. There are three main components in the system: (1) flat-plate closed loop pulsating heat pipe, (2) heat sink and (3) heating piece. Also, to make these three components functional, there are some other systems as circulation line, data acquisition system, visualization system, heating unit and measuring tools (thermocouples).

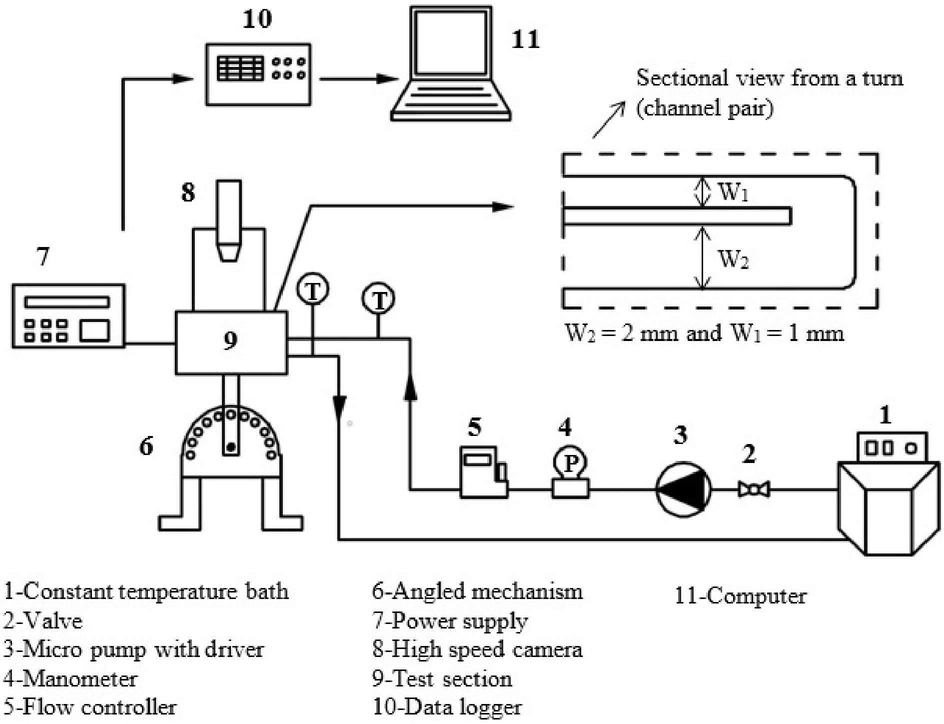

Figure 1: Experimental apparatus with PHP details.

Heat pipe mainly is a 4 mm thick copper plate having sixteen interconnected parallel channels or eight turn. Channel height is 2 mm; while in a turn, one of the parallel channels has 2 mm wide and other one has 1 mm wide. Details are shown in Fig 1. On the bottom surface of PHP plate, for thermocouple placements, channels having 1 mm depths are engraved. PHP consists of three classical regions as evaporator, adiabatic and condenser; and for each region, three thermocouples are glued. Also, a glass cover is placed over the PHP plate to ensure a leak-proof medium and to make the visualization possible.

Evaporator and condenser regions of the heat pipe are placed over the heating piece and heat sink, respectively. Heating piece includes two heaters of which the cables connected to a power supply. On the other hand, heat sink is connected to circulation line, and there are flow passages in heat sink. Cooling water flowing in these flow passages removes thermal energy from condenser region. To determine the removing heat from condenser region, flow rate of cooling water is set to a constant value of 20 ml min-1 and temperature readings are performed at the heat sink inlet and outlet. Also, in the experiments, inlet temperature of cooling fluid is set to 20 °C. Heat input applied from heating piece to evaporator section, and thus heat pipe, is controllably provided via the power supply. Orientation or inclination angle of heat pipe is arranged via the angle mechanism. Flow images are taken and transported to a computer via high speed camera and its software. Also, all temperature measurements are recorded with the support of data logger and computer.

One of the efficient ways to compare thermal performances of PHPs under different conditions is to evaluate relevant thermal resistance relative trends and magnitudes.

$$R_{th} = \frac{(T_e - T_c)}{Q} \tag{1}$$

One of the other performance criteria is the comparison of evaporator temperatures. In the present study, as stated in the above paragraphs, in the evaporator and condenser regions there are three thermocouples, and temperature of relevant regions is determined by averaging those readings. In this regard, in Equation (1), T_c and T_e represents condenser and evaporator mean temperatures. On the other hand, in the relevant equation, Q represents average value of rejected heat *(Q_r)* and input heat *(Q_i)*, as follows:

$$Q = \frac{Q_i + Q_r}{2} \tag{2}$$

$$Q_r = \dot{m} c_p (T_{wo} - T_{wi}) \tag{3}$$

where, mass flow rate and specific heat are denoted with $\dot{m}$, and c_p, respectively; while T_{wi} and T_{wo} denote inlet cooling water temperature and outlet cooling water temperature (based on heat sink).

In the present study, depending on experimental results, the uncertainty analysis is also performed by following the classical well-known approach in the literature [12]. Minimum and maximum values for uncertainty of thermal resistance are 4.1% and 5.4%, respectively. On the other hand, uncertainty value in temperature measurements is ±0.1 °C.

Results and Discussion

In the present study, non-uniform FP-CLPHPs are studied; and in the following, results obtained via the performed experiments are presented and discussed. To evaluate the role of fluid properties in the discussion of the results, before presentation of experimental results, Table 1 including fluid thermo-physical properties is presented.

Table 1: Working fluid properties (1 atm): ethanol [13] and hexane [14].

Name of Properties	Temperature (°C)	Ethanol	Hexane
Boiling point (C)	20	78.3	68.7
Liquid specific heat $kJkg^{-1}C_{-1}$	20	2.39	2.24
Liquid thermal conductivity $Wm^{-1}C^{-1}$	20	0.172	0.128
Liquid density kgm^{-3}	20	789	659
Latent heat of vaporization $kJkg^{-1}$	20	846	335
Surface tension(x10^3) Nm^{-1}	20	22.8	18.5
Liquid dynamic viscosity (x10^3)Pas	20	1.15	0.3
Saturation pressure variation with temperature(dP/dT)sat (x10^3)PaC^{-1}	80	4.23	4.27

In Figure 2, variations of the thermal resistance and evaporator temperature with heat input as a function of mixing ratio are presented. Firstly, as a general evaluation, heat input effect is discussed. Variations in thermal resistance trend give information about the operational behaviour of a PHP. Horizontal trend of thermal resistance data means that PHP cannot work; relatively significant decreasing trend means that PHP successfully operate; and slight decrements in thermal resistance data especially at relatively high heat inputs mean the PHP can only partially operate (intermittent stat-stop motions, pool boiling type operation, etc.). Also, abrupt drop in thermal resistance values means start of the PHP operation. In this regard, from Figure 2a, it is seen that start-up characteristics of E:H = 1:4 and E:H = 1:1 are significantly better against E:H = 4:1. Start-up heating power of E:H = 1:4 and E:H = 1:1 is 20 W; while this value is 30 W for E:H = 4:1. Also, magnitudes of thermal resistance data is lower for E:H = 1:4 and E:H = 1:1 compared to E:H = 4:1. This shows that circulation rate or effective heat transfer mechanisms (flow patterns, thin film evaporation, bubble nucleation, etc.) is better; and/or they more widely distribute throughout the flow passage. Details can be seen in Figure 3 representing flow images at different conditions. As comparatively seen from Figure 2 and Figure 3, at 30 W heat input, thermal resistance of E:H = 1:4 is obviously lower than the one of E:H = 4:1. For E:H = 1:4 at 30 W, nucleation effectively occurs, there are many vapour plug and they are dispersed nearly whole the heat pipe. Thin film evaporation is effective. When the heat input increases to 45W, For E:H = 1:4, bubble population significantly increases, number of vapour plugs increases and their size decreases. Micro convection and phase change phenomenon enhance. On the other hand, at 30 W, for E:H = 4:1, only some of the channels are active. In some channels, relatively long vapour bubbles occur, and they moves relatively low velocity (compared to E:H = 1:4). Depending on heat input increase, even for E:H = 4:1, most of the channels become active, number of vapour plugs increase, in other words, phase change enhances. However, flow phenomena or motion is not effective as the one in other mixing ratio. This is clearly seen from flow images.

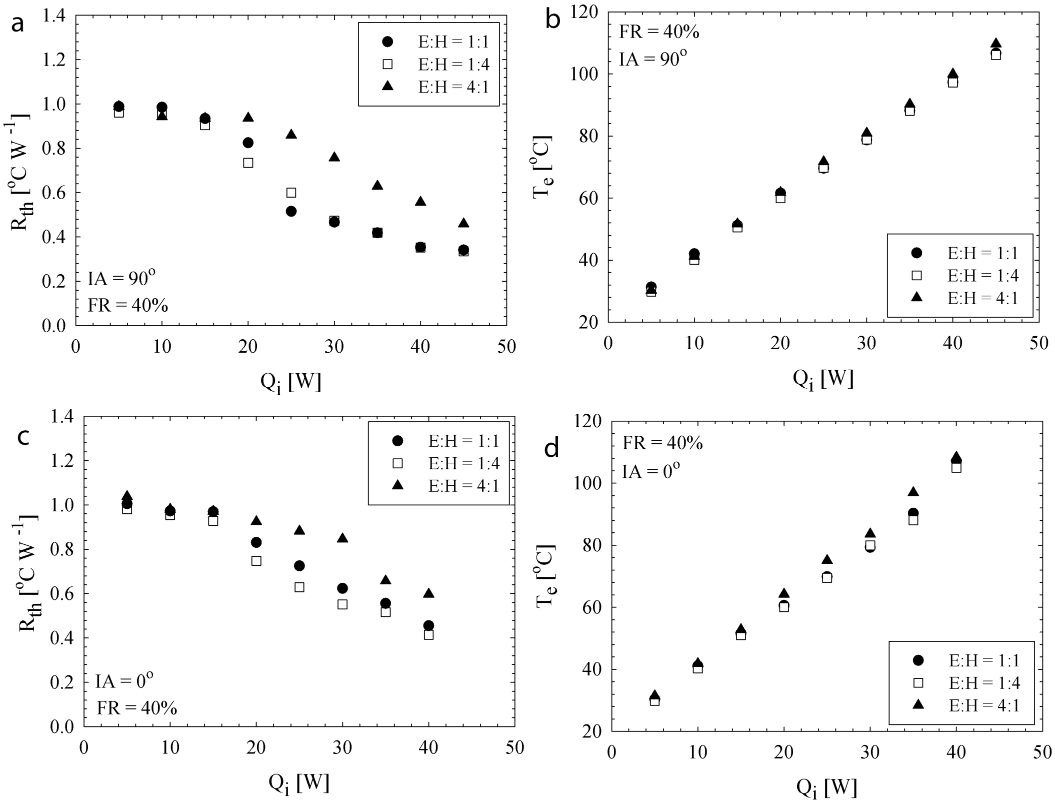

Figure 2: Thermal resistance and evaporator temperature variations with heat input as a function of mixing ratio.

On the other hand, as clearly seen from the graphs (Figure 2), mixing ratio is a very influential parameter dominating the thermal performance. Increasing ethanol volume fraction in the mixture (E:H = 4:1) significantly decreases the thermal performance. On the other hand, equal mixture (E:H = 1:1) or excess of hexane (E:H = 1:4) presents similar performance with each other; and they show clearly better thermal performance compared to the mixture of E:H = 4:1. Influential flow patterns or phenomena are clearly discussed in the previous paragraph (for Figure 3). Here, Table 1, in other words, the role of fluid properties is discussed. Actually, (dP/dT)sat is an important parameter for start-up or operation of the PHP since it represents temperature based pressure variation. However, both of the fluids have similar (dP/dT)sat value; and in spite of this, there are differences at start-up characteristics depending on mixing ratio. Thus, there should be other parameters effecting start-up performance. It is concluded that dynamic viscosity is the critical parameter. There are significant difference between dynamic viscosities of ethanol and hexane (nearly 4 times). Therefore, increasing ethanol volume fraction significantly decreases thermal performance especially at start-up conditions and/or low to medium heat inputs. It should be stated that dynamic viscosity decreases with increasing temperature; thus, the mixture having highest ethanol fraction (E:H = 4:1) starts to operate at higher heat loads, and its thermal resistance significantly decreases at relatively high heat loads. In addition to dynamic viscosity, another important property is the latent heat. In spite of higher ethanol volume of E:H = 1:1 compared to E:H = 1:4, thermal performances of these two mixture is similar. The probable reason is the higher latent heat value of ethanol. Up to some volume fraction of ethanol, this property can compensate thermal deterioration caused by high dynamic viscosity.

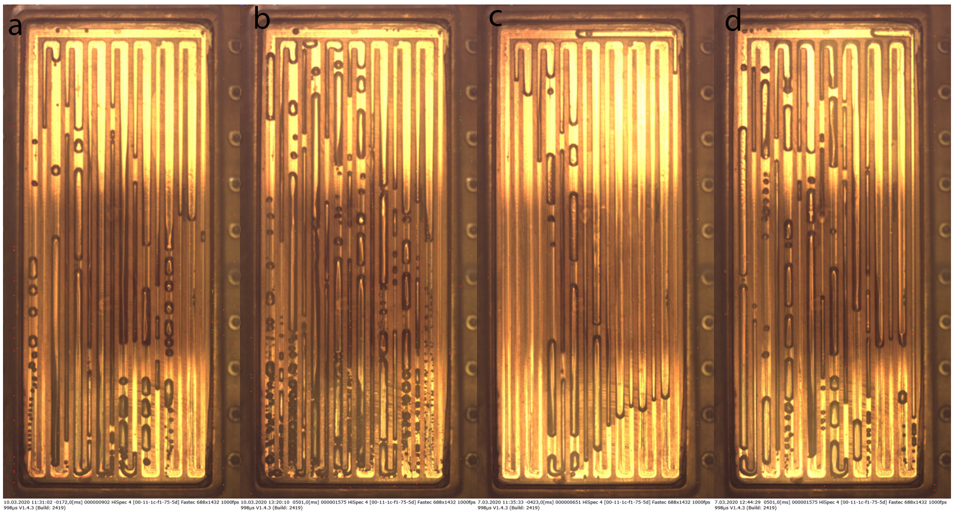

Figure 3: Flow images belong to E:H = 1:4 and E:H = 4:1 at vertical condition (90°).

Figure 2 is presented for both the horizontal and vertical conditions. However, to clearly show the effect of inclination angle, Figure 4 is presented.

As it is seen from Figure 4, PHPs charged with relevant mixtures shows nearly independent operation from inclination angle. Dependence on angle is a bit more for E:H = 1:1 compared to others. Basic probable reason is related to the non-uniform design of the consecutive channels; which increases internal perturbations. Lack of gravity support is greatly compensated by non-uniformity of capillary force (unbalanced capillary force) and imbalances caused by rapid bubble growth phenomenon occurring in narrow channels. However, gravity is still effective on the results. At vertical conditions, maximum reachable heating power values are higher for all the mixing ratios. Also, evaporator temperatures at vertical conditions are lower at last a few heating powers. Therefore, it can be concluded that thermal performance is slightly dependent on inclination angle for all the mixing ratios.

Conclusions

Detailed discussion is performed in previous section. In this part, experimental results obtained in the scope of present study are summarized as follows:

- Start-up characteristics of E:H = 1:4 and E:H = 1:1 are significantly better against E:H = 4:1. Also, magnitudes of thermal resistance data is lower for E:H = 1:4 and E:H = 1:1 compared to E:H = 4:1.

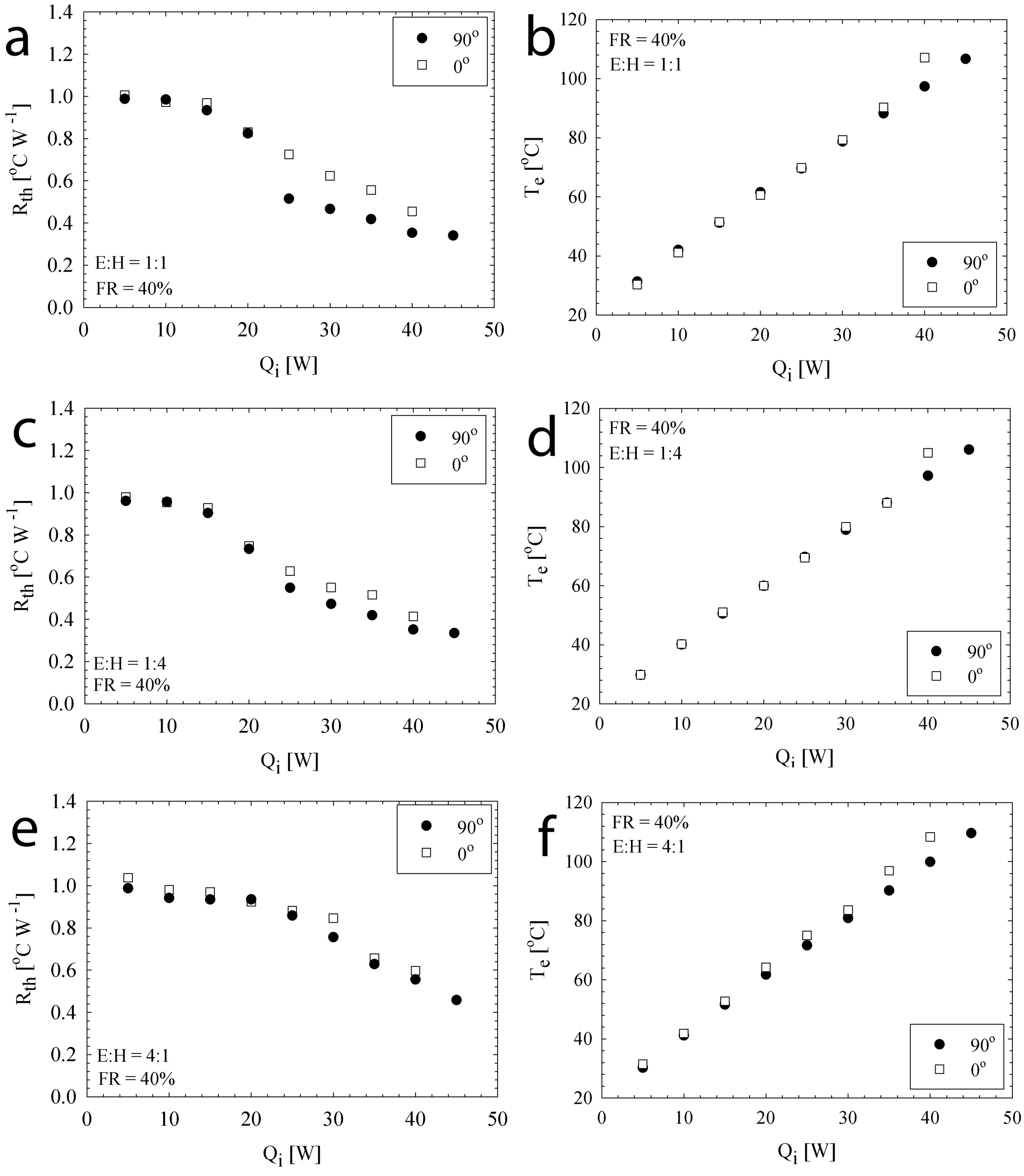

Figure 4: Effect of inclination angle.

- Increasing ethanol volume fraction in the mixture (E:H = 4:1) significantly decreases the thermal performance. On the other hand, equal mixture (E:H = 1:1) or excess of hexane (E:H = 1:4) presents similar performance with each other.
- Dynamic viscosity is the critical parameter especially at start-up conditions and/or low to medium heat inputs. On the other hand, another critical parameter is latent heat.
- Variations in thermal resistance trend give information about the operational behavior of a PHP. Horizontal trend of thermal resistance data means that PHP cannot work; relatively significant decreasing trend means that PHP successfully operate; and slight decrements in thermal resistance data especially at relatively high heat inputs mean the PHP can only partially operate.
- PHPs charged with relevant mixtures shows nearly independent operation

from inclination angle. Dependence on angle is a bit more for E:H = 1:1 compared to others. However, depending on the maximum reachable heating power and evaporator temperatures, it can be concluded that thermal performance is slightly dependent on inclination angle for all the mixing ratios. In other words, gravity is still effective on the results.

- Flow patterns, bubble dynamics and/or phase change phenomena are very important in terms of thermal performance.

Acknowledgement

The Scientific and Technological Research Council of Turkey (TUBITAK) supported this study with the project number of 217M341.

References

[1] Alhuyi Nazari, M., Ahmadi, M. H., Ghasempour, R., & Shafii, M. B. (2018). How to improve the thermal performance of pulsating heat pipes: A review on working fluid. Renewable and Sustainable Energy Reviews, 91, 630–638. `https://doi.org/10.1016/j.rser.2018.04.042`

[2] Khandekar, S., Dollinger, N., & Groll, M. (2003). Understanding operational regimes of closed loop pulsating heat pipes: an experimental study. Applied Thermal Engineering, 23(6), 707–719. `https://doi.org/10.1016/s1359-4311(02)00237-5`

[3] Qu, J., Wu, H., Cheng, P., & Wang, X. (2009). Non-linear analyses of temperature oscillations in a closed-loop pulsating heat pipe. International Journal of Heat and Mass Transfer, 52(15–16), 3481–3489. `https://doi.org/10.1016/j.ijheatmasstransfer.2009.03.012`

[4] Fumoto, K., Kawaji, M., & Kawanami, T. (2010). Study on a Pulsating Heat Pipe With Self-Rewetting Fluid. Journal of Electronic Packaging, 132(3), 031005–1. `https://doi.org/10.1115/1.4001855`

[5] Saha, M., Feroz, C. M., Ahmed, F., & Mujib, T. (2011). Thermal performance of an open loop closed end pulsating heat pipe. Heat and Mass Transfer, 48(2), 259–265. `https://doi.org/10.1007/s00231-011-0882-9`

[6] Pachghare, P. R., & Mahalle, A. M. (2013). Effect of Pure and Binary Fluids on Closed Loop Pulsating Heat Pipe Thermal Performance. Procedia Engineering, 51, 624–629. `https://doi.org/10.1016/j.proeng.2013.01.088`

[7] Han, H., Cui, X., Zhu, Y., & Sun, S. (2014). A comparative study of the behavior of working fluids and their properties on the performance of pulsating heat pipes (PHP). International Journal of Thermal Sciences, 82, 138–147. `https://doi.org/10.1016/j.ijthermalsci.2014.04.003`

[8] Yang, K.-S., Cheng, Y.-C., Liu, M.-C., & Shyu, J.-C. (2015). Micro pulsating heat pipes with alternate microchannel widths. Applied Thermal Engineering, 83, 131–138. `https://doi.org/10.1016/j.applthermaleng.2015.03.020`

[9] Cui, X., Qiu, Z., Weng, J., & Li, Z. (2016). Heat transfer performance of closed loop pulsating heat pipes with methanol-based binary mixtures. Experimental Thermal and Fluid Science, 76, 253–263. `https://doi.org/10.1016/j.expthermflusci.2016.04.005`

[10] Patel, V. M., Gaurav, & Mehta, H. B. (2017). Influence of working fluids on startup mechanism and thermal performance of a closed loop pulsating heat pipe. Applied Thermal Engineering, 110, 1568–1577. `https://doi.org/10.1016/j.applthermaleng.2016.09.017`

[11] Patel, V. M., Gaurav, & Mehta, H. B. (2017). Influence of working fluids on startup mechanism and thermal performance of a closed loop pulsating heat pipe. Applied Thermal Engineering, 110, 1568–1577. `https://doi.org/10.1016/j.applthermaleng.2016.09.017`

[12] Kline S. J., & McClintock, F. A. (1953). Describing uncertainties in single-sample experiments, Mech. Eng., 75, 3–8.

[13] Shi, S., Cui, X., Han, H., Weng, J., & Li, Z. (2016). A study of the heat transfer performance of a pulsating heat pipe with ethanol-based mixtures. Applied Thermal Engineering, 102, 1219–1227. `https://doi.org/10.1016/j.applthermaleng.2016.04.014`

[14] Thermophysical Properties of Fluid Systems. (2020). NIST Chemistry WebBook. `https://webbook.nist.gov/chemistry/fluid/`

Acridine-1,8-dione Derivative as a Chemosensor: DFT Studies

Fatemeh Mohajer[1], Ghodsi Mohammadi Ziarani[2], Alireza Badiei[3], Maryam Anafcheh[4]
[1]f.mohajer@alzhara.ac.ir, Department of Chemistry, Faculty of Physics and Chemistry, University of Alzahra, Tehran, Iran
[2]gmziarani@yahoo.com, Department of Chemistry, Faculty of Physics and Chemistry, University of Alzahra, Tehran, Iran
[3]m.anafcheh@alzhara.ac.ir, School of Chemistry, College of Science, University of Tehran, Tehran, Iran
[4]abadiei@khayam.ut.ac.ir, Department of Chemistry, Faculty of Physics and chemistry, University of Alzahra, Tehran, Iran

Abstract

Synthesized acridine-1,8-dione derivative was examined to detect Fe^{+3} ions by fluorescent. The sensor displayed high selectivity and sensitivity toward Fe^{+3} in the presence of the other ions in the solution of $EtOH/H_2O$ (1:99, v/v). The progress in fluorescence intensity was related linearly to the concentration of Fe^{+3} with a detection limit of $5.3x10^{-7}$ M. The synthesized compound had a unique blue color in the fluorescent irritation, which was highly intensive. As a result, this chemosensor afforded a different manner for selectivity of Fe^{3+} ions, among other ions. DFT results indicate that in the preferred conformer of 1,8-dione the Cl atom points out the acridine plane with $HC1C_2C_3$ dihedral angel $\theta = 2.92^{\text{º}}$. The complexes stabilize due to the donation of electron density from lone pairs of oxygen atoms or CC σ orbitals to the empty LP* of transition metals (Figure 1).

Graphical Abstract

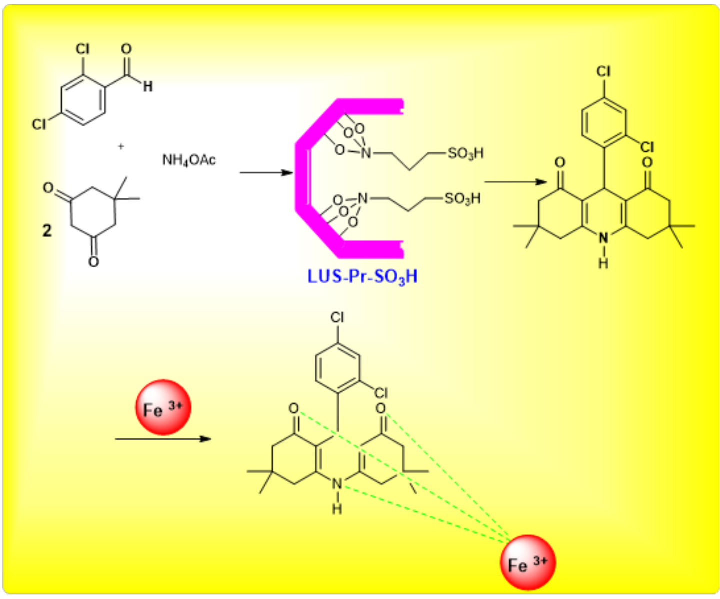

Figure 1: Scheme 1

Keywords: Fluorescent sensor, Iron ion (III), Acridine-1,8-dione derivatives, Nanocatalyst LUS-Pr-SO_3H, Computational study of DFT.

Introduction

As Iron is a highly vital element from biological perspectives, it has a crucial role in many living routes at the molecular and cellular structures such as oxygen, electron transfer, DNA synthesis, and nitrogen complex [1, 2]. Nevertheless, the reduction of iron in a human body could make several syndromes like anemia [3] diabetes, [4] Parkinson's disease, [5] and cancer [6]. Since Fe^{3+} is highly valuable for health, making sensors might be used in various applications. In this paper, we report a synthesized compound of acridine with highly a blue fluorescence response in the presence of a UV light source.

There are many techniques such as FAAS (flame atomic absorption spectroscopy) [7] and ICP-AES (inductively coupled plasma-atomic emission spectrometry) [8,9] for detection and measurement of iron ions. These methods are generally expensive, complicated, and inconvenient for the study of Fe^{3+}. Among several procedures for recognition of ions, fluorescent sensors manipulated mainly due to their easiness, and flexibility [10]. There are many sensors respond solely to Fe^{3+}, [11] and some are sensitive to Fe^{+2} [12, 13]. The current sensor is profoundly different in comparison with others as it is unique and just responded to Fe3+ without any significant interferences. Based on our literature survey, there was no report on the application of acridine as a fluorescence sensor for Fe^{3+} with very high observed selectivity in the presence of adverse ions.

The presence of two types of electron donor nitrogen atoms in chloro 1,8-dione acridine, chlorobenzene as a substituent, including a 1,4-dihydropyridine nitrogen atom and two 5,5-dimethylcyclohex-2-en-1-one oxygen atom, makes the presence acridine derivative a worthy two dentate ligand which could coordinate Fe^{3+}.

Results and Discussion

Study of the Sensing Ability of Acridine:

For the selectivity study, the fluorescence response behavior of 1,8-dione acridine + Fe^{3+} system was examined upon treatment with various metal cations including K^+, Na^+, Co^{2+}, Ni^{2+}, Ca^{2+}, Mn^{2+}, Hg^{2+}, Pb^{2+}, Fe^{3+}, Fe^{2+}, Mg^{2+}, Al^{3+}, Cr^{2+} and Cu^{3+}. None of the metal cations caused any observable disturbances in the fluorescence pattern of 1,8-dione acridine except in the presence of Fe^{3+} (Figure 2).

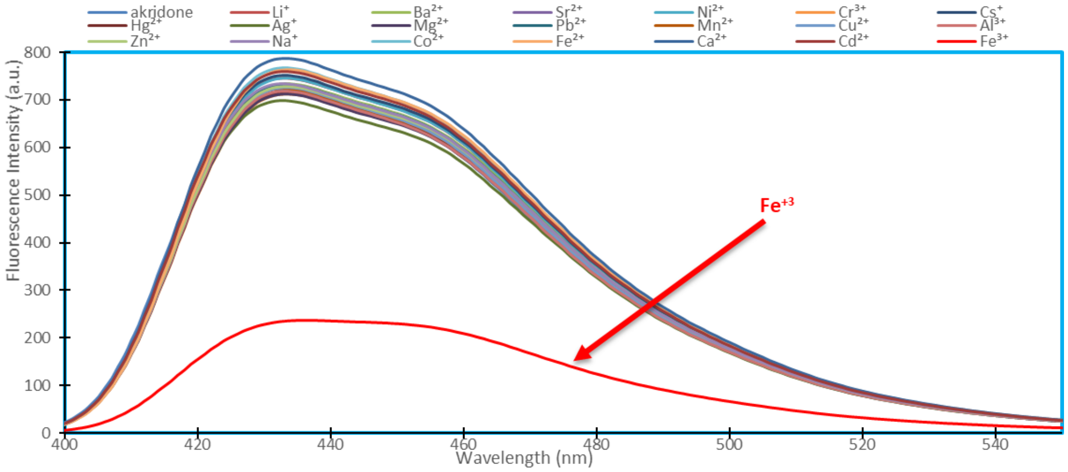

Figure 2: Fluorescence emission spectra of synthesized chemosensor in the presence of 30 equiv. of different metals including Na^+, Mg^{2+}, Al^{3+}, K^+, Ca^{2+}, Cr^{3+}, Mn^{2+}, Fe^{2+}, Fe^{3+}, Co^{2+}, Ni^{2+}, Cu^{2+}, Zn^{2+}, Cd^{2+} and Pb^{2+} in $EtOH/H_2O$ (1:99, v/v) solution, [acridine chemosensor] = 10 μM, (δ_{ex}: 431 nm).

DFT Study:

The simulated IR spectra for 1,8-dione acridine Fe^{3+} ion complex and their assignments are given in Figure 2. The simple scaling of the theoretical wavenumbers according to the equation $\nu_{Obsd} = 0.9828\ \nu_{Theor}$ generally leads to a satisfactory agreement with the set of the observed wavenumbers. It is worthwhile noting that stretching modes of the C-C bonds of hexagon-hexagon junctions and the C=O carbonyl bonds shift to the lower frequencies at 1618.5 and 1726.4 cm^{-1}, respectively, in comparison to those of pristine 1,8-dione acridine.

Summary

In conclusion, a novel chloro 1,8-dione acridine through fluorescent sensor was conclusively established, and its detection limit for a wide-ranging of metal ions was investigated. The chemosensor displayed an excellent sensing facility to Fe^{3+} ion through a considerable fluorescence quench, which was recognized to the interaction of chemosensor with Fe^{3+}. Detection limits were calculated about $5.3x10^{-7}$ M in this case; we consider that the chemosensor could be useful for the recognition of the metal cations "Fe^{3+}". Our DFT results show that the geometry of 1,8-dione acridine in which the Cl atom points out of the acridine plane with $HC1C_2C_3$ dihedral angel $\theta = 2.92^{\text{o}}$ is the preferred conformer. The stability of the complexes can be attributed to a donation of electron density from lone pairs of oxygen atoms or CC σ orbitals to the empty LP* of transition metals.

References

[1] Liu, X., & Theil, E. C. (2005). Ferritins: Dynamic Management of Biological Iron and Oxygen Chemistry. Accounts of Chemical Research, 38(3), 167–175. `https://doi.org/10.1021/ar0302336`

[2] Kustka, A., Carpenter, E. J., & Sanudo-Wilhelmy, S. A. (2002). Iron and marine nitrogen fixation: progress and future directions. Research in Microbiology, 153(5), 255–262. `https://doi.org/10.1016/s0923-2508(02)01325-6`

[3] Allen, L. H. (2000). Anemia and iron deficiency: effects on pregnancy outcome. The American Journal of Clinical Nutrition, 71(5), 1280S-1284S. `https://doi.org/10.1093/ajcn/71.5.1280s`

[4] Simcox, J. A., & McClain, D. A. (2013). Iron and Diabetes Risk. Cell Metabolism, 17(3), 329–341. `https://doi.org/10.1016/j.cmet.2013.02.007`

[5] Martin, W. R. W., Wieler, M., & Gee, M. (2008). Midbrain iron content in early Parkinson disease: A potential biomarker of disease status. Neurology, 70(Issue 16, Part 2), 1411–1417. `https://doi.org/10.1212/01.wnl.0000286384.31050.b5`

[6] Richardson, D. R., Kalinowski, D. S., Lau, S., Jansson, P. J., & Lovejoy, D. B. (2009). Cancer cell iron metabolism and the development of potent iron chelators as anti-tumour agents. Biochimica et Biophysica Acta (BBA) - General Subjects, 1790(7), 702–717. `https://doi.org/10.1016/j.bbagen.2008.04.003`

[7] Ulusoy, H. I., Gurkan, R., Aksoy, U., & Akcay, M. (2011). Development of a cloud point extraction and preconcentration method for determination of trace aluminum in mineral waters by FAAS. Microchemical Journal, 99(1), 76–81. `https://doi.org/10.1016/j.microc.2011.03.013`

[8] Sooriyaarachchi, M., & Gailer, J. (2010). Removal of Fe^{3+} and Zn^{2+} from plasma metalloproteins by iron chelating therapeutics depicted with SEC-ICP-AES. Dalton Transactions, 39(32), 7466. `https://doi.org/10.1039/c0dt00229a`

[9] Frankowski, M., Ziola-Frankowska, A., Kurzyca, I., Novotny, K., Vaculovic, T., Kanicky, V., Siepak, M., & Siepak, J. (2011). Determination of aluminium in groundwater samples by GF-AAS, ICP-AES, ICP-MS and modelling of inorganic aluminium complexes. Environmental Monitoring and Assessment, 182(1–4), 71–84. `https://doi.org/10.1007/s10661-010-1859-8`

[10] Das, S., Dutta, M., & Das, D. (2013). Fluorescent probes for selective determination of trace level Al^{3+}: recent developments and future prospects. Analytical Methods, 5(22), 6262. `https://doi.org/10.1039/c3ay40982a`

[11] Sen, S., Sarkar, S., Chattopadhyay, B., Moirangthem, A., Basu, A., Dhara, K., & Chattopadhyay, P. (2012). A ratiometric fluorescent chemosensor for iron: discrimination of Fe^{2+} and Fe^{3+} and living cell application. The Analyst, 137(14), 3335. `https://doi.org/10.1039/c2an35258c`

[12] Aydin, Z., Wei, Y., & Guo, M. (2012). A highly selective rhodamine based turn-on optical sensor for Fe^{3+}. Inorganic Chemistry Communications, 20, 93–96. `https://doi.org/10.1016/j.inoche.2012.02.025`

[13] Devaraj, S., Tsui, Y., Chiang, C.-Y., & Yen, Y.-P. (2012). A new dual functional sensor: Highly selective colorimetric chemosensor for Fe^{3+} and fluorescent sensor for Mg^{2+}. Spectrochimica Acta Part A: Molecular and Biomolecular Spectroscopy, 96, 594–599. `https://doi.org/10.1016/j.saa.2012.07.032`

The Effect of Gamma Irradiation on the Optical Properties of CdS Coated Glass/ITO Thin Films

Nasim Yousefpour Novini[1], Nader Salahshour [2]

[1] $n_$yousefpour98@sut.ac.ir, Sahand University of Technology, Faculty of Science,
Department of Physics, Tabriz, Iran
[2] salahshour.n@gmail.com, Urmia university of Technology, Faculty of Science,
Department of Physics, Urmia, Iran

Abstract

In this work cadmium sulphide (CdS) thin films deposited on the glass and ITO coated glass by chemical bath deposition (CBD) method by using cadmium chloride, thiourea, ammonia solution and sodium hydroxide. Then the effect of gamma irradiation in the range of 10-30 kGy doses on the optical properties of CdS thin films investigated. UV-Vis spectroscopy before and after gamma irradiation was studied and changes in optical properties such as absorption, transition, band gap energy, extinction coefficient in the range of 300-1100 nm were studied. The mean band gap energy for CdS coated glass and glass/ITO substrate before irradiation obtained 2.41 and 2.37 eV that is similar to typical value reported in the literature. From SEM analysis after gamma ray we seen that grain size was changed and some cracked lines was observed. Results show that gamma ray at different doses dramatically changes the optical properties..

Introduction

Cadmium Sulphide (CdS) is one of the most important semiconductors of group II-VI, with a straight and relatively wide band gap (2.42 electron volts) as an optical window along with the active semiconductor of cadmium Telluride to make a thin layer of cells. It also has important applications in optoelectronics and electronic devices r [1, 2]. The preparation thin films by CBD method are better in terms of morphology and optical transmissibility. The properties thin films of CdS prepared in different methods have been studied by many researchers [3–5]. In 2014 Faisal [6] was reported The effect of gamma radiation on the structure and optical properties CdS thin films prepared by CVD method. However, very limited work has been done to investigate the effect of gamma radiation on various properties of CdS thin films. In 2014 K. Lingeswaran and el [7], they studied the characteristics of thin films deposited by CBD method on commercial glass and glass coated with indium oxide (ITO). In 2017 Tahir [8] was reported The effect of gamma radiation on optical properties of CdS thin Films prepared by cell-gel method.

In this work, the CdS thin films deposited by CBD on the glass and ITO surface and the effect of gamma radiation at different doses on optical properties of thin films have been studied.

Experiment

It is important that substrate be clean For the obtain excellent adherence and uniform thin films. CdS Thin films were deposited on the substrates using the CBD method. All the chemical used were analytical grade and all the solutions were to be prepared in de-ionized water The bath was prepared with 0.1 mM $CdCl_2$, 0.85 mM NH_3, 0.5 mM thiourea and de-ionized water. The substrate was kept vertically in the beaker at 80°C and PH=11 for 2 hours. Then the samples are dried and exposed to gamma radiation in different doses.

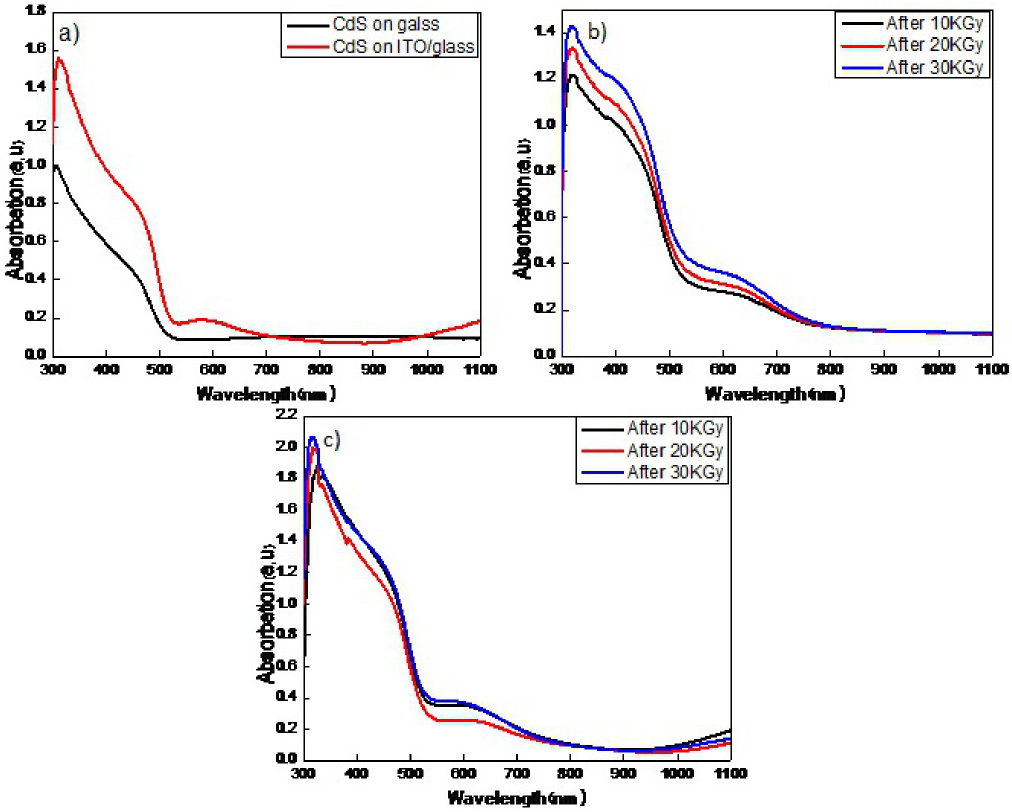

Figure 1: Absorption spectra of a) before irradiation, b) CdS on glass, c) CdS on ITO/glass after different gamma does

Results

All CdS thin films were observed uniform, smooth and adhere strongly to uniform, and well adherent on the glass and ITO coated glass substrates. Optical spectra were analysed by Perkin-Elmer lamda 45 spectrometer in the range of 300-1100 nm for different doses of gamma radiation in order to evaluate the influence of gamma ray on the thin CdS/glass and CdS/ITO/glass films absorption. Figure 1, shows the absorption spectra of the films before and after irradiation. According to that figure before gamma irradiation, difference in the absorption between the thin CdS/glass and CdS/ITO/glass films is clear and due to the presence of ITO layer, absorption was increased. Average absorption of CdS/ITO/glass films in the range of 300-1100 nm increased with the increased of gamma irradiation doses. due to the increase in grain size after gamma radiation, absorption coefficient increased.

After determining absorption coefficient and From solid state band theory, the relation between the absorption coefficient a and the energy of the incident light hv is given by Equation 1:

$$a = \frac{A(hv - E_g)^2}{hv} \tag{1}$$

where A is a constant and E_g is the band gap energy. By using the above formula and for the direct allowed transition (n = 1/2), the absorption coefficient in a function of photon energy was calculated and plotted. Intercept on the x-axis gives the value of the direct band gap. In Figure 2, before irradiation, band gap energy for CdS/glass surface is approximately 2.41 eV and for the CdS/ITO/glass is approximately 2.37 eV. Band gap energy decreases with increased in the gamma radiation doses. This is maybe due to the surface defects after irradiation [6, 9].

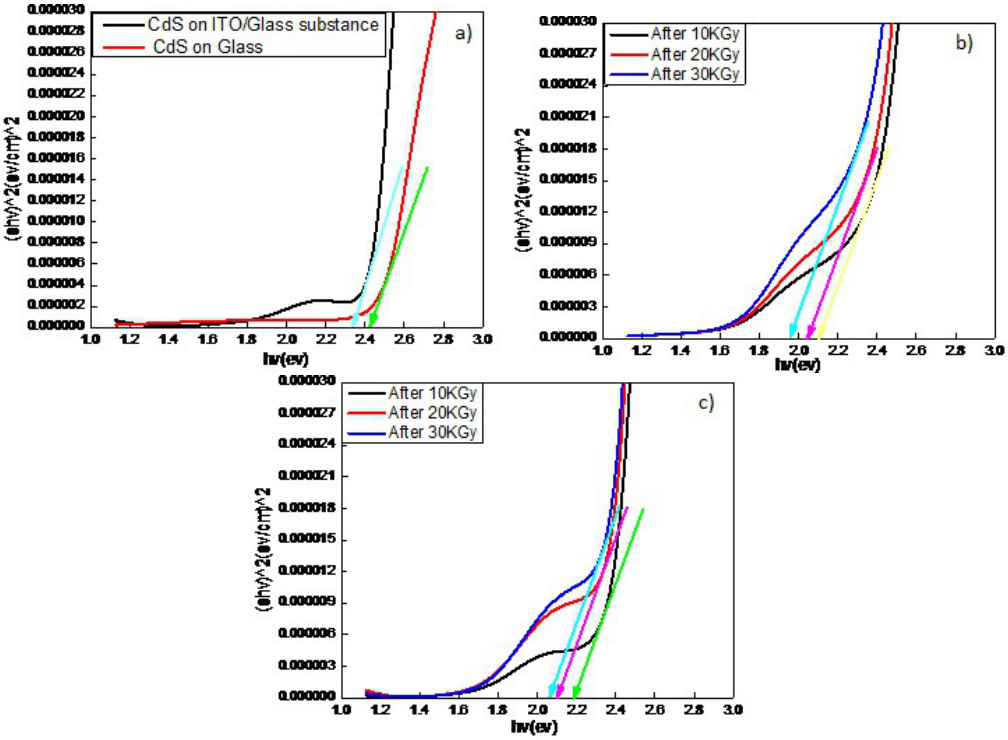

Figure 2: Band gap of a) before irradiation, b) CdS on ITO/glass, c) CdS on glass after different gamma does

extinction coefficient (k) for CdS films is given by the Equation 2:

$$K = \frac{\alpha\lambda}{4\pi} \tag{2}$$

According to Figure 3, the extinction coefficient increased with increased gamma dose, and increased due to increased absorption in the samples.

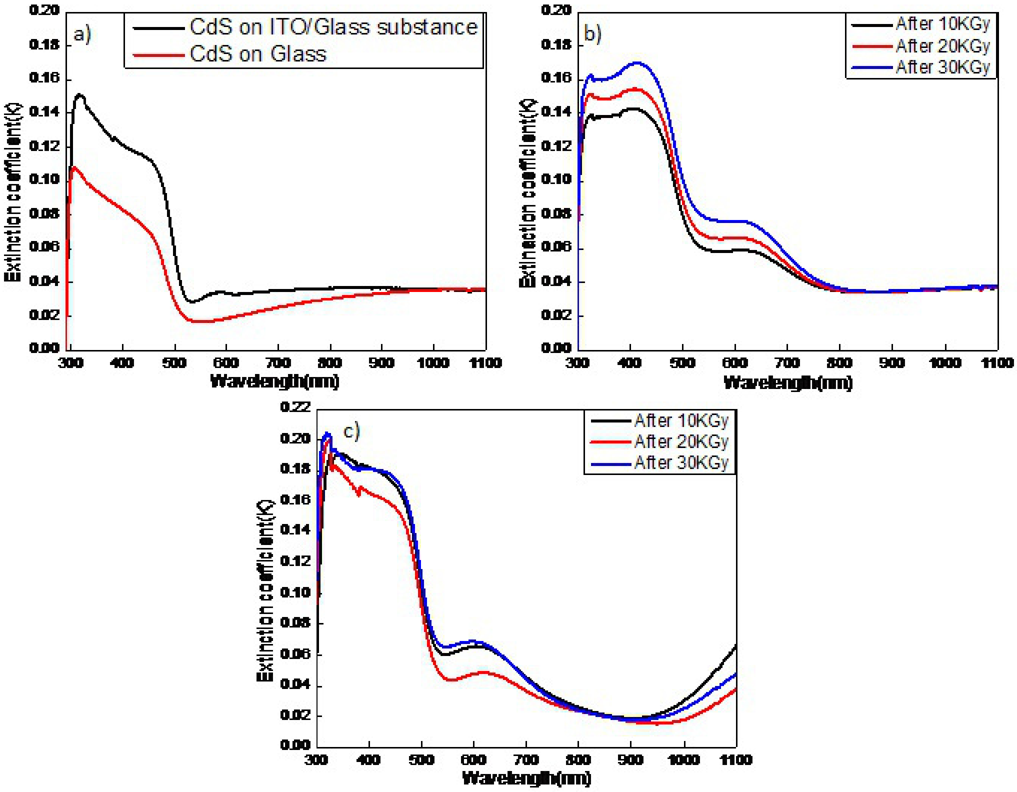

Figure 3: Extinction coefficient of a) before irradiation, b) CdS on glass, c) CdS on ITO/glass after different gamma

Figure 4, shows the X-ray diffraction patterns of CdS on glass before and after irradiation. Diffraction peaks occurring at $2\theta = 25°, 27°, 29°, 39°, 44°$ and $49°$ correspond to H(100)/H(002) and C(111)/ H(101)/ H(110) and C(220)/ H(103)/ H(112) and C(311) Miller planes respectively. All XRD results are the same for CdS / Glass and CdS / TIO / Glass. Table 1, shows the effect gamma irradiation on grain size of CdS /glass which the grain size after gamma ray increased.

Table 1: Shows the effect gamma irradiation on grain size of CdS /glass.

Before gamma	a A°	c(A°)	gain size(nm)
CdS on glass	4.105	6.644	36.11
After gamma	a A°	c(A°)	gain size(nm)
CdS on glass	4.104	6.656	36.20

Conclusion

CdS/glass and CdS /ITO/glass thin films were prepared by CBD method and the effect of different gamma irradiation does on optical were investigated. The results showed that different gamma does changed the optical properties.

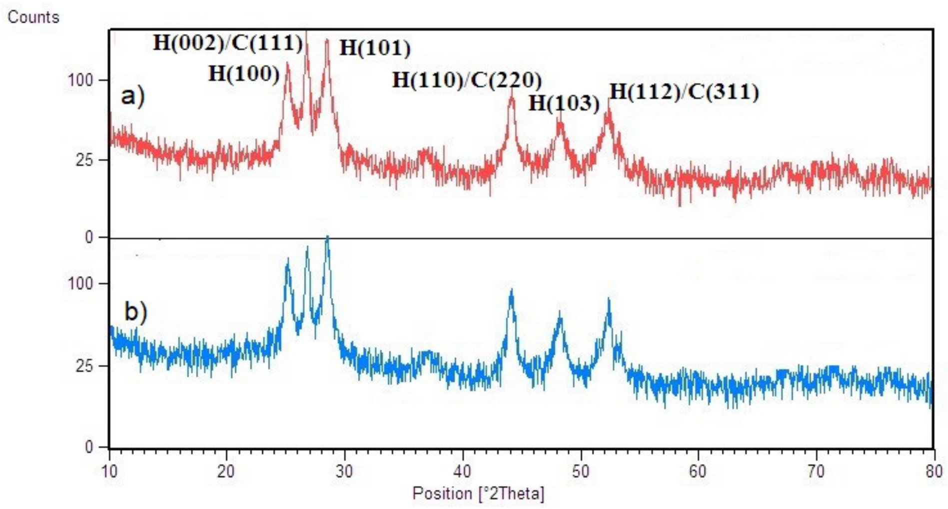

Figure 4: X-ray diffraction patterns of CdS on glass substrates a) before b) after gamma ray

References

[1] Chandramohan S., Kanjilal A., Sarangi S.N., Majumder S., Sathyamoorthy R. , Som T., "Effect of Fe-ion implantation doping on structural and optical properties of CdS thin films" Applied Physics A, 99, 837–842, 2010

[2] Britt J., Ferekides C., " Thin-film CdS/CdTe solar cell with 15.8% efficiency" Applied Physics lett, 62, 2851, 1993 `https://doi.org/10.1063/1.109629`

[3] Moreno-Regino V.D., Castaneda-de-la-Hoya F.M., Torres-Castanedo C.G. , Marquez-Marin J. , Castanedo-Perez R., Torres-Delgado G., Zelaya-Angel O., "Structural, optical, electrical and morphological properties of CdS films deposited by CBD varying the complexing agent concentration" Results in Physics, 13, 102238, 2019 `https://doi.org/10.1016/j.rinp.2019.102238`

[4] Aguilar-Hernandez J. , Contreras-Puente G., Morales-Acevedo A., Vigil-Galan O., Cruz-Gandarilla F., Vidal-Larramendi J., Escamilla-Esquivel A., Hernandez-Contreras H., Hesiquio-Garduno M., Arias-Carbajal A., "Photoluminescence and structural properties of cadmium sulphide thin films grown by different techniqes" Semiconductor Science and Technology, 18(2), 111, 2002 `DOI:10.1088/0268-1242/18/2/308`

[5] Slonopas A. , Ryan H., Foley B., Sun Z., Sun K., Globus T., Norris P., "Growth Mechanisms and Their Effect on The Opto-Electrical Properties of CdS Thin Films Prepared by Chemical Bath Deposition" Mater. Sci. Semicond. Process, 52, 24-31, 2016 `https://doi.org/10.1016/j.mssp.2016.05.011`

[6] Antar F.,"Effect of Gamma – Ray on Structural and Optical Properties of Cadimum Sulfide (Cds) Thin Films" International Journal of Application or Innovation in Engineering and Management, 3, 2014

[7] Lingeswaran K., Prasad Karamcheti S.S, Gopikrishnan M., G.Ra,"Preparation and characterization of chemical bath deposited CdS thin film for solar cell" Middle-East Journal of Scientific Research, 20, 812-814, 2014 `https://doi.org/10.4028/www.scientific.net/MSF.743-744.438`

[8] Khawla Jemeal Tahir, "Effects of gamma irradiation on optical properties of CdS thin film" Journal University of Kerbala, 15, 49-55, 2017

[9] Nefzi Ch., Souli M., Beji N., Mejri A., Kamoun N., "Enhancement by High Gamma Radiations of Optical and Electrical Properties of Indium Oxide Thin Films for Solar Devices" Journal of Materials Science, 52, 336-345, 2017 `DOI: 10.1007/s10853-016-0334-5`

Structural, Electrical and Optical Properties of Fe doped CdS Thin Films Prepared by Chemical Bath Deposition

Nasim Yousefpour Novini[1], Farzad Yousefpour Novini [2]

[1] n_yousefpour98@sut.ac.ir, Sahand University of Technology, Faculty of Science,
Department of Physics, Tabriz, Iran
[2] farzad.yousefpour@srbiau.ac.ir, Islamic Azad University, Faculty of Science and
Research Branch, Tehran, Iran

Abstract

Fe doped Cadmium sulfide (CdS) nanostructure thin films have been deposited on glass substrates successfully by the low cost and simple method of chemical bath deposition using cadmium chloride, thiourea, iron(II) chloride and ammonia. The effect of different iron concentrations on morphological, optical and electrical properties of CdS thin films have been investigated. Optical properties, including absorption coefficient, band gap, photoluminescence. UV-VIS spectrophotometric measurements as studied and the change in absorption and photoluminescence in the visible wavelength ranges (300-1100 nm) have investigated. The band-gap energy of the samples have measured in the range of 2.41-2.31 eV and according to the V-I results we observed that with increase in iron concentration, the current decreases linearly.

Introduction

Cadmium sulphide (CdS) is one of the most important Group II-VI semiconductors with a straight relatively wide band gap (2.42 eV). It has important applications in solar cells, optoelectronics and electronic devices. Recent research on CdS material and doped this material with various transition metals such as Fe, Cr, Mn and Ni, known as a dilute magnetic semiconductor [1]. Different physical and chemical methods have been proposed for the fabrication of CdS thin films. Chemical methods including spray pyrolysis, electrochemical deposition and chemical bath deposition (CBD) are more widely used. Preparation of thin films by CBD method has better properties in terms of morphology and optical absorbance and has long been considered for its simplicity and economy. The properties of CdS thin films prepared by various methods have been studied by many researchers [2–4]. In 2015, Al-Zahrani [5] investigated the effect of gamma irradiation on the optical properties of Fe-doped CdS thin film prepared by electron beam evaporation. Chandramohan et al. [1] By ion implantation, Fe doped CdS thin films and its effect on the optical and structural properties were investigated.

In this paper, Fe doped CdS thin films were prepared by the easy and low cost method of CBD and the effect of Different concentrations (0.4, 0.5 and 0.6 mM) of iron on optical such as absorption coefficient, band gap, photoluminescence in the ranges of (300-1100 nm) and electrical properties I-V have been studied.

Experiment

The substrates were dipped in 20% HCl solution for 15 minutes then cleaned in ultra-sonic bath, degreased by ethanol-acetone-ethanol and deionised water for 10 minutes, respectively. The bath was prepared with 0.1 mM $CdCl_2$, 0.85 mM NH_3, 0.4 mM $FeCl_2$, 0.5 mM thiourea and de-ionized water. The substrate was kept vertically in the beaker at 80 °C and pH=11 for 2 hours. This process was repeated for 0.5 mM and 0.6 mM iron concentrations. Thus, samples with a uniform surface and good adhesion are obtained. To make the ohmic contact, aluminum deposited on thin films by PVD method then we pasted the thin copper wires on thin films with silver glue.

Results and Discussion

Structural Characterization:

Figure 1 shows the XRD patterns of un-doped and 0.4 mM Fe doped CdS samples. In the X-ray diffraction pattern of thin films, all diffraction peaks designated with standard cards JCPDS 80-0019 for the cubic phase and JCPDS 80-0006 for the hexagonal phase. The patterns in Figure 1 clearly have diffraction peaks around 25°, 27°, 29°, 39°, 44° and 49° which, respectively, correspond to the H(100)/H(002) and C(111)/ H(101)/ H(110) and C(220)/ H(103)/ H(112) and C(311) Miller planes of thin films. The wideness of the peaks confirms that the samples are nanocrystallin. According to the Figure 1 the preferred growth is at an angle of 2θ=27°. The broadened profile of the diffraction peaks originates from the small sizes of the nanocrystals, and the Debye – Scherrer Equation 1 can be used to estimate the particle size [6]:

$$D = \frac{k\lambda}{\beta_{2\theta}\cos\theta} \tag{1}$$

Here, $\beta_{2\theta}$ is FWHM of the diffraction peak corrected for instrumental factors, λ = 1.5406 °A and k is the shape factor which takes a value of about 0.9. The shifting of the peak position is also confirms that the Fe is replaced in Cd atom position. Table 1 shows the grain size that it decreased by increased iron concentration [7].

EDS, SEM:

The EDS analysis was used to identify the constituent elements of the films. Figure 2a shows the EDS spectrum of Fe doped CdS thin film, which indicates that in addition to the elements Cd, S, Fe, the element Si is also present from glass substrate. The observed peak of Cd, Fe and S elements confirm the presence of Fe in CdS thin films. In Figure 2b,c shows the SEM Images of doped and un-doped

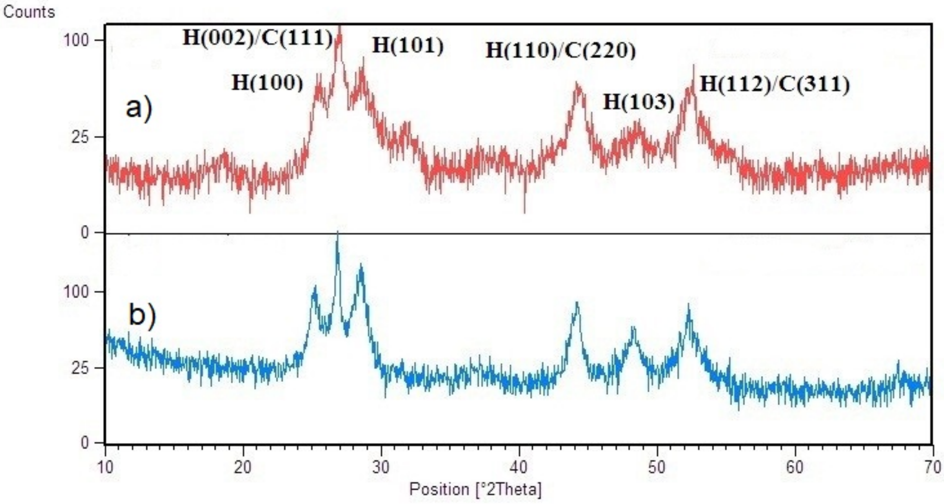

Figure 1: The XRD patterns of samples a) CdS, b) 0.4mM Fe doped CdS.

Table 1: The grain size of thin films.

sample	a A°	c(A°)	gain size(nm)
CdS	4.105	6.644	36.11
0.4mM Fe	4.090	6.654	36.08
0.5mM Fe	4.106	6.655	27.09
0.6mM Fe	4.110	6.524	21.66

CdS thin films that illustrates appropriate size distribution of Fe embedded in CdS with an average size of 38 nm, a result consistent with that obtained from XRD patterns.

Optical Study:

Optical absorption spectra is one of the important parameters in the study of optical properties of Nanostructures. It is well known that these materials show interesting size-dependent absorption. Figure 3a, shows the optical absorption spectra of thin films in the wavelength ranges 300-1100 nm. The band gap of the samples were estimated using Tauc relation [8]:

$$(\alpha hv)^2 = B(hv - E_g) \tag{2}$$

where B is a constant and E_g is the band gap energy. The values of optical absorption coefficient, α, were calculated from $\alpha = 2.303A/d$, where A and d are the absorbance value and cell thickness, respectively. Figure 4 presents the functional dependence of $(\alpha hv)^2$ versus (hv) for un-doped and Fe doped CdS which shows the band gap decreased from 2.41 to 2.31 eV with increased Fe concentration. Similar behaviour of the variation of the optical band gap with different Fe concentration has been reported by other group [9]. The decrease in the band gap with increasing of Fe concentration which is suggested to be related to the sp-d exchange interaction with the e^{2+} magnetic moment [10, 11].

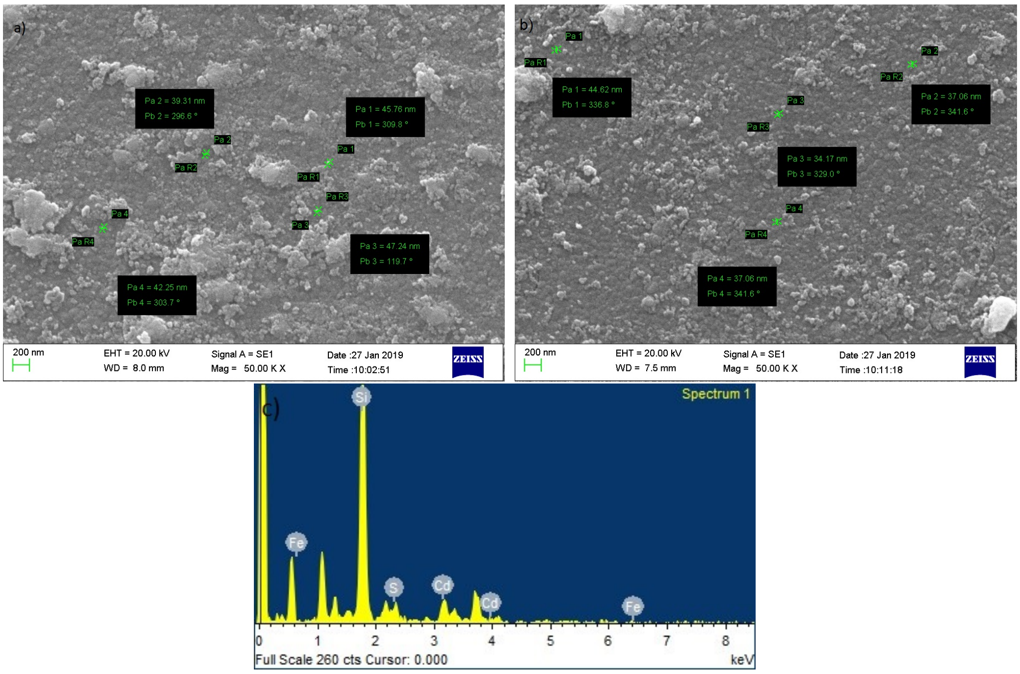

Figure 2: a) SEM Images of CdS, b) SEM Images of 0.4mM Fe doped CdS, c) EDS spectrum of 0.4mM Fe doped CdS

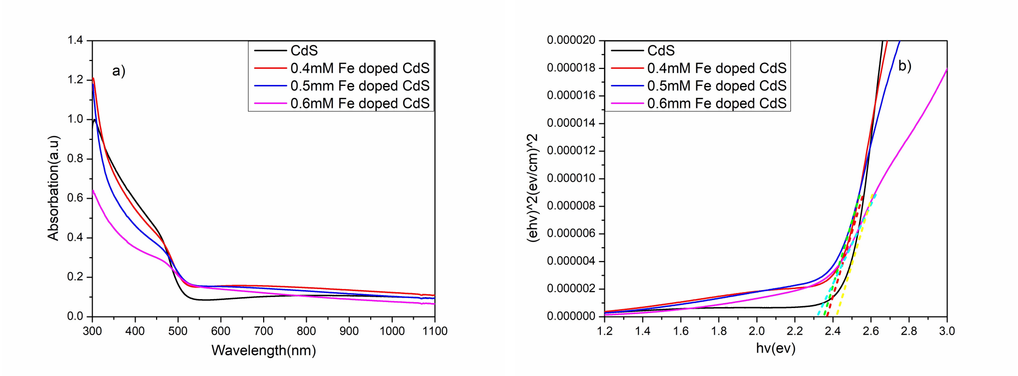

Figure 3: a) Absorption coefficient of thin films, b) band gap of thin films.

Photoluminescence is one of the most well-known types of luminescence in which Stimulation is carried out by photons. From the point of view of quantum mechanics, this process involves excitation to higher energy levels and then back to lower energy levels. Photoluminescence measurement of the Fe doped CdS was carried out with spectrofluorometer in room temperature. As we know, the excitation wavelength is very important for the Photoluminescence spectrum. For these samples, the excitation wavelength is 280 nm. Figure 5 shows the sharp emission peak at 539 nm for all thin films (un-doped and Fe doped CdS) and at 450 nm, 415 nm for Fe doped CdS. this peak is related to the green emission (GE) (with 2.3 eV energy) from CdS material that is a consequent of transition from sulphide excitations to the capacity band and acceptor-donor pair recombination and it can be attributed to radiation levels and surface defects after doped CdS

[12]. According to the result, the peak intensity increased clearly with increased concentration of iron.

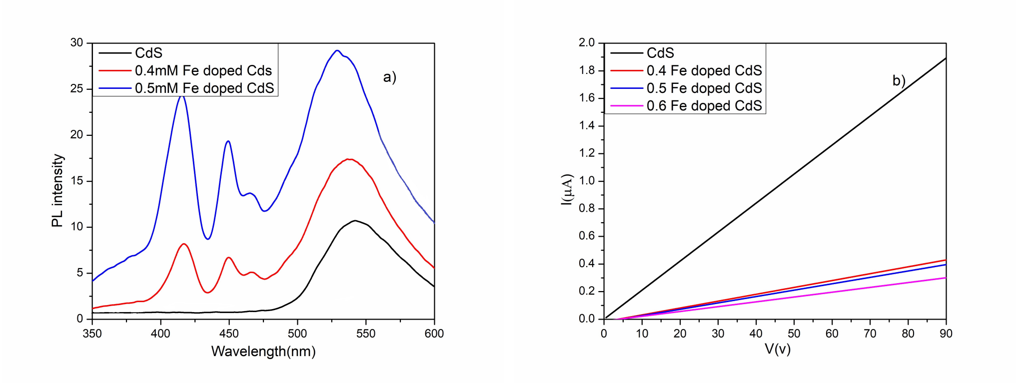

Figure 4: a)Photoluminescence of thin films, b)V-I of thin films.

Electrical Properties:

In order to measure the electrical properties we need Ohmic contacts. It was obtained by under vacuum of aluminium wire of high purity on the surface of film. Figure 6 shows the voltage curve for Fe doped CdS thin films and the pure sample. There is a linear relation between current and voltage so when voltage increased the current that cross the film increased too. by increased the iron concentration, the current increased linearly.

Conclusion

CdS and Fe doped CdS thin films were prepared by CBD method and the effect of different iron concentrations on optical and electrical properties were investigated. The results showed that different iron concentrations changed the optical and electrical properties. The grain size of Fe doped CdS films decreased with the increased Fe concentrations. The bandgap values decreased from 2.41 to 2.31 eV by increased Fe content in the CdS structure.

References

[1] Chandramohan S., Kanjilal A., Sarangi S. N., Majumder S., Sathyamoorthy R., Som T., "Effect of Fe-ion implantation doping on structural and optical properties of CdS thin films" Applied Physics A, 99(4), 837–842, 2010 `DOI: 10.1007/s00339-010-5598-z`

[2] Moreno-Regino V.D., Castaneda-de-la-Hoya F.M., Torres-Castanedo C.G., Marquez-Marin J., Castanedo-Perez R., Torres-Delgado G., Zelaya-Angel O., "Structural, optical, electrical and morphological properties of CdS films deposited by CBD varying the complexing agent concentration" Results in Physics, 13, 102238, 2019 `https://doi.org/10.1016/j.rinp.2019.102238`

[3] Aguilar-Hernandez J., Contreras-Puente G., Morales-Acevedo A., Vigil-Galan O., Cruz-Gandarilla F., Vidal-Larramendi J., Escamilla-Esquivel A., Hernandez-Contreras H., Hesiquio-Garduno M., Arias-Carbajal A., "Photoluminescence and structural properties of cadmium sulphide thin films grown by different techniques" Semiconductor Science and Technology, 18(2), 111, 2002 `DOI:10.1088/0268-1242/18/2/308`

[4] Slonopas A., Ryan H., Foley B., Sun Z., Sun K., Globus T., Norris P., "Growth mechanisms and their effects on the opto-electrical properties of CdS thin films prepared by chemical bath deposition" Materials Science in Semiconductor Processing, 52, 24-31, 2016 `https://doi.org/10.1016/j.mssp.2016.05.011`

[5] Al-Zahrani a J.H., El-Hagary b M., A.El-Taher n.,"Gamma irradiation induced effects on optical properties and single oscillator parameters of Fe-doped CdS diluted magnetic semiconductors thin films" Materials Science in Semiconductor Processing, 39, 74-78, 2015 `https://doi.org/10.1016/j.mssp.2015.04.042`

[6] Cullity B.D., "Elements of X-ray Diffraction, 2nd ed" Addison-Wesley Series in Metallurgy and Materials.1978

[7] Sanap V.B, Pawar B.H., "Growth And Characterization of Nanostructured CdS Thin Films By Chemical Bath Deposition Technique" Chalcogenide Lett. 6(9).2010

[8] Wu X.J., Shen D.Z., Zhang Z.Z., Liu K.W., Li B.H., Zhang J.Y., Lu Y.M., Zhao D.X., Yao B., Ren X.G., Fan X.W., "Characterization of $Cd_{1-x}Fe_x$S diluted magnetic semiconductors grown at near phase conversion temperature" Solid State Communctoins, 141(6) , 344-347, 2007 `https://doi.org/10.1016/j.ssc.2006.11.002`

[9] El-Hagary M., Emam-Ismail M., Shaaban E. R., Althoyaib S., "Composition, annealing and thickness dependence of structural and optical studies on $Zn_{1-x}Mn_x$S nanocrystalline semiconductor thin films" Materials Chemistry and Physics,132(2-3), 581-590, 2012 `https://doi.org/10.1016/j.matchemphys.2011.11.072`

[10] Ghosh P.k. , Ahmed S.K.F., Jana S. , Chattopadhyay K.K., "Photoluminescence and field emission properties of ZnS:Mn nanoparticles synthesized by rf-magnetron sputtering technique"Optical Materials, 29(12), 1584-1590, 2007 `https://doi.org/10.1016/j.optmat.2006.07.016`

[11] Lee J., "Raman scattering and photoluminescence analysis of B-doped CdS thin Films" Thin Solid Films, 451, 170-174, 2004 `https://doi.org/10.1016/j.tsf.2003.10.103`

[12] Priya A. S., Shameem Banu I.B., Thirumalai J., Alagar A., "Optical characterization of Mn doped CdS nanoparticles synthesized by simple chemical route " Optoelectronics And Advanced Materials – Rapid Communications, 7(3), 191-195, 2013

Examining the Distribution of Primary Energy Resources in the World and Turkey

Akide Cerci Ogmen[1], Ismail Ekmekci[2]
[1]akidecerci@gmail.com, Department of Occupational Health and Safety, Istanbul Commerce University, Istanbul, Turkey
[2]iekmekci@ticaret.edu.tr, Engineering and Design Faculty, Istanbul Commerce University, Istanbul, Turkey

Abstract

Renewable energy sectors, which determine the development levels of countries, are growing in our country by gaining serious momentum as in the whole world. Renewable energy sources are the second most preferred energy sources of many countries in the world and contribute to global electricity. In this study, the change in the total energy supply in Turkey and in the world will be compared. According to the development of primary energy sources installed capacity in the world and Turkey will be examined. As in developing countries, in Turkey also widely used in coal and bio fuels are the largest source of energy by far. The second largest resource is hydroelectricity. Liquid biofuels constitute the rest of wind energy, geothermal, solar and tidal renewable energy sources. The world's fuel supply shares are 26.9% coal, 31.5% oil, 22.8% natural gas, 4.9% nuclear, 0.3% other energy and 13.5% renewable energy sources, respectively. Turkey's share in the energy supply of respectively 21.49% coal, 6.3% petroleum, natural gas 24.26%, 23.19% hydroelectric, renewable energy sources in the form of 24.57%.Renewable energy sources in the world and Turkey has so different in themselves. 18.8% hydroelectricity, 5.7% wind, 4.4% solar energy, 4.8% geothermal, 66.4% biofuels constitute the percentages of renewable energy sources in the world. Referring to Turkey distribution of renewable energy sources, biomass 0.70%, wind 57.91%, solar 5.72%, 23.19% hydropower, lakes and rivers 8.76%, 1.45% is shown as geothermal energy.

Keywords: Energy Sources, Renewable Energy Sources, Distribution of Renewable Energy Sources, Installed Capacity.

Introduction

Today, the energy for which dearly-won are fought and causes the deaths of many people is of great importance to all humanity. In a geography where energy is not available; It is impossible to talk about production, consumption, economy and of course human life [2]. The fact that the production and use of energy is in line with social benefit is an indicator of economic and social development [9]. At the same time, the economic, cultural and scientific levels of countries are measured by the amount of energy they produce and use. In short, energy is a locomotive of economic development [1].

Energy sources are very important in terms of economy and social development. After the Industrial Revolution, demand of people for energy resources increases and this increase continues today [11]. When the literature is reviewed, it is seen that there are a number of different distinctions regarding energy. Energy has been categorized as ”renewable” and ”non-renewable” energy types. According to another distinction; It is possible to examine energy in two different parts as primary and secondary energy sources [2]. Primary energy sources are the forms of energy that have not undergone any change or transformation. Primary energy sources are oil, coal, natural gas, nuclear, hydraulic, biomass, tidal wave, solar and wind [8].

Energy Situation in Turkey and the World

Major Energy Sources and Production and Consumption Rates by Country:

Oil: Today, oil is the source that causes the most violence among energy resources. To be able to see how the struggle for oil will get tough and some statistical data will be a guide to understand the global demand trends of oil [7].

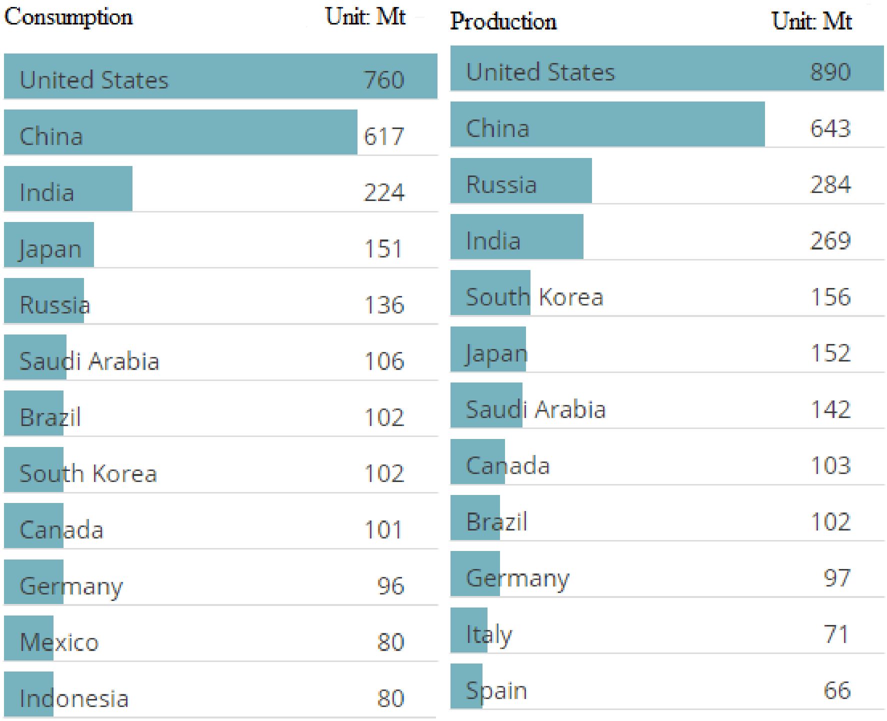

Figure 1: Oil products domestic consumption and production [4].

As seen in Figure 1, the global oil product consumption, oil product consumption decreased in the USA, the largest consumer worldwide, due to a lower demand from industry and the petrochemical sector (delays in projects), and to diminishing car sales to a lesser extent. It also declined in Japan in Latin America as well as in the Middle East and Africa, due to rising fuel prices. The Middle East experienced a powerful drop in line with the reduced crude oil production, with a falling output in Saudi Arabia and Iran. The declining trend continued in the EU, especially in France (due to refinery strikes) and Sweden, as refineries were shut down due to increased competition. Production increased in China due to substantial growth in refining capacity, while production stabilized in India [4].

Natural Gas:

Natural gas has been a popular energy source due to increases awareness of clean environment in people. These situations have made natural gas a popular resource as it is both an alternative and a clean fuel for the environment [7].

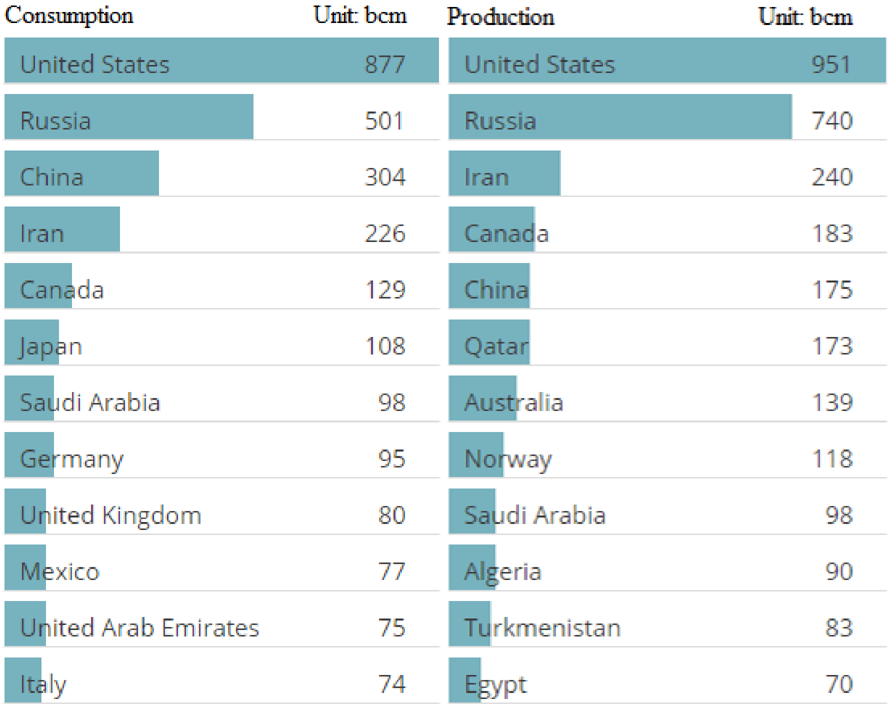

Figure 2: Natural gas domestic consumption and production [5].

When the natural gas internal consumption and production values are examined in Figure 2, in the USA, the largest gas consumer, it grew in 2019, thanks to lower prices and new gas-fired capacity in the power sector. In China, the economic slowdown and the relaxation of policy on coal-to-gas switching contributed to reduce by half the growth in gas consumption. Consumption grew in the EU, as demand recovered in Spain, Italy and Germany, and in producing countries such as Russia, Australia, Egypt, Iran and Algeria.The USA, the largest gas producer, accounted for over half of the 2019 global increase, followed by Russia, Australia, Iran and China. Gas production also continued to increase steadily in Australia and in Russia, pushed by the development of LNG projects and by domestic demand. Gas production continues decreasing in Europe, as maintenance and interruption reduced output in Norway [5].

Coal, Lignite:

Having an important place in human life and energy raw materials, coal has wide reserves and indispensable common consumption areas in the world. Coal is the first in the world electricity generation is ranked. As it is known, the most negative aspect of coal is the damage it causes to the environment [7].

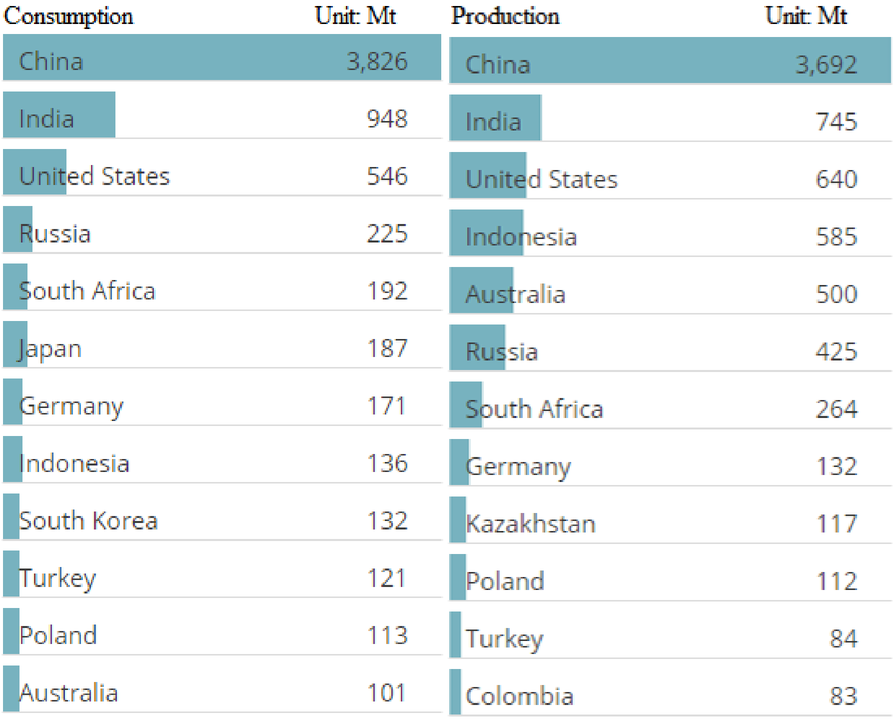

Figure 3: Coal and lignite domestic consumption and production [6].

Examining Figure 3, coal consumption increased in China, which accounts for half of the global coal demand. In India, the second largest coal consumer worldwide, coal consumption diminished, owing to higher hydropower and renewable generation that decreasing coal needs in the power sector. Coal consumption slowed down in Indonesia, and decreased in South Korea and Japan, due to a lower demand from the power sector. It also slowed down in large coal producing countries such as South Africa, Russia [6].

Renewable energy resources and their shares by country

Hydropower and Geothermal:

Hydroelectric energy is a type of energy provided by converting the potential energy of water into kinetic energy [7]. The most common use of this energy is to accumulate water in reservoirs by building dams on rivers, and to generate electrical energy in the turbine by utilizing the potential energy of the accumulated water [8].Geothermal energy is briefly the natural heat of the earth and it is defined as the thermal energy contained in the hot fluid (water, steam, gas) under pressure and hot dry rocks accumulated in the depths of the earth's crust [7]. This energy is used for electrical energy generation or heating [8].

Looking at Figure 4 [10], the global hydroelectric capacity of the world, China

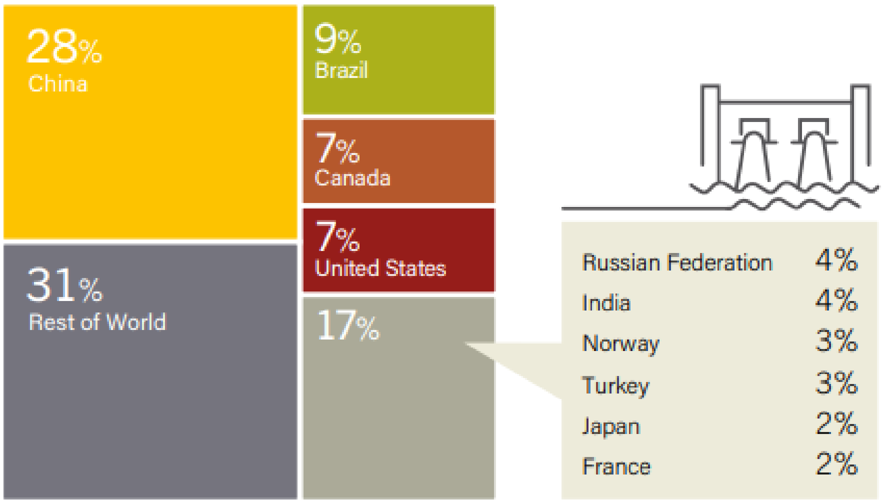

Figure 4: Hydropower global capacity, shares of top 10 countries in World, 2019.

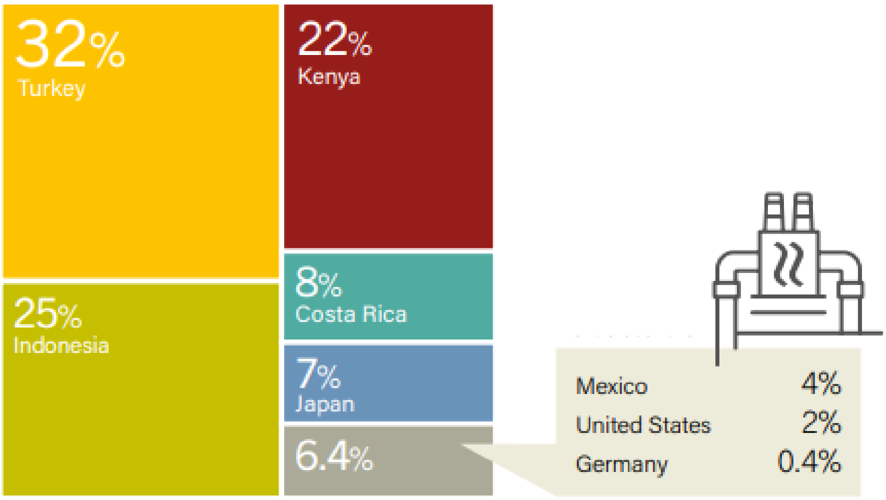

Figure 5: Geothermal power capacity and shares by country, 2019.

has the highest installed capacity in the world with 28%. Brazil, Canada and the United States have 9%, 7% and 7% installed power, respectively.

According to the Figure 5, countries which have benefited most from geothermal energy in the world, respectively, Turkey, Indonesia, Kenya, Costa Rica and Japan [10].

Solar, Wind and Biomass:

The world's most important energy source is the sun. Technologies such as solar collectors, solar power plants and solar cells (photovoltaic) have been developed to take advantage of this energy that comes to the world through solar rays. Thanks to these technologies, solar energy can be used as heat energy directly or indirectly by converting it into electrical energy [8]. Wind energy is used to generate mechanical energy or electrical energy. Wind Power Plants are used to generate electrical energy from wind energy [8]. Biomass is a mass of non-fossil organic matter of biological origin [7]. In recent years, the world has focused on renewable energy crops agriculture [8].

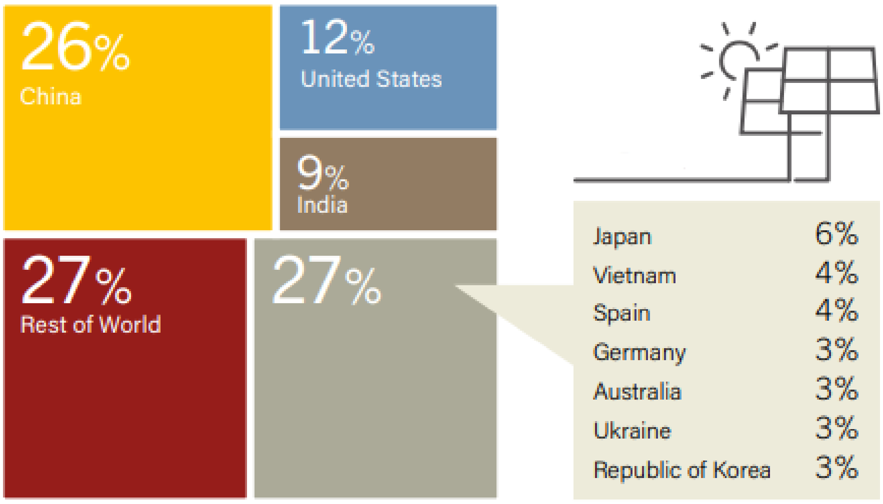

Figure 6: Solar PV global capacity and shares by country, 2019.

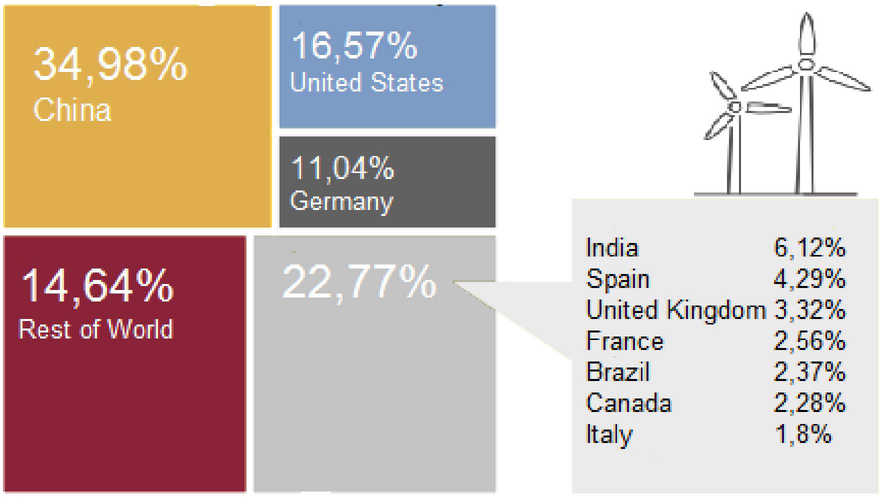

Figure 7: Wind global capacity and shares by country, 2019.

Countries with solar energy potential are shown in the Figure 6 [10]. The country with the highest capacity is seen as China with 26%. China is followed by the United States and India. Turkey has increased its installed capacity of solar energy and has managed to be among the 49 countries in the world. It ranks 13th among 49 countries [3]. Looking at the countries that produce electricity from wind energy, it is seen that the production is mostly in China (Figure 7), [10]. Turkey is situated in the rate of 14.64%. Producing electricity from wind energy also has its own substantial value in Turkey. The evaluation of the countries using biomass energy was made in 15 countries and the remaining 28 European countries. When the results are evaluated, it is seen that the country with the highest biomass energy capacity is the USA [10].

Conclusions

In this study, what is the primary energy sources in the world and in Turkey were evaluated. The consumption of renewable energy resources, which has been increasingly used in recent years and is thought to replace non-renewable energy sources in the future, has been examined. The results obtained from the conducted study are as follows. Using the data of 2019, the usage and production percentages of non-renewable energy resources are given by country. 86.4% of the energy consumed in the world is provided by non-renewable energy sources. When the amount of primary energy consumption by 2019 in Turkey is evaluated; It is observed that a large part of the total consumption is met by non-renewable energy sources. This ratio is 52,05%. The most widely used renewable energy source in Turkey is 23.19% from hydraulic energy. Turkey and the world demand for renewable energy sources is increasing rapidly every year. According to data for 2019, especially Turkey's geothermal and wind energy power plants capacity is increasing rapidly. Existing projects should be completed rapidly and energy transmission infrastructure should be strengthened in order to benefit more from the renewable energy potential of the countries.

References

[1] Atilgan, I. (2000). Türkiye'nin Enerji Potansiyeline Bakis. J. Fac. Eng. Arch. Gazi Univ., 15(1), 31–47. `https://dergipark.org.tr/en/download/article-file/76406`

[2] Bahar, O. (2005). Türkiye'de Enerji Sektoru Uzerine Bir Degerlendirme . Mugla Universitesi Sosyal Bilimler Enstitusu Dergisi , (14) , 35-59 . Retrieved from `https://dergipark.org.tr/tr/pub/musbed/issue/23490/250178`

[3] Ulkelere Gore Ruzgar Enerjisi. (2020). Enerji Atlasi. `https://www.enerjiatlasi.com/ulkelere-gore-ruzgar-enerjisi.html` Last Access: 18.09.2020

[4] Oil consumption by region — Oil energy consumption statistics — Enerdata. (2020). Global Energy Statistical Yearbook. `https://yearbook.enerdata.net/oil-products/world-oil-domestic-consumption-statistics.html`. Refined Oil Products Production — World Refined Oil Statistics — Enerdata. (2020). Global Energy Statistical Yearbook. `https://yearbook.enerdata.net/oil-products/world-refined-production-statistics.html` Last Access: 18.09.2020

[5] Natural Gas Consumption Statistics — Natural Gas Data — Enerdata. (2020). Global Energy Statistical Yearbook. `https://yearbook.enerdata.net/natural-gas/gas-consumption-data.html`. Global Natural Gas Production — World gas natural statistics — Enerdata. (2020). Global En-

ergy Statistical Yearbook. `https://yearbook.enerdata.net/natural-gas/world-natural-gas-production-statistics.html`

[6] Consumption of Coal and lignite — World Coal consumption — Enerdata. (2020). Global Energy Statistical Yearbook. `https://yearbook.enerdata.net/coal-lignite/coal-world-consumption-data.html`. Coal and lignite Production Data — World Coal Production — Enerdata. (2020). Global Energy Statistical Yearbook. `https://yearbook.enerdata.net/coal-lignite/coal-production-data.html` Last Access: 18.09.2020

[7] Karabulut, B. (2016). Enerji Guvenligine Kuresel Olcekte Bir Bakis. The Journal of Defense Sciences, 15(1), 31–54.

[8] Koc, E , Kaya, K . (2015). Enerji Kaynaklari - Yenilenebilir Enerji Durumu. Mühendis ve Makina, 56 (668), 36-47. Retrieved from: `https://www.mmo.org.tr/sites/default/files/b0218b112f2e18b_ek.pdf`. Last Access: 18.09.2020

[9] MMO. (2012). Türkiye'nin Enerji Gorunumu. Yayin No: MMO/588, TMMOB Makine Muhendisleri Odasi, `http://www1.mmo.org.tr/resimler/dosya_ekler/dd924b618b4d692_ek.pdf`. Last Access: 18.09.2020

[10] REN21. (2020). Renewables 2020 Global Status Report. `https://www.ren21.net/wp-content/uploads/2019/05/gsr_2020_full_report_en.pdf`. Last Access: 18.09.2020

[11] Yilmaz, M. (2012). Turkiye'nin Enerji Potansiyeli ve Yenilenebilir Enerji Kaynaklarinin Elektrik Enerjisi Uretimi Acisindan Onemi. Ankara Universitesi Cevrebilimleri Dergisi, 4(2), 33–54. `https://doi.org/10.1501/csaum_0000000064`

Performance Comparison of Pitch Angle Controllers for 2 MW Wind Turbine

Ahmet Selim Pehlivan[1], Kemalettin Erbatur[2]

[1]spehlivan@sabanciuniv.edu, Department of Mechatronics Engineering, Sabanci University, Istanbul, Turkey
[2]erbatur@sabanciuniv.edu, Department of Mechatronics Engineering, Sabanci University, Istanbul, Turkey

Abstract

As wind energy is becoming more and more significant for renewable energy, effectiveness of pitch angle controller plays crucial role to achieve higher performance and optimized turbine designs. Aerodynamic performance of wind turbine rotor and consecutively electrical power production of turbine depend on the efficiency of pitch controller design. This work presents the effects of two different pitch angle controllers on a 2 MW DFIG type wind turbine under Matlab Simulink environment. The main objective of the pitch controller is to regulate the rotor and generator speed as the input of the controller was generator speed where the output of the controller is to determine the pitch angle. PI and PID control methodologies are used to design pitch controller of the turbine. Through the controller design, iterations, settling time, overshoot value, error values and power output values are decided for comparison parameters. Both controller performances in terms of transient and steady state are evaluated.

Keywords: Wind Energy, Pitch Angle Controller, Speed Regulation, Power Output.

Introduction

Wind turbine (WT) systems with large power scales, blade pitches have to be controlled in order to prevent excessive amount of energy, over speed of a rotor and not to damage the system over nominal wind speeds [1]. This reasoning can be stated as the variable speed WTs provide an opportunity to generate more energy than fixed speed wind turbines [2].

On the other hand, the output power of the variable speed WTs varies due to the uncertainties of the wind speeds. The fluctuations of the wind speeds leads to changes of the voltage and the frequency. However, fixed voltage and a fixed frequency are two of the most important criteria for a quality of electrical energy. In order to improve quality of the output power, appropriate control methods gave to be applied on wind turbine systems [3].

The variable-speed, variable-pitch wind turbine systems typically have two operating regions according to the wind speed. In partial-load region where the wind speed is lower than the rated wind speed v_{rated}, the turbine speed is controlled at the optimal value so that the maximum energy is extracted from the wind turbine [4, 5]. In the full load region where the wind speed exceeds its rated value, the generator output power is limited at the rated value by controlling the pitch angle are limited [6, 7].

One of the most important problems of horizontal axis large-scale wind turbines is that to maximize the power efficiency below the nominal wind speed and limit the nominal power above the nominal wind speeds [8]. In order to resolve this problem, variable speed variable pitch angle wind turbines can have different torque controller to maximize the power efficiency and pitch controllers to limit the nominal power [9, 10].

Pitch control is one of the most significant subsystem of a modern wind turbine and different control techniques have been applied so far to achieve more efficient wind turbines. Even though many research groups have used many control theories, classical PID controllers are frequently used in today's modern wind turbines commercially. PID controllers have been used in a great deal of wind turbine control applications because of their simple structures, high safety and robustness [11, 12]. Therefore, PID controllers have been employed in order to control system outputs of particular systems that have mathematical models [13, 14].

In this paper, conventional PI and PID controllers were applied to regulate a 2 MW DFIG type variable speed wind turbine in Matlab Simulink environment. The main aim of the both controllers is to limit the turbine output power and the generator speed in the full load region. Performance comparison criteria for both controllers are rise time, overshoot, settling time for transient dynamics whereas the error in speed and expected power are for steady state operation. In addition, energy production difference can be taken into account as comparison criterion. The comparative simulation results for a 2-MW doubly fed induction generator (DFIG) wind turbine system for both controllers shown for a certain wind speed profile.

Methodology

Wind turbine modelling and system definition. Wind turbines consists of several subsystems, which can be stated as aerodynamic, mechanical, electromechanical and electrical subsystems. In addition, control systems are also designed separately for all of the subsystem above however, torque control and pitch controllers can be considered as the most significant ones among the others [8].

As illustrated in Figure 1, wind turbines may have a different subsystem from different engineering disciplines where many of them require different controllers. Torque controllers are generally used for DFIG type generators to regulate the powers where pitch controllers are used to regulate the speed of the rotor. In addition, another highly important concept for wind turbine technologies is to classify

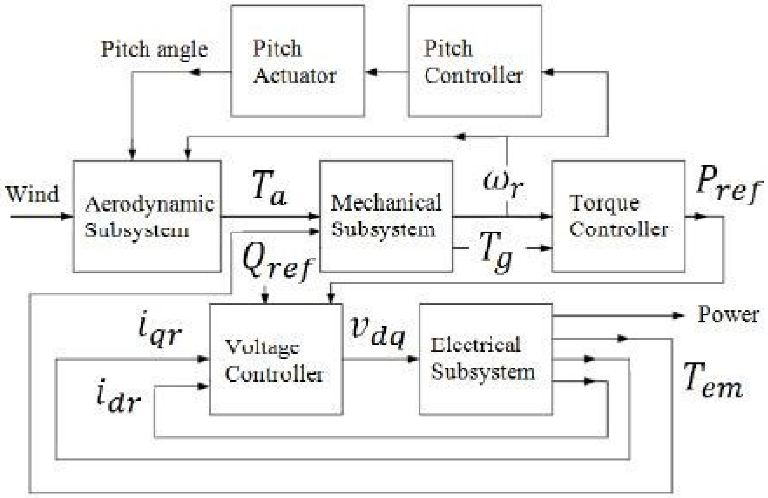

Figure 1: Wind turbine block diagram.

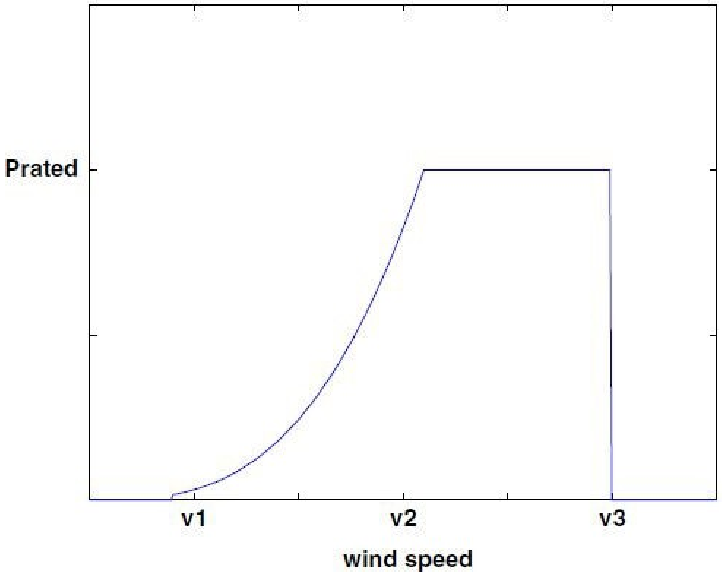

Figure 2: Wind speed regions.

operating regions since many important descriptions for the turbine are made by the wind regime graphs such as operating speed, determination of maximum power production, maximum available aeromechanical power and so on. Figure 2 shows the operating regions of the 2 MW wind turbine that is used to complete this study. As can be seen from the figure, wind profile is divided in three zone according to wind speed in which zone 1, zone 2, zone 3 can be named as cut in, rated and active and cut off respectively. Wind turbines generally starts to produce electricity with the wind speed of cut in. Until the rated wind speed, pitch system operates as Maximum Power Point Tracking (MPPT) mode with 0 degrees of pitch. While the wind speed increases, pitch system keeps maximizing the power output from the available aeromechanical power. Zone 2 is generally considered as partial load region where pitch system may start to become active to have more efficient power output performance. If the wind speed is more than rated speed, than pitch system becomes active while the wind speed increases, rotation and power is limited with higher pitch angles. Zone 3 can be considered as active pitch region above rated wind speed where the power is regulated by active pitching. After wind speed exceeds or gets near to cut off speed wind turbines are stopped due to mechanical safety reason by using pitch control [15].

Modelling of aerodynamic, mechanical, electromechanical, grid side converters on a simulation environment is a significant issue to conduct a better study for performance comparison. Throughout the study, 2 MW DFIG type variable speed and variable pitch wind turbine is under Matlab/Simulink environment used with a wind regime that is above rated speed. The aim of this certain wind regime is to observe the effect of pitching under abrupt changes of wind speed and the power regulation characteristics. Table 1 depicts the parameters for the wind turbine simulated throughout the controller design study.

Table 1: Wind turbine system parameters.

Nominal output power	2 MW	Nominal rotor speed	15.8 rpm
Working mode	Grid connection	Gear box rate	1:94.7
Cut in wind speed	3 m/s	Generator pole pair	2
Nominal wind speed	12 m/s	Generator type	DFIG
Cut out wind speed	25 m/s	Generator synchronous speed	1500 rpm
Rotor diameter	82.6 m	Generator voltage	690 V
Rotor swept area	5359		

Pitch Control Subsystem. One of the most important subsystems of a wind turbine can be pitch control since it affects the mechanical strength, aeromechanical power, rotation dynamics and consecutively electrical power regulation. Pitch controllers are actively used in the full load-operating region in order to prevent any kind of mechanical damage from the excessive loading at high wind speeds. Moreover, in order to regulate the power with the aid of speed regulation, different pitch controlling techniques are used in the modern commercial wind turbines. Throughout this study, PI and PID controllers are implemented and simulated for 2 MW DFIG wind turbine as mentioned above. Pitch controller uses the rotor angular speed as an input and error is regulated with the PID controller. In this study, normalized error is calculated and applied to controller as per unit (p.u).

Classical PID controller. In conventional control methods, PID controllers have feedback structures. After an error is passed through proportional, integral and derivative actions, the error is applied again to the system input in accordance with and the system output is controlled as desired [2]. Clarification of the continuous equation of the PID controller is as in Equation 1. Where u(t) is the controlled output , K_p is the proportional gain , K_i is the integral gain , K_d is the derivative gain and e(t) is also the error signal between the system output and the system input value [2]. Discrete version of the PID controller can be stated as follows in Equation 2.

$$u(t) = K_p e(t) + K_i \int_0^t e(t)dt + K_d \frac{de(t)}{dt} \quad (1)$$

$$\Delta u(k) = K_p[e(k) - e(k-1)] + K_i T_s e(k) + \frac{K_d}{T_s}[e(k) - 2e(k-1) + e(k-2)] \quad (2)$$

Results and Discussion

As mentioned previously, PI and PID controllers for a 2 MW DFIG type wind turbine are implemented for a certain wind regime which has a mean value of 17 m/s. Transient and steady state dynamics with the arguments of overshoot, rise time, settling time, steady state error and power productions are compared.

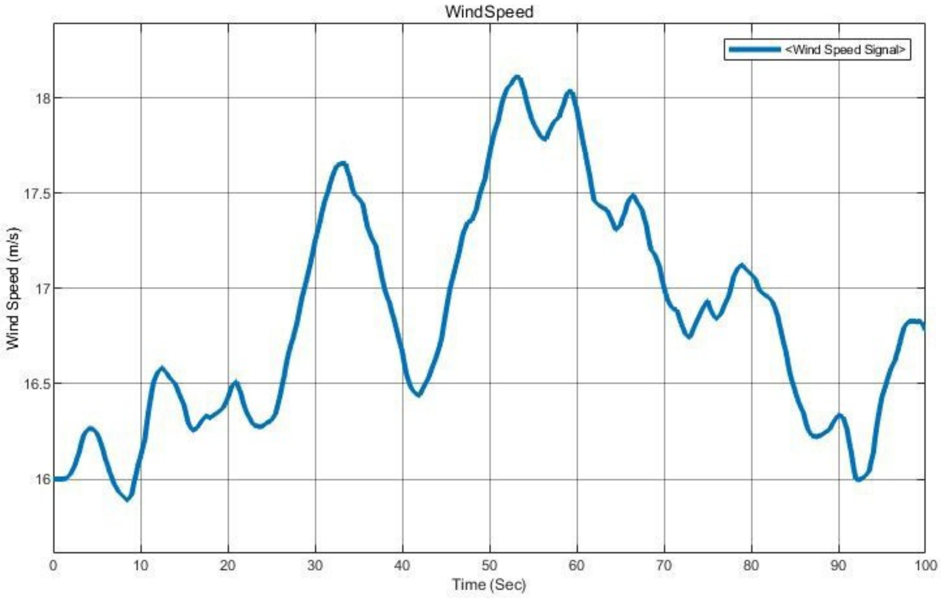

Figure 3: Applied wind speed.

As illustrated in Figure 3, wind speed input is designed for 100 seconds of simulations to observe the turbine outputs including pitch angle, power output, and C_p values to compare performances of the implemented PI and PID controllers. Wind speed has abrupt increases to observe the response of the controllers.

Under the depicted wind profile several simulations conducted to compare performances of both PI and PID controllers for transient and steady state situations. As Figure 4 and 5 show, the main aim of the controller is to maximize the power output by keeping the generator rotational speed steady at 220 rad/sec. As previously mentioned, pitch controllers aim to regulate the rotational speed of the turbine and consecutively regulate the power while full load wind regions.

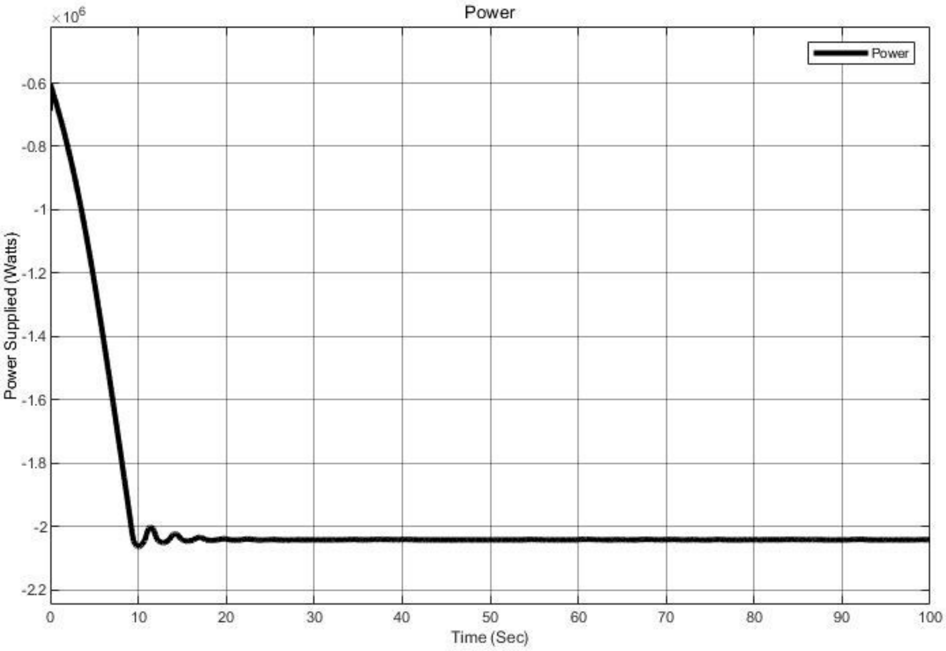

Figure 4: Power output of turbine.

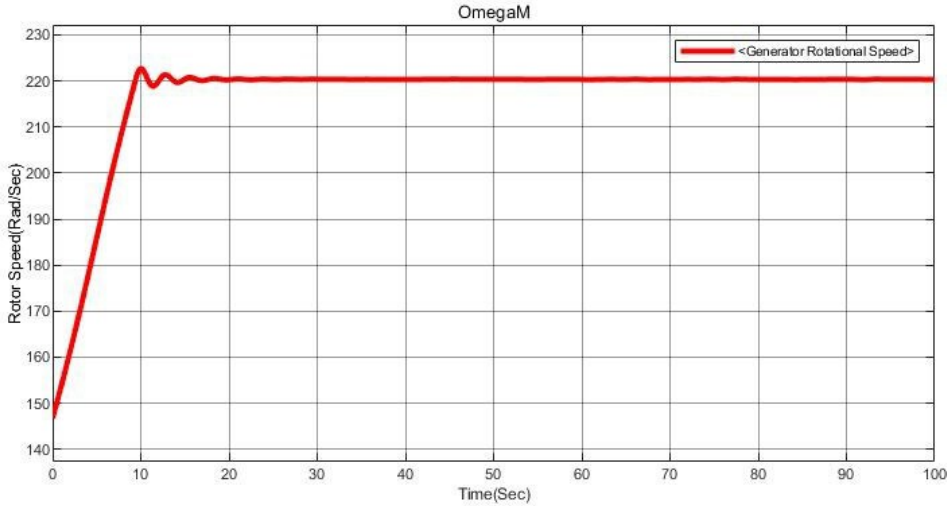

Figure 5: Generator rotational speed.

As wind speed fluctuates and abruptly change overrated speed, pitch angle of blades change also drastically. Figure 6 shows from the simulation results of a PID controller configuration.

Comparison of Transient Response. In this study, both PI and PID configuration of pitch controllers were compared initially with transient responses. Successively, steady state responses for both controllers are also shown. Both controllers perform successful performances as they have stable outputs in terms of reaching maximum power output and generator speed stability. However, their transient dynamics alter in terms of overshoot and settling time. In this manner, PI controller performance can be more efficient.

As denoted in Figure 7, both controllers perform successful operations for 100

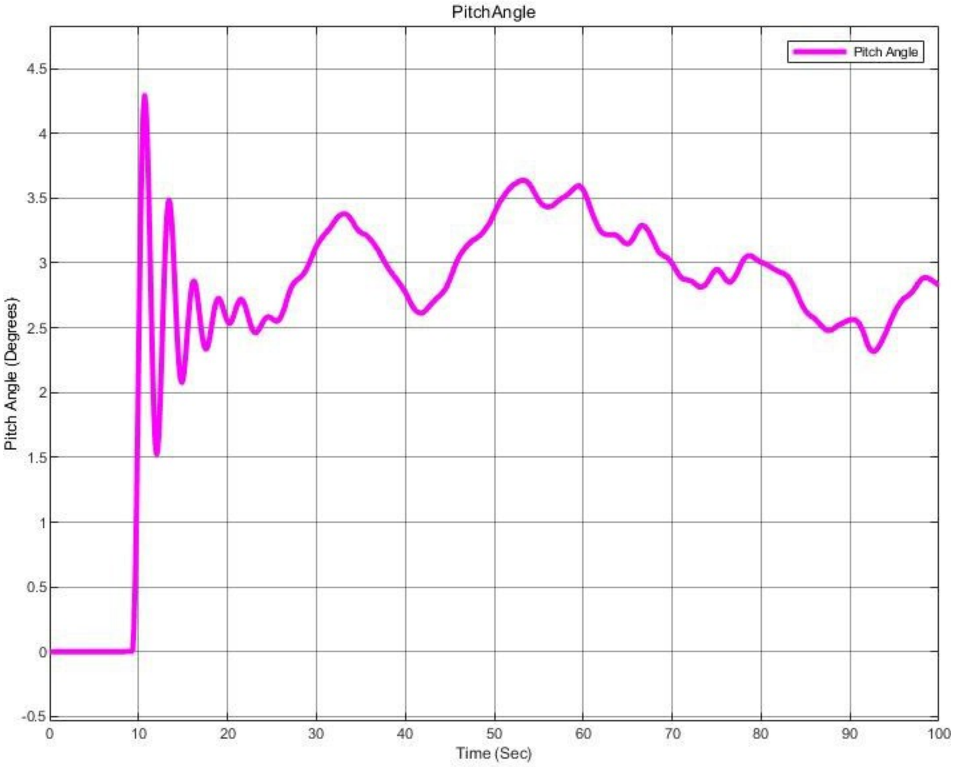

Figure 6: Pitch angle change.

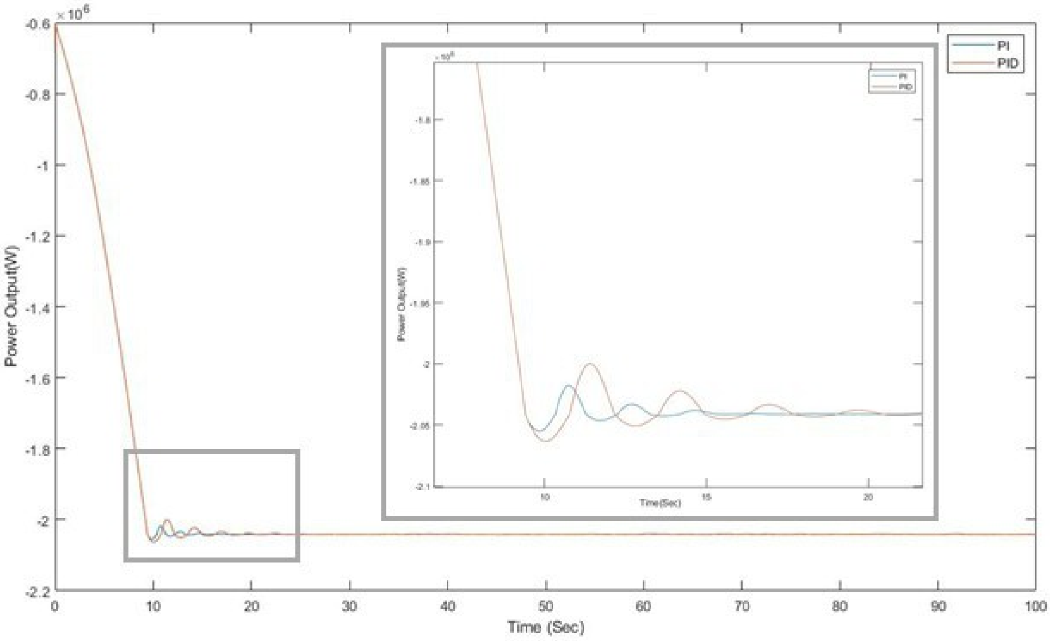

Figure 7: P I& PID Controller results and transient response.

second simulation for steady state characteristics. However, for transient response performances vary. PI and PID controllers denote different transients as overshooting is more stable for PI controller. In addition, rise time, overshoot and settling time for PI and PID controllers are tabulated at Table 2 that is shown below.

Table 2: Transient response results.

Controllers	**PI**	**PID**
Overshoot (Δh)	2 %	4.5 %
Rise time (t_r)	10 s	11 s
Settling time (t_s)	20 s	25.8 s

Comparison of Steady State Response. Unlike the previous transient response, PID controller yields better results than PI controller under steady state in terms of both steady state error and total power production. Necessary results for comparison are tabulated at Table 3.

Table 3: Steady state results.

Controllers	**PI**	**PID**
Steady state error (e_{ss})	0.002	0.001
Total power production		2.4 % (More than PI)

Conclusions

In this study, 2 MW wind turbine with DFIG configuration model was used to perform controller designs with PI and PID techniques. Several simulations were conducted under MATLAB/SIMULINK for a certain wind speed profile that is above rated wind speed. A comparison for the performance under transient response and steady state conditions. It is shown that PI controller performed better under transient state of simulation results whereas PID controller can be stated better for steady state since more power production and less steady state error can be observed.

As a future work of this study, both controllers will be developed for gust wind profiles and tuned to find best parameters.

Acknowledgements

This project was supported by Sabanci University, Istanbul by the tuition waiver of the Ph.D. dissertation of Ahmet Selim Pehlivan.

References

[1] Burton, T., Jenkins, N., Sharpe, D., & Bossanyi, E. (2011a). Wind Energy Handbook (2nd ed.). Wiley.

[2] Civelek, Z., Cam, E., Luy, M., & Mamur, H. (2016). Proportional–integral–derivative parameter optimisation of blade pitch controller in wind turbines by a new intelligent genetic algorithm. IET Renewable

Power Generation, 10(8), 1220–1228. https://doi.org/10.1049/iet-rpg.2016.0029

[3] Jelavic, M., Petrovic, V., & Peric, N. (2017). Estimation based Individual Pitch Control of Wind Turbine. Automatika, 51(2), 181–192. https://doi.org/10.1080/00051144.2010.11828370

[4] Strachan, N. P. W., & Jovcic, D. (2008, July). Improving Wind Power Quality using an Integrated Wind Energy Conversion and Storage System (WECSS). 2008 IEEE Power and Energy Society General Meeting - Conversion and Delivery of Electrical Energy in the 21st Century. https://doi.org/10.1109/pes.2008.4596078

[5] Nam, Y., Kien, P. T., & La, Y.-H. (2013). Alleviating the Tower Mechanical Load of Multi-MW Wind Turbines with LQR Control. Journal of Power Electronics, 13(6), 1024–1031. https://doi.org/10.6113/jpe.2013.13.6.1024

[6] Senjyu, T., Sakamoto, R., Urasaki, N., Funabashi, T., Fujita, H., & Sekine, H. (2006). Output Power Leveling of Wind Turbine Generator for All Operating Regions by Pitch Angle Control. IEEE Transactions on Energy Conversion, 21(2), 467–475. https://doi.org/10.1109/tec.2006.874253

[7] Kamel, R. M., Chaouachi, A., & Nagasaka, K. (2010). RETRACTED: Wind power smoothing using fuzzy logic pitch controller and energy capacitor system for improvement Micro-Grid performance in islanding mode. Energy, 35(5), 2119–2129. https://doi.org/10.1016/j.energy.2010.01.030

[8] Evren, S., Unel, M., & Aksit, M. (2012). Modeling and Control of a Variable Speed Variable Pitch Angle Prototype Wind Turbine. Mathematical and Computational Applications, 18(3), 408–420. https://doi.org/10.3390/mca18030408

[9] Boukhezzar, B., Lupu, L., Siguerdidjane, H., & Hand, M. (2007). Multivariable control strategy for variable speed, variable pitch wind turbines. Renewable Energy, 32(8), 1273–1287. https://doi.org/10.1016/j.renene.2006.06.010

[10] Jianzhong Zhang, Ming Cheng, Zhe Chen, & Xiaofan Fu. (2008). Pitch angle control for variable speed wind turbines. 2008 Third International Conference on Electric Utility Deregulation and Restructuring and Power Technologies. https://doi.org/10.1109/drpt.2008.4523867

[11] Astrom, K. J., & Hagglund, T. (2001). The future of PID control. Control Engineering Practice, 9(11), 1163–1175. https://doi.org/10.1016/s0967-0661(01)00062-4

[12] PID control system analysis and design. (2006). IEEE Control Systems, 26(1), 32–41. https://doi.org/10.1109/mcs.2006.1580152

[13] Civelek, Z., Luy, M., Cam, E., & Barisci, N. (2015). Control of Pitch Angle of Wind Turbine by Fuzzy Pid Controller. Intelligent Automation & Soft Computing, 22(3), 463–471. `https://doi.org/10.1080/10798587.2015.1095417`

[14] Mamur, H. (2014). Design, application, and power performance analyses of a micro wind turbine. Turkish Journal of Electrical Engineering & Computer Sciences, 23, 1619–1637. `https://doi.org/10.3906/elk-1401-174`

[15] Hwas, A., & Katebi, R. (2012). Wind Turbine Control Using PI Pitch Angle Controller. IFAC Proceedings Volumes, 45(3), 241–246. `https://doi.org/10.3182/20120328-3-it-3014.00041`

Genetic Algorithm Optimization of PID Pitch Angle Controller for a 2 MW Wind Turbine

Ahmet Selim Pehlivan[1], Kemalettin Erbatur[2]
[1]spehlivan@sabanciuniv.edu, Department of Mechatronics Engineering, Sabanci University, Istanbul, Turkey
[2]erbatur@sabanciuniv.edu, Department of Mechatronics Engineering, Sabanci University, Istanbul, Turkey

Abstract

Speed regulation of wind turbine rotors are controlled by pitch angle controllers that affect the life expectancy of wind turbines, reliability and power quality. Optimization of wind turbine pitch angle controllers perform crucial effect on the wind turbine dynamics where the speed stability is achieved. In today's modern and commercial wind turbines, blade pitch angle controllers are generally implemented with PI and PID techniques. Determining the controller gain coefficients are one of the most significant problems in order to show a more stable rotor dynamics that eventually leads to better wind turbine performance in terms of both mechanical and electrical qualities. Hence, PID controller was designed and optimized with genetic algorithm technique for a 2 MW DFIG type wind turbine under Matlab-Simulink environment. Gain parameters were optimized for a given wind speed profile from third zone and optimized gain coefficients were achieved within the optimization study. A controller with optimum gain coefficients shows the superior performance than the regular PID performance.

Keywords: Genetic Algorithm, Pitch Angle Controller, Speed Regulation, Wind Energy.

Introduction

Wind turbine (WT) systems with large power scales, blade pitches have to be controlled in order to prevent excessive amount of energy, over speed of a rotor and not to damage the system over nominal wind speeds [1]. This reasoning can be stated as the variable speed WTs provide an opportunity to generate more energy than fixed speed wind turbines [2].

On the other hand, the output power of the variable speed WTs varies due to the uncertainties of the wind speeds. The fluctuations of the wind speeds leads to changes of the voltage and the frequency. However, fixed voltage and a fixed frequency are two of the most important criteria for a quality of electrical energy. In order to improve quality of the output power, appropriate control methods gave to be applied on wind turbine systems [3].

The variable-speed, variable-pitch wind turbine systems typically have two operating regions according to the wind speed. In partial-load region where the wind speed is lower than the rated wind speed v_{rated}, the turbine speed is controlled at the optimal value so that the maximum energy is extracted from the wind turbine [4, 5]. In the full load region where the wind speed exceeds its rated value, the generator output power is limited at the rated value by controlling the pitch angle are limited [6, 7].

One of the most important problems of horizontal axis large-scale wind turbines is that to maximize the power efficiency below the nominal wind speed and limit the nominal power above the nominal wind speeds. [8]. In order to resolve this problem, variable speed variable pitch angle wind turbines can have different torque controller to maximize the power efficiency and pitch controllers to limit the nominal power [9, 10].

Pitch control is one of the most significant subsystem of a modern wind turbine and different control techniques have been applied so far to achieve more efficient wind turbines. Even though many research groups have used many control theories, classical PID controllers are frequently used in today's modern wind turbines commercially. PID controllers have been used in a great deal of wind turbine control applications because of their simple structures, high safety and robustness [11, 12]. Therefore, PID controllers have been employed in order to control system outputs of particular systems that have mathematical models [13, 14].

In this paper, conventional linear PID controller were applied to regulate a 2 MW DFIG type variable speed wind turbine in Matlab Simulink environment. The main purpose of the study was to optimize the PID controller by genetic algorithm methodology with Matlab optimization toolbox. For a certain amount of data sets starting from K_p,K_i and K_d from 10 to 1000 is covered to find an optimum combination of controller gains.

Methodology

Wind turbine modelling and system definition: Wind turbines consists of several subsystems, which can be stated as aerodynamic, mechanical, electromechanical and electrical subsystems. In addition, control systems are also designed separately for all of the subsystem above however, torque control and pitch controllers can be considered as the most significant ones among the others [8].

As illustrated in Figure 1, wind turbines may have a different subsystem from different engineering disciplines where many of them require different controllers. Torque controllers are generally used for DFIG type generators to regulate the powers where pitch controllers are used to regulate the speed of the rotor. In addition, another highly important concept for wind turbine technologies is to classify operating regions since many important descriptions for the turbine are made by the wind regime graphs such as operating speed, determination of maximum power production, maximum available aeromechanical power and so on. Figure 2 shows the operating regions of the 2 MW wind turbine that is used to complete this study.

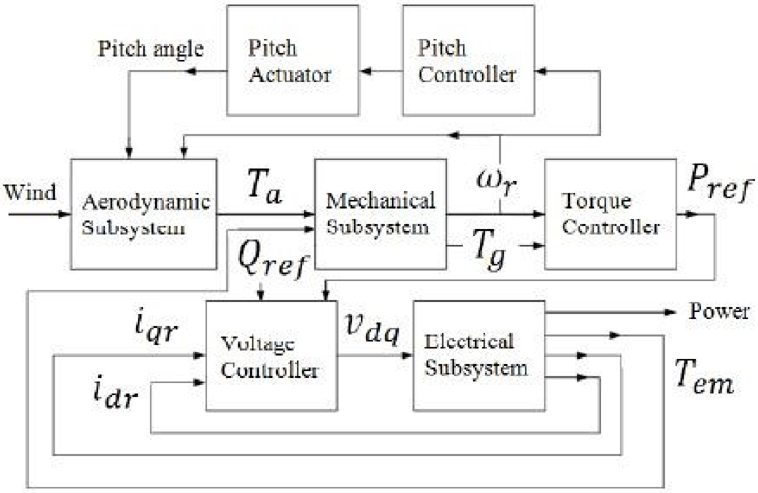

Figure 1: Wind turbine block diagram.

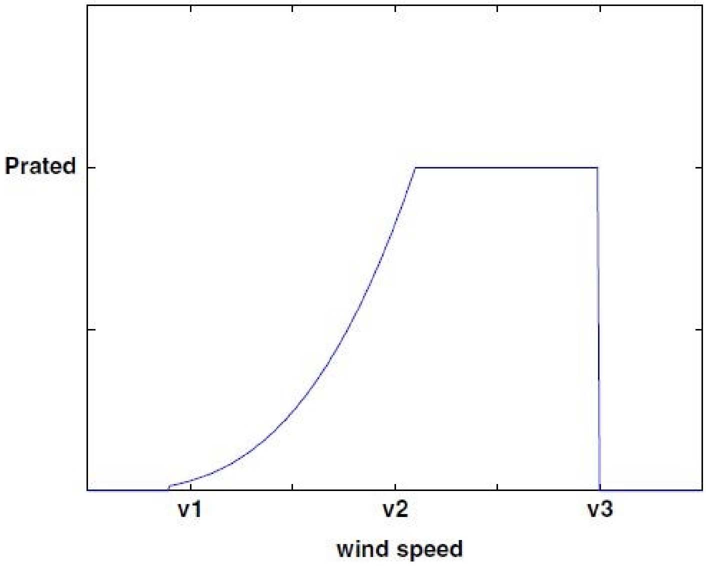

Figure 2: Wind speed regions.

As can be seen from the figure, wind profile is divided in three zone according to wind speed in which zone 1, zone 2, zone 3 can be named as cut in, rated and active and cut off respectively. Wind turbines generally starts to produce electricity with the wind speed of cut in. Until the rated wind speed, pitch system operates as Maximum Power Point Tracking (MPPT) mode with 0 degrees of pitch. While the wind speed increases, pitch system keeps maximizing the power output from the available aeromechanical power. Zone 2 is generally considered as partial load region where pitch system may start to become active to have more efficient power output performance. If the wind speed is more than rated speed, than pitch system becomes active while the wind speed increases, rotation and power is limited with higher pitch angles. Zone 3 can be considered as active pitch region above rated wind speed where the power is regulated by active pitching. After wind speed exceeds or gets near to cut off speed wind turbines are stopped due to mechanical safety reason by using pitch control [15].

Modelling of aerodynamic, mechanical, electromechanical, grid side converters on a simulation environment is a significant issue to conduct a better study for performance comparison. Throughout the study, 2 MW DFIG type variable speed and variable pitch wind turbine is under Matlab/Simulink environment used with a wind regime that is above rated speed. The aim of this certain wind regime is to observe the effect of pitching under abrupt changes of wind speed and the power regulation characteristics. Table 1 depicts the parameters for the wind turbine simulated throughout the controller design study.

Table 1: Wind turbine system parameters.

Nominal output power	2 MW	Nominal rotor speed	15.8 rpm
Working mode	Grid connection	Gear box rate	1:94.7
Cut in wind speed	3 m/s	Generator pole pair	2
Nominal wind speed	12 m/s	Generator type	DFIG
Cut out wind speed	25 m/s	Generator synchronous speed	1500 rpm
Rotor diameter	82.6 m	Generator voltage	690 V
Rotor swept area	5359		

Genetic Algorithm Methodology: In the study, ITAE (Integral Time Absolute Error) technique was applied to measure the error. The calculated error is logged on the block for the objective function.

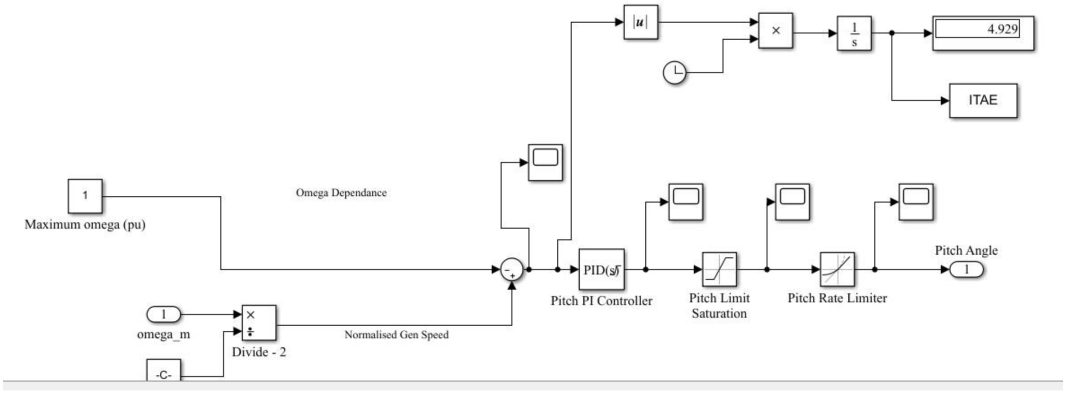

Figure 3: ITAE technique for objective function.

As mentioned previously, genetic algorithm study is applied to find an optimum gain combination for the PID controller.

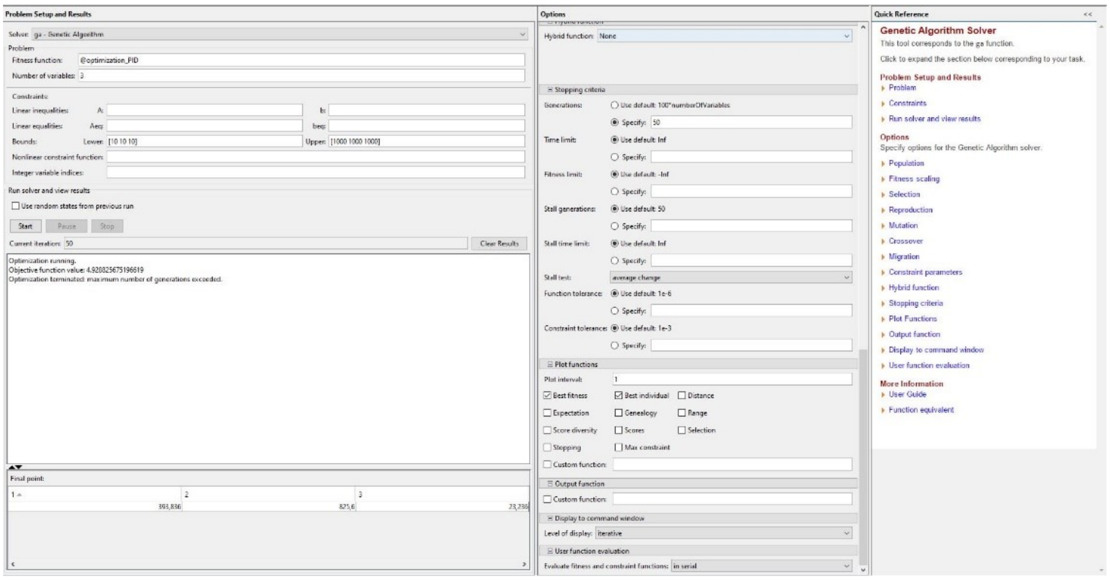

Solver: ga - Genetic Algorithm

Fitness function: @optimization_PID

Number of variables: 3

Linear inequalities: A: b:

Linear equalities: Aeq: beq:

Bounds: Lower: [10 10 10] Upper: [1000 1000 1000]

Nonlinear constraint function:

Integer variable indices:

☐ Use random states from previous run

Current iteration: 50

```
Optimization running.
Objective function value: 4.928825675196619
Optimization terminated: maximum number of generations exceeded.
```

Final point:

1	2	3
393,836	825,6	23,236

Hybrid function: None

Generations: ○ Use default: 100*numberOfVariables ● Specify: 50

Time limit: ● Use default: Inf ○ Specify:

Fitness limit: ● Use default: -Inf ○ Specify:

Stall generations: ● Use default: 50 ○ Specify:

Stall time limit: ● Use default: Inf ○ Specify:

Stall test: average change

Function tolerance: ● Use default: 1e-6 ○ Specify:

Constraint tolerance: ● Use default: 1e-3 ○ Specify:

Plot interval: 1

☑ Best fitness ☑ Best individual ☐ Distance

☐ Expectation ☐ Genealogy ☐ Range

☐ Score diversity ☐ Scores ☐ Selection

☐ Stopping ☐ Max constraint

☐ Custom function:

☐ Custom function:

Level of display: iterative

Evaluate fitness and constraint functions: in serial

Figure 4: Optimization boundary conditions.

Results and Discussion

As mentioned previously, PID controller was previously designed for the pitch angle controller and was optimized by Genetic Algorithm toolbox of Matlab. After the simulation runs for 2500 iterations, local optimum point was reached with (384, 826, 24) for K$_p$,K$_i$ and K$_d$ respectively.

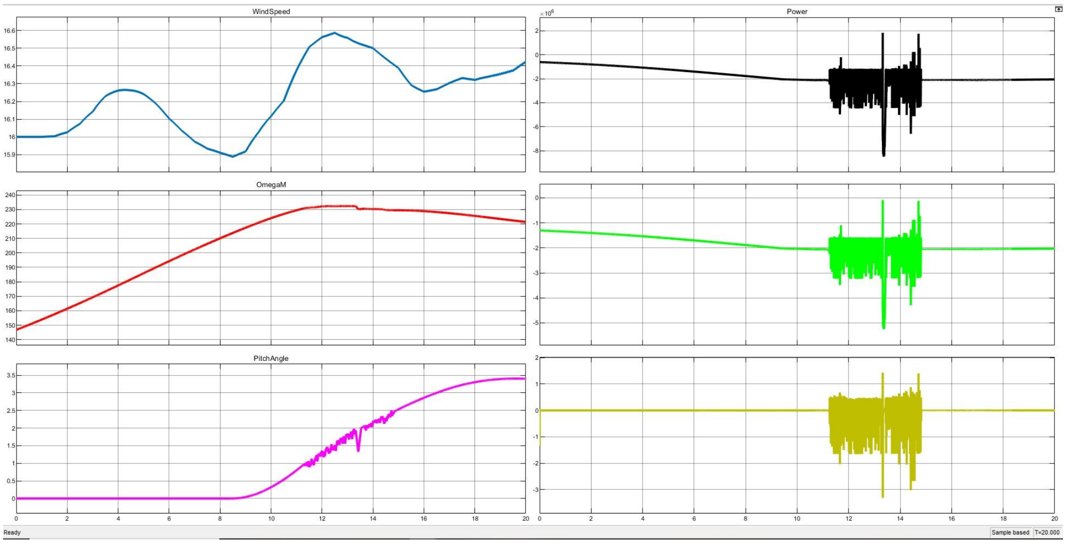

Figure 5: Simulation with initial gains.

As can be seen from the Figure 5, 20 seconds of simulation was conducted initial gains were selected as (10,10,10) for the gains. As the gains are very low, control action cannot be seen effectively therefore small chatters can be seen.

As illustrated in Figure 6, optimization runs lead to more efficient performance in terms of generator speed and quality of the electrical power. Moreover , one

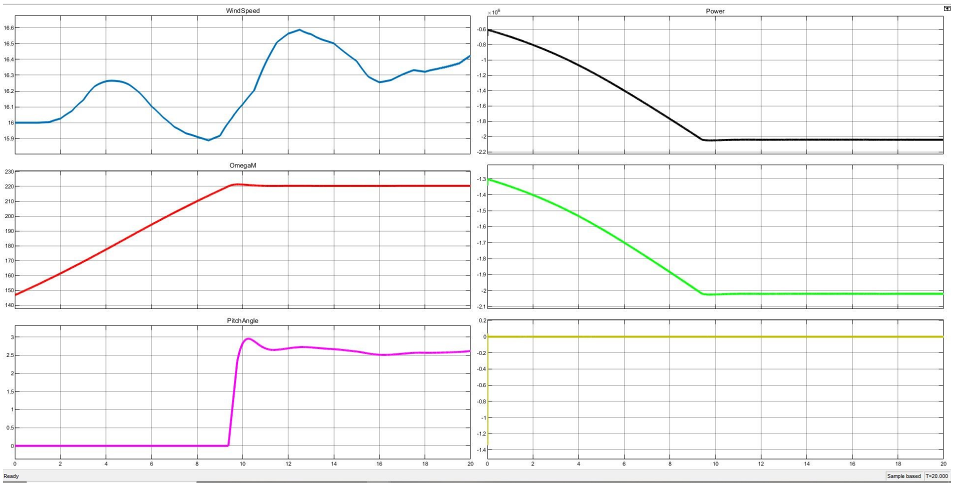

Figure 6: Best fit simulation.

local optimum point is achieved among the data range. K_p,K_i and K_d are found as 384, 826 and 34.

Conclusions

In this study, 2 MW wind turbine with DFIG configuration model was used to perform controller designs PID technique. Several simulations were conducted under MATLAB/SIMULINK for a certain wind speed profile that is above rated wind speed. PID controller was optimized with genetic algorithm technique to reach the local optimum combination for the gain set.

As a future work of this study, global optimum combination for the given interval is to be searched with genetic algorithm and particle swarm methodology will be applied.

Acknowledgements

This project was supported by Sabanci University, Istanbul by the tuition waiver of the Ph.D. dissertation of Ahmet Selim Pehlivan.

References

[1] Burton, T., Jenkins, N., Sharpe, D., & Bossanyi, E. (2011a). Wind Energy Handbook (2nd ed.). Wiley.

[2] Civelek, Z., Cam, E., Luy, M., & Mamur, H. (2016). Proportional–integral–derivative parameter optimisation of blade pitch controller in wind turbines by a new intelligent genetic algorithm. IET Renewable Power Generation, 10(8), 1220–1228. `https://doi.org/10.1049/iet-rpg.2016.0029`

[3] Jelavic, M., Petrovic, V., & Peric, N. (2017). Estimation based Individual Pitch Control of Wind Turbine. Automatika, 51(2), 181–192. `https://doi.org/10.1080/00051144.2010.11828370`

[4] Strachan, N. P. W., & Jovcic, D. (2008, July). Improving Wind Power Quality using an Integrated Wind Energy Conversion and Storage System (WECSS). 2008 IEEE Power and Energy Society General Meeting - Conversion and Delivery of Electrical Energy in the 21st Century. `https://doi.org/10.1109/pes.2008.4596078`

[5] Nam, Y., Kien, P. T., & La, Y.-H. (2013). Alleviating the Tower Mechanical Load of Multi-MW Wind Turbines with LQR Control. Journal of Power Electronics, 13(6), 1024–1031. `https://doi.org/10.6113/jpe.2013.13.6.1024`

[6] Senjyu, T., Sakamoto, R., Urasaki, N., Funabashi, T., Fujita, H., & Sekine, H. (2006). Output Power Leveling of Wind Turbine Generator for All Operating Regions by Pitch Angle Control. IEEE Transactions on Energy Conversion, 21(2), 467–475. `https://doi.org/10.1109/tec.2006.874253`

[7] Kamel, R. M., Chaouachi, A., & Nagasaka, K. (2010). RETRACTED: Wind power smoothing using fuzzy logic pitch controller and energy capacitor system for improvement Micro-Grid performance in islanding mode. Energy, 35(5), 2119–2129. `https://doi.org/10.1016/j.energy.2010.01.030`

[8] Evren, S., Unel, M., & Aksit, M. (2012). Modeling and Control of a Variable Speed Variable Pitch Angle Prototype Wind Turbine. Mathematical and Computational Applications, 18(3), 408–420. `https://doi.org/10.3390/mca18030408`

[9] Boukhezzar, B., Lupu, L., Siguerdidjane, H., & Hand, M. (2007). Multivariable control strategy for variable speed, variable pitch wind turbines. Renewable Energy, 32(8), 1273–1287. `https://doi.org/10.1016/j.renene.2006.06.010`

[10] Jianzhong Zhang, Ming Cheng, Zhe Chen, & Xiaofan Fu. (2008). Pitch angle control for variable speed wind turbines. 2008 Third International Conference on Electric Utility Deregulation and Restructuring and Power Technologies. `https://doi.org/10.1109/drpt.2008.4523867`

[11] Astrom, K. J., & Hagglund, T. (2001). The future of PID control. Control Engineering Practice, 9(11), 1163–1175. `https://doi.org/10.1016/s0967-0661(01)00062-4`

[12] PID control system analysis and design. (2006). IEEE Control Systems, 26(1), 32–41. `https://doi.org/10.1109/mcs.2006.1580152`

[13] Civelek, Z., Luy, M., Cam, E., & Barisci, N. (2015). Control of Pitch Angle of Wind Turbine by Fuzzy Pid Controller. Intelligent Automation & Soft Computing, 22(3), 463–471. `https://doi.org/10.1080/10798587.2015.1095417`

[14] Mamur, H. (2014). Design, application, and power performance analyses of a micro wind turbine. Turkish Journal of Electrical Engineering & Computer Sciences, 23, 1619–1637. `https://doi.org/10.3906/elk-1401-174`

[15] Hwas, A., & Katebi, R. (2012). Wind Turbine Control Using PI Pitch Angle Controller. IFAC Proceedings Volumes, 45(3), 241–246. `https://doi.org/10.3182/20120328-3-it-3014.00041`

A Novel Hybrid System for Boron Removal and Eco-Electricity Production

Cagdas Saz[1], Cengiz Ture[2], Onur Can Turker[3], Anil Yakar[4]
[1]cagdassaz@eskisehir.edu.tr, Department of Biology, Eskisehir Technical University, Eskisehir, Turkey
[2]cture@eskisehir.edu.tr, Department of Biology, Eskisehir Technical University, Eskisehir, Turkey
[3]octurker@aksaray.edu.tr, Department of Biology, Aksaray University, Aksaray, Turkey
[4]ayakar@eskisehir.edu.tr, Department of Biology, Eskisehir Technical University, Eskisehir, Turkey

Abstract

Plant-based waste water treatment systems (PWTS) are thought to play crucial potential to clean and improve the quality of various waste water types. The desire to explore waste water treatment technologies using eco-friendly and green energy systems led to the integration of plant-based waste water treatment systems and electro-coagulation systems (EC), leading to the emergence of new hybrid technology. In this study, the treatment and eco-electricity performance of PWTS-EC were evaluated for 4 days to remove boron (B) from synthetic waste water. The systems are designed in 7 different combinations using sludge (S), *Lemna gibba* (L), and presence oxygen (O) parameters. Treatment and eco-electric power generation performance of the systems (SLO, LO, LS, SO, L, S, O) were compared with a control system. The average B treatment performances were recorded as 48.47%, 33.59%, 35.04%, 30.62%, 29.6%, 26.46%, 22.43%, 16.61% for SLO, LO, LS, SO, L, S, O, and control, respectively. In addition, eco-electrical generation performances were varied between 1.20 and 0.7 V with an open-circuit connection. According to the present results, the SLO system was found as a more efficient system comparing the systems in terms of B treatment and eco-electricity production performance. The results of this experiment prove that PWTS-EC can be used as an alternative and low cost, low energy and renewable alternative treatment method for B contaminated waste water treatment and eco-electricity production.

Keywords: Plant-based electro-coagulation system, Lemna gibba, Boron treatment, Eco-electricity production.

Introduction

Fossil fuels, renewable energy, and nuclear power are three different categories of energy sources. Renewable energy can never get exhausted because it is constantly renewed. Moreover, it can be directly used or converted into other forms of energy.

Wind energy is the most widely used renewable energy source [1–3]. Boron (B) is a naturally occurring element found in freshwater ecosystems in most parts of the world in concentrations less than 1 mg/L [1–3]. Therefore, they are released into aquatic ecosystems through natural processes such as leaching of salt deposits and weathering of minerals from rocks, as well as man-made glass industry waste water sources, mining activities, oil and gas production (produced waters), and run-off effluents from areas where B-containing agrochemicals are used [4, 5]. The waste water released to ecosystems as a result of these activities are generally quite high in terms of B content. Besides, another mechanism affecting B content, especially in aquatic ecosystems, is anthropogenic resources [2–5] In the case of using detergents and cleaning products enriched with borax, water-soluble B forms such as boric acid are easily discharged into sewage treatment systems with domestic waste water and cause pollution by being transported to the aquatic ecosystem. [5, 6]. While B at low concentrations (up to 0.3 mg/L) is the main nutrient for plants, high concentrations are toxic for plants [7, 8]. B toxicity, especially in Australia, the United States of America, North Africa, and Turkey, is an environmental problem, including natural and crop plants grown in semi-arid and arid regions [9–11]. In addition, the World Health Organization determined the safe B rate in drinking water as 2.4 mg/L in 2009 [12–15]. B coming from domestic waste water to sewage treatment systems cannot be removed to a largely due to the high maintenance costs of traditional methods in sewage treatment systems (reverse osmosis, ion exchange techniques, activated sludge, etc.) [2–15].

Nowadays, industrialization and economic developments, which have gained speed with population growth, have brought the demand for water resources [16]. With the increasing demand, access to clean water resources and water pollution negatively affect the ecosystem [17]. The negative impact on water resources has encouraged governments and companies to use cost-effective and energy-efficient alternative treatment technologies in their environmental policies [18, 19]. In this direction, the demand for phytoremediation and electro-coagulation (EC) methods has been increasing in recent years [20, 21]. Plant-based waste water treatment systems (PWTS) are widely used within the scope of PWTS applications due to their functions such as high pollutant removal efficiency, easy operation, and maintenance, low cost, good water potential, allowing water to exist. Because of these functions, PWTS is considered a sustainable waste water management option [22–24]. PWTS are a cost-effective and environmentally friendly engineering system capable of removing organic matter and various metals and metalloids (B, As, and Zn) from waste water using a range of biological [25–27], chemical [28], and physical mechanisms [29, 30].

From another point of view, the EC process is also used as a low-cost and environmentally friendly technology for the treatment of water containing heavy metals, organic compounds, oil [31–35]. It is a compact system of EC, consisting of electrolysis and coagulation steps [36]. The simplest structure of an EC system consists of an electrolytic cell containing an anode and a cathode [37, 38]. At this stage, although there are many studies on the use of Fe and Al electrodes, the use of magnesium electrodes in the EC process is also a new ecological method

[36–38]. The traditional EC system is based on the principle of applying current from an external power source to the anode and cathode [37]. However, Dong et al. (2016) on the other hand, the anode and cathode provide the electrolysis process by generating their energy through an external resistor. Therefore, an ecological approach has been displayed with this use and it has been pointed out that effective energy saving can be achieved.

The desire to explore waste water treatment technologies using ecological and green energy systems has led to the emergence of new hybrid technologies (PWTS-EC) with the integration of PWTS and EC systems. In this hybrid technology, while organic substances are broken down thanks to the mud, oxygen, electrode, and plant in the system, eco-electricity is produced by keeping the free electrons released through the closed-circuit system [5, 38].

In this study, the boron treatment and eco-electricity generation performance of PWTS-EC reactors in different combinations were investigated to remove B from synthetic waste water contaminated with B.

Materials And Methods

Lemna gibba Eskisehir in Turkey was collected from a natural wetland located. To maximize plant growth, Hoagland's solution was used as a suitable medium. *L. gibba* leaves were cultured according to the OECD test protocol for the duration of the experiment [39]. Following the culture period, bright green and healthy 4 grams *L. gibba* were carefully placed in the reactors.

The sludge used in the reactors was fed with Hoagland media and waste water (from an industrial waste water treatment facility) for 5 days before the experiment began.

The study was carried out under lamps with 5 W light power at room temperature (24 ± 2°C) in Eskisehir Technical University Science Faculty Plant Ecology Laboratory. Eight plastic containers with dimensions of 33 cm × 23 cm × 15 cm and a volume of 10 L were used for the reactors in which PWTS-EC processes were carried out. Each reactor consisted of two sections called the anode (21 cm) and the cathode (11 cm). The reactors were being separated from each other by glass wool (1 cm), which is a permeable selective membrane. For water samples taken from the reactors, taps have been integrated into the parts of the anode sections close to the ground. The sludge (S), *L. gibba* (L), and oxygen (O) parameters were placed in the anode compartments of the reactors in different combinations (SLO, LO, LS, SO, L, S, O) In the control reactor, the anode and cathode compartments are left empty. The cathode electrode selected as the eco-electrode in the reactors is made of 10 cm × 5 cm × 1 cm graphite felt, and the anode electrode consists of 5 cm × 5 cm × 0.3 cm magnesium (Mg) plates that do not harm the environment. Conductive copper electric cable was passed through anode and cathode electrodes and connected with an external resistance of 30-50 Ω. The electrolysis circuit was completed by ensuring the decomposition of organic substances in water for 8 hours with the effect of the current density created by the external resistance. At the end of 8 hours, 500 ml of water was taken from the anode compartment and transferred to the cathode area and the coagulation phase, which is the second period of 16 hours without external resistance. At the end of the period, 500 ml of water was taken from the cathode area and was analysed.

In the study, the synthetic waste water rich in organic matter proposed by Liu et al. (2013) [40] was modified by contaminating with boron. To determine the B, chemical oxygen demand (COD), ammonium (NH_4^+), and removal efficiencies of each reactor (1, 4, and 7 days) The parameters of pH, Electrical Conductivity (EC), Dissolved Oxygen (DO), and Redox Potential (ORP), temperature (t) were determined daily by the HACH HQ40D multi-parameter. B concentration in water samples was determined by the carminic acid method [15]. COD values of the water samples were determined with HACH DR/890. NH4+concentrations were measured using the INTELLICAL ISE ammonium electrode [41]. The eco-electricity generation performance of each reactor was measured daily with Fluke 287 TRUE RMS. According to the close circuit procedure, the cathode and anode are connected by wires and resistance (1000 Ω), and then the potential between the edges of the resistor is monitored [15, 41, 42].

Results and Discussion

The average values of physicochemical parameters (pH, EC, ORP, t, DO) of the influent and effluent of PWTS-EC reactors during the experimental period are shown in Table 1.

Table 1: Average Values of Inflow and Effluent Physicochemical Parameters.

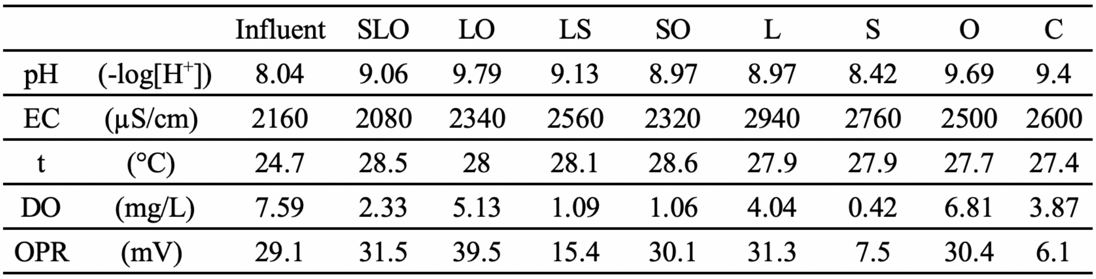

		Influent	SLO	LO	LS	SO	L	S	O	C
pH	**(-log[H⁺])**	**8.04**	**9.06**	**9.79**	**9.13**	**8.97**	**8.97**	**8.42**	**9.69**	**9.4**
EC	**(µS/cm)**	**2160**	**2080**	**2340**	**2560**	**2320**	**2940**	**2760**	**2500**	**2600**
t	**(°C)**	**24.7**	**28.5**	**28**	**28.1**	**28.6**	**27.9**	**27.9**	**27.7**	**27.4**
DO	**(mg/L)**	**7.59**	**2.33**	**5.13**	**1.09**	**1.06**	**4.04**	**0.42**	**6.81**	**3.87**
OPR	**(mV)**	**29.1**	**31.5**	**39.5**	**15.4**	**30.1**	**31.3**	**7.5**	**30.4**	**6.1**

During the experimental days of PWTS-EC reactors, it was determined that the pH values in the outlet samples were higher than the inlet water samples. In addition, the highest pH value was observed in the LO reactor (9.79), while the lowest value was observed in the S reactor (8.42). This indicates that *L. gibba* and oxygen configurations especially in PWTS-EC reactors reduce the amount of CO_2 consumption. Similar observations were reported by Krishna and Polprasert (2008), who used duckweed-based waste water treatment systems in their experimental processes, and it was observed that the pH values at the inlet increased from C 6.9-7.5 to 7.5-8.4 during the experimental period. It is seen that the DO values increased like pH during the experiment period. On the other hand, it is observed that the EC and redox values of the effluent of the reactors follow a fluctuating course compared to the influent.

During the experimental period, the B, COD, and NH_4^+ concentrations of the influent and effluent of the reactors were determined and the percentage treatment amounts according to the influent water are given in Table 2. According to the analysis results, it is seen that the B, COD, and NH_4^+ removal percentages in PWTS-EC reactors are higher than the output values of the control reactor. The B, COD and NH_4^+ removal rates of the final output samples of the PWTS-EC reactors were respectively: SLO>LO>LS>SO>L>S>O>C. From these results, it can be concluded that S, O, and L, which are parameters in PWTS-EC reactors, slightly catalyse the removal of B, COD and NH_4^+.

Table 2: Average Removal Amounts of NH_4^+, B, and COD and Average Eco-Electricity Production.

	SLO	LO	LS	SO	L	S	O	C
NH_4^+ Removal (%)	48.5	33.6	35	30.6	29.4	26.5	22.4	16.6
B Removal (%)	78.3	70.5	67.3	54.1	41.2	40.8	35.7	29.3
COD Removal (%)	65.7	60.1	54.2	50.3	45.6	40.2	35.1	24.5
Eco-electricity production (open circuit) (V)	1.2	0.9	1.17	1.14	1.2	0.84	0.75	0.7
Eco-electricity production (close circuit) (V)	0.78	0.58	0.76	0.78	0.74	0.54	0.48	0.45

The eco-electric values of the reactors, which are measured and averaged every day in open-circuit and closed-circuit conditions, are also shown in Table 2. When the open circuit results are examined, although SLO = L>LS>SO>LO>O>S>C, the closed-circuit results show the order SLO = SO>LS>L>LO>SO>O>C. When the open circuit and closed-circuit eco-electricity production performances of the reactors are evaluated together, it is concluded that the presence of sludge in the environment positively affects the eco-electricity generation performance in general. It is a fact that this situation positively affects B, NH_4^+, and COD removal rates.

In light of all data, it was determined that the SLO reactor showed higher purification and eco-electricity generation efficiency compared to all other reactors. When all results are examined, the electrolysis process in this new hybrid technology reactors is provided by anode and cathode electrodes that generate their energy through an external resistance. In this way, in addition to high water treatment, effective energy saving has been achieved. Also, unlike Al and Fe electrodes used as electrodes, an ecological approach was demonstrated using graphite felt and Mg. Results from the present study reveal that the SLO combination PWTS-EC treatment system has the potential for B, NH_4^+, and COD removal and that such systems can generate renewable energy from waste with an ecological approach. It is thought that the eco-electricity produced by integrating PWTS-EC systems with power management systems will be sufficient to operate low energy devices.

References

[1] WHO, 2003. Boron in Drinking Water. World Health Organization, Geneva, Switzerland.

[2] Hasenmueller, E. A., & Criss, R. E. (2013). Multiple sources of boron in urban surface waters and groundwaters. Science of The Total Environment, 447, 235–247. `https://doi.org/10.1016/j.scitotenv.2013.01.001`

[3] Chen, M., Dollar, O., Shafer-Peltier, K., Randtke, S., Waseem, S., & Peltier, E. (2020). Boron removal by electrocoagulation: Removal mechanism, adsorption models and factors influencing removal. Water Research, 170, 115362. `https://doi.org/10.1016/j.watres.2019.115362`

[4] Turker, O. C., Yakar, A., & Gur, N. (2017). Bioaccumulation and toxicity assessment of irrigation water contaminated with boron (B) using duckweed (Lemna gibba L.) in a batch reactor system. Journal of Hazardous Materials, 324, 151–159. `https://doi.org/10.1016/j.jhazmat.2016.10.044`

[5] Turker, O. C. (2018). Simultaneous boron (B) removal and electricity generation from domestic wastewater using duckweed-based wastewater treatment reactors coupled with microbial fuel cell. Journal of Environmental Management, 228, 20–31. `https://doi.org/10.1016/j.jenvman.2018.08.112`

[6] Wolska, J., & Bryjak, M. (2013). Methods for boron removal from aqueous solutions — A review. Desalination, 310, 18–24. `https://doi.org/10.1016/j.desal.2012.08.003`

[7] Hilal, N., Kim, G. J., & Somerfield, C. (2011). Boron removal from saline water: A comprehensive review. Desalination, 273(1), 23–35. `https://doi.org/10.1016/j.desal.2010.05.012`

[8] [Yildirim, K., & Kasim, G. C. (2018). Phytoremediation potential of poplar and willow species in small scale constructed wetland for boron removal. Chemosphere, 194, 722–736. `https://doi.org/10.1016/j.chemosphere.2017.12.036`

[9] Kabay, N., Yilmaz, I., Bryjak, M., & Yuksel, M. (2006). Removal of boron from aqueous solutions by a hybrid ion exchange–membrane process. Desalination, 198(1–3), 158–165. `https://doi.org/10.1016/j.desal.2006.09.011`

[10] Turker, O. C., & Baran, T. (2017). Evaluation and application of an innovative method based on various chitosan composites and Lemna gibba for boron removal from drinking water. Carbohydrate Polymers, 166, 209–218. `https://doi.org/10.1016/j.carbpol.2017.02.106`

[11] Gur, N., Turker, O. C., & Bocuk, H. (2016). Toxicity assessment of boron (B) by Lemna minor L. and Lemna gibba L. and their possible use as model

plants for ecological risk assessment of aquatic ecosystems with boron pollution. Chemosphere, 157, 1–9. `https://doi.org/10.1016/j.chemosphere.2016.04.138`

[12] WHO, 2011. Guidelines for Drinking-Water Quality, fourth ed. World Health Organization, Geneva, Switzerland.

[13] Guan, Z., Lv, J., Bai, P., & Guo, X. (2016). Boron removal from aqueous solutions by adsorption - A review. Desalination, 383, 29–37. `https://doi.org/10.1016/j.desal.2015.12.026`

[14] Turker, O. C., Vymazal, J., & Ture, C. (2014). Constructed wetlands for boron removal: A review. Ecological Engineering, 64, 350–359. `https://doi.org/10.1016/j.ecoleng.2014.01.007`

[15] Turker, O. C., Ture, C., Yakar, A., & Saz, Ç. (2017). Engineered wetland reactors with different media types to treat drinking water contaminated by boron (B). Journal of Cleaner Production, 168, 823–832. `https://doi.org/10.1016/j.jclepro.2017.09.067`

[16] Astiaso Garcia, D. (2017). Green areas management and bioengineering techniques for improving urban ecological sustainability. Sustainable Cities and Society, 30, 108–117. `https://doi.org/10.1016/j.scs.2017.01.008`

[17] Gill, S. E., Handley, J. F., Ennos, A. R., Pauleit, S., Theuray, N., & Lindley, S. J. (2008). Characterising the urban environment of UK cities and towns: A template for landscape planning. Landscape and Urban Planning, 87(3), 210–222. `https://doi.org/10.1016/j.landurbplan.2008.06.008`

[18] Kopnina, H. (2014). Education for sustainable development (ESD) as if environment really mattered. Environmental Development, 12, 37–46. `https://doi.org/10.1016/j.envdev.2014.09.001`

[19] Klein, L. R., Hendrix, W. G., Lohr, V. I., Kaytes, J. B., Sayler, R. D., Swanson, M. E., Elliot, W. J., & Reganold, J. P. (2015). Linking ecology and aesthetics in sustainable agricultural landscapes: Lessons from the Palouse region of Washington, U.S.A. Landscape and Urban Planning, 134, 195–209. `https://doi.org/10.1016/j.landurbplan.2014.10.019`

[20] Vymazal, J. (2013). The use of hybrid constructed wetlands for wastewater treatment with special attention to nitrogen removal: A review of a recent development. Water Research, 47(14), 4795–4811. `https://doi.org/10.1016/j.watres.2013.05.029`

[21] Devlin, T. R., Kowalski, M. S., Pagaduan, E., Zhang, X., Wei, V., & Oleszkiewicz, J. A. (2019). Electrocoagulation of wastewater using aluminum, iron, and magnesium electrodes. Journal of Hazardous Materials, 368, 862–868. `https://doi.org/10.1016/j.jhazmat.2018.10.017`

[22] Alkimin, G. D., Daniel, D., Frankenbach, S., Serodio, J., Soares, A. M. V. M., Barata, C., & Nunes, B. (2019). Evaluation of pharmaceutical toxic effects of non-standard endpoints on the macrophyte species Lemna minor and Lemna gibba. Science of The Total Environment, 657, 926–937. `https://doi.org/10.1016/j.scitotenv.2018.12.002`

[23] Vymazal, J. (2007). Removal of nutrients in various types of constructed wetlands. Science of The Total Environment, 380(1–3), 48–65. `https://doi.org/10.1016/j.scitotenv.2006.09.014`

[24] Ceschin, S., Sgambato, V., Ellwood, N. T. W., & Zuccarello, V. (2019). Phytoremediation performance of Lemna communities in a constructed wetland system for wastewater treatment. Environmental and Experimental Botany, 162, 67–71. `https://doi.org/10.1016/j.envexpbot.2019.02.007`

[25] Bocuk, H., Yakar, A., & Turker, O. C. (2013). Assessment of Lemna gibba L. (duckweed) as a potential ecological indicator for contaminated aquatic ecosystem by boron mine effluent. Ecological Indicators, 29, 538–548. `https://doi.org/10.1016/j.ecolind.2013.01.029`

[26] Sasmaz, A., & Obek, E. (2009). The accumulation of arsenic, uranium, and boron in Lemna gibba L. exposed to secondary effluents. Ecological Engineering, 35(10), 1564–1567. `https://doi.org/10.1016/j.ecoleng.2009.06.007`

[27] Verma, R., & Suthar, S. (2014). Synchronized urban wastewater treatment and biomass production using duckweed Lemna gibba L. Ecological Engineering, 64, 337–343. `https://doi.org/10.1016/j.ecoleng.2013.12.055`

[28] Priya, A., Avishek, K., & Pathak, G. (2011). Assessing the potentials of Lemna minor in the treatment of domestic wastewater at pilot scale. Environmental Monitoring and Assessment, 184(7), 4301–4307. `https://doi.org/10.1007/s10661-011-2265-6`

[29] Bal Krishna, K. C., & Polprasert, C. (2008). An integrated kinetic model for organic and nutrient removal by duckweed-based wastewater treatment (DUBWAT) system. Ecological Engineering, 34(3), 243–250. `https://doi.org/10.1016/j.ecoleng.2008.08.013`

[30] Sims, A., Gajaraj, S., & Hu, Z. (2013). Nutrient removal and greenhouse gas emissions in duckweed treatment ponds. Water Research, 47(3), 1390–1398. `https://doi.org/10.1016/j.watres.2012.12.009`

[31] Daneshvar, N., Oladegaragoze, A., & Djafarzadeh, N. (2006). Decolorization of basic dye solutions by electrocoagulation: An investigation of the effect of operational parameters. Journal of Hazardous Materials, 129(1–3), 116–122. `https://doi.org/10.1016/j.jhazmat.2005.08.033`

[32] Fajardo, A. S., Rodrigues, R. F., Martins, R. C., Castro, L. M., & Quinta-Ferreira, R. M. (2015). Phenolic wastewaters treatment by electrocoagulation

process using Zn anode. Chemical Engineering Journal, 275, 331–341. `https://doi.org/10.1016/j.cej.2015.03.116`

[33] Holt, P. K., Barton, G. W., & Mitchell, C. A. (2005). The future for electrocoagulation as a localised water treatment technology. Chemosphere, 59(3), 355–367. `https://doi.org/10.1016/j.chemosphere.2004.10.023`

[34] Canizares, P., Martinez, F., Rodrigo, M., Jimenez, C., Saez, C., & Lobato, J. (2008). Modelling of wastewater electrocoagulation processes Part I. General description and application to kaolin-polluted wastewaters. Separation and Purification Technology, 60(2), 155–161. `https://doi.org/10.1016/j.seppur.2007.08.003`

[35] Hakizimana, J. N., Gourich, B., Chafi, M., Stiriba, Y., Vial, C., Drogui, P., & Naja, J. (2017). Electrocoagulation process in water treatment: A review of electrocoagulation modeling approaches. Desalination, 404, 1–21. `https://doi.org/10.1016/j.desal.2016.10.011`

[36] Chen, G. (2004). Electrochemical technologies in wastewater treatment. Separation and Purification Technology, 38(1), 11–41. `https://doi.org/10.1016/j.seppur.2003.10.006`

[37] Chen, X., Chen, G., & Yue, P. L. (2000). Separation of pollutants from restaurant wastewater by electrocoagulation. Separation and Purification Technology, 19(1–2), 65–76. `https://doi.org/10.1016/s1383-5866(99)00072-6`

[38] Dong, Y., Qu, Y., Li, C., Han, X., Ambuchi, J. J., Liu, J., Yu, Y., & Feng, Y. (2017). Simultaneous algae-polluted water treatment and electricity generation using a biocathode-coupled electrocoagulation cell (bio-ECC). Journal of Hazardous Materials, 340, 104–112. `https://doi.org/10.1016/j.jhazmat.2017.06.055`

[39] OECD 2006. Guidelines for the Testing of Chemicals, Revised Proposal for a New Guideline 221, Lemna sp. Growth Inhibition Test

[40] Liu, S., Song, H., Li, X., & Yang, F. (2013). Power Generation Enhancement by Utilizing Plant Photosynthate in Microbial Fuel Cell Coupled Constructed Wetland System. International Journal of Photoenergy, 2013, 1–10. `https://doi.org/10.1155/2013/172010`

[41] Saz, C., Ture, C., Turker, O. C., & Yakar, A. (2018). Effect of vegetation type on treatment performance and bioelectric production of constructed wetland modules combined with microbial fuel cell (CW-MFC) treating synthetic wastewater. Environmental Science and Pollution Research, 25(9), 8777–8792. `https://doi.org/10.1007/s11356-018-1208-y`

[42] Zhao, Y., Collum, S., Phelan, M., Goodbody, T., Doherty, L., & Hu, Y. (2013). Preliminary investigation of constructed wetland incorporating microbial fuel

cell: Batch and continuous flow trials. Chemical Engineering Journal, 229, 364–370. `https://doi.org/10.1016/j.cej.2013.06.023`

Performance Analysis and Investment Cost Account Calculation of Building Integrated Photovoltaic Systems

Dilara Ayturk Tulukcu[1], Selcuk Sayin[2]
[1]dilaraytrk@gmail.com, Department of Architecture, Konya Technical University, Konya, Turkey
[2]ssayin@ktun.edu.tr, Department of Architecture, Konya Technical University, Konya, Turkey

Abstract

Population growth in developing countries, industrialization and rapid advancement of technology cause the increase of energy demand day by day. Fossil energy sources, which are frequently used to produce energy, are also rapidly depleting with this demand. In addition, the trend towards renewable energy sources is increasing in the context of the damage caused by the usage of fossil resources and the strategies developed by countries to supply their own energy demands. Buildings have a big role in total energy consumption and are among the important elements of environmental pollution caused by energy consumption. Solar energy is one of the important energy sources with its clean, local and renewable features. It can be used with today's photovoltaic system technologies, for building energy needs. The aim of the study is to determine the efficiency and cost analysis of a photovoltaic system which was integrated into an existing building. For this purpose, a glass factory building in Afyonkarahisar / Turkey was used. By integrating the photovoltaic system on the roof of this building, the system's energy analysis, initial investment cost and payback period were calculated. The performance analysis of the system was performed with PVsyst V6.7.8 simulation. On the roof, 5184 piece 265 V si-mono PV modules with a total area of 7014 m^2 and inverter with a total power of 1025 kWac were used. According to the results, it is concluded that the grid-connected photovoltaic system can generate 1723 MWh of energy annually, thus 64% of the annual energy need can be supply from the system and the efficiency of the system is 84.49%. It can repay the initial investment cost in about 7 years. It is appropriate to perform the study according to the net present value calculation.

Keywords: Solar energy, Photovoltaic system, PVsyst, Building integrated photovoltaics.

Introduction

Due to the technological, climatic and demographic changes, energy consumption increased rapidly in all over the world. Fossil energy sources are used widely for energy demand and they have significant impacts on the environment. Buildings have a big role in total energy consumption and are among the important elements of environmental pollution caused by fossil energy sources. This situation has brought to the agenda the concept of environment-friendly architecture. This concept is reflected in applications of the use of solar energy, which is one of the most important renewable energy sources and basis of our lives as heat, light and energy sources [1]. Solar energy can be used with today's photovoltaic system technologies, for building energy needs. Solar energy is more advantageous than other renewable energy sources with its clean energy, potential and ease of use [2]. Although, Turkey is in the sun belt, this solar energy potential is not efficiently and widely used.

There are many methods for generating usable energy from the sun. The widely used photovoltaic (PV) cell technology converts the energy carried by the Sun to the Earth through radiation into electrical energy [3]. Photovoltaic systems are beneficial in long-term use thanks to both environmentally friendly and easily accessible sources.

In the study, the photovoltaic system design of a factory in Afyonkarahisar/ TURKEY was carried out and the performance of the system was analysed PVsyst V6.7.8 simulation tool.

Photovoltaic Systems

Photovoltaic systems are mechanisms that directly generate electrical energy from solar radiation. It consists of many components including PV modules, inverters, batteries, charge control units, and other system components. PV modules are the most important part of the system. PV cells are made of semiconductor materials that generate electricity with solar energy.

There are many factors that need to be calculated and considered to learn the feasibility and performance of a PV system. These factors are; geographical location and solar radiation values of the location, the properties of the panels and inverters to be used, the shadowing of the radiation falling on the panels, the energy losses of the system, etc. For this reason, it is much more efficient and easy to make these calculations with simulation programs such as PVsyst.

Material and Method

In this study, a grid-connected photovoltaic system was designed with panel layouts which is added to the roof of a glass factory building in Afyonkarahisar/TURKEY. The study was carried out using the PVsyst V6.7.8 simulation tool and the performance evaluation of the system was made according to the simulation outputs of this tool. While calculating the cost, market research was conducted for the system requirements, net present value and payback and depreciation period were determined according to prices.

PVsyst Simulation Tool Method:

PVsyst program is used effectively in dimensioning, simulation and analysis of PV systems. With the help of this program, the daily or monthly total solar radiation data of the regions can be converted into hourly solar radiation data, and energy simulations can be performed by making system designs [5].

Afyonkarahisar is located on 37° 45° and 39° 17° north latitude, 29° 40° and 31° 43° east longitude and its altitude is 1034 meters. Afyonkarahisar's annual average temperature is 11.2 °C, the average temperature of the coldest month is 0.3 °C and the average temperature of the hottest month is 22.1 °C [6]. In Figure 1, the solar energy map of Afyonkarahisar with annual solar energy radiation of 1550-1650 kWh/m^2-year is given.

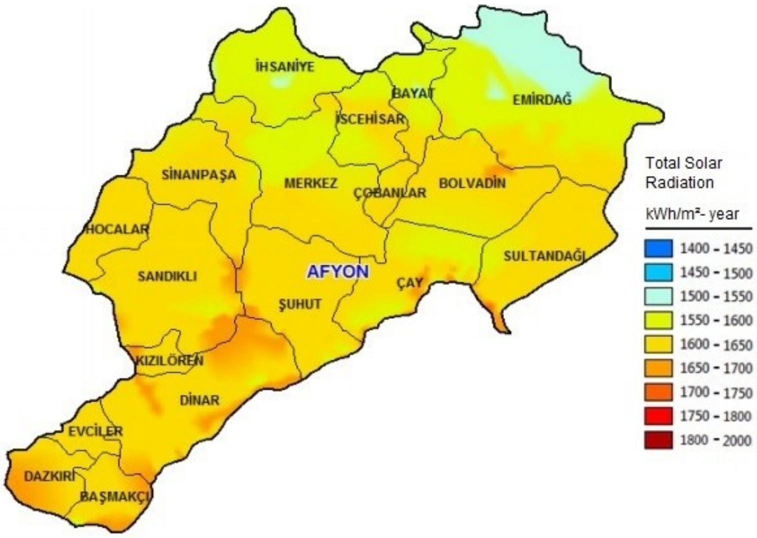

Figure 1: Afyonkarahisar solar energy map [8].

Afyonkarahisar monthly global radiation values and sunshine duration are shown in Table 1. Turkey average sunshine duration is 7.2 hours/day. When the chart is examined, sunbathing periods in May, June, July, August and September in Afyonkarahisar are higher than this value [10].

Table 1: Global radiation values and sunshine duration for Afyonkarahisar [8].

Month	Global Radiation Value (KWh/m^2-day)	Sunshine Duration (Hour)	Month	Global Radiation Value (KWh/m^2-day)	Sunshine Duration (Hour)
January	1.85	3.91	July	6.72	11,36
February	2.47	5.17	August	8.94	10.73
March	4.00	5.64	September	4.92	9.39
April	5.10	7.05	October	3.53	6.82
May	6.21	9.27	November	2.19	5.12
June	6.63	10.71	December	1.66	3.74

Average Sunshine Duration = 5,80

The factory located in Afyonkarahisar, are shown in Figure 2 and 3, and selected for system design has a short side of 65.5 meters, a long side of 120 meters, a height of 9.5 meters and a roof area of 7.860 square meters. The azimuth angle of the building is -17°. The slope of the roof, which is solved as a split gable roof, is 10%, the slope angle is 6 ° and the slope is in the east-west direction. Roof surface azimuth angles are -107° and 73°. Data such as the location of the building and its azimuth angle were obtained using Google Earth Pro program.

Figure 2: Location of glass factory.

Figure 3: Facade of glass factory.

Cost Calculation Method:

Average values method was used while calculating the investment cost. Market research has been made according to the properties of the selected system elements and the average prices of the products have been determined. With reference to other PV panel applications, installation, transportation, maintenance-repair and cabling costs were calculated on average as a result of interviews with a local PV panel practitioner.

Then, it was evaluated whether the investment is suitable or not according to the Net Present Value (NPV) calculation method. The net present value of a project is the sum of the net cash flows during its economic life, reduced to present value at a predetermined discount rate [7]. The net present value method is used to evaluate existing or potential investments.

Results and Discussion

In this section, the PV system simulation is realized with the methods which are explained in Section 3. The results of the simulation are presented in addition with the cost calculations and they are discussed.

System design realization with PVsyst simulation tool:

A grid-connected system design is simulated in the PVsyst program. The area of the building was determined and the photovoltaic panel and inverter were selected according to optimum values depending on factors such as climate, cost, profit, payback and installed power. In this study, a monocrystalline silicon cell photovoltaic panel of 1638 x 826 x 40 mm with a unit norm power of 265 W was chosen. A circuit with a power output of 2.5 kWac, made by Canadian Solar brand, was selected as the inverter. Since the panels are integrated into a pitched roof, the current roof inclination angle of 6 ° has been entered into the program.

Roof dimensions and angles determined in the PVsyst simulation tool, modelled as shown in Figure 4.

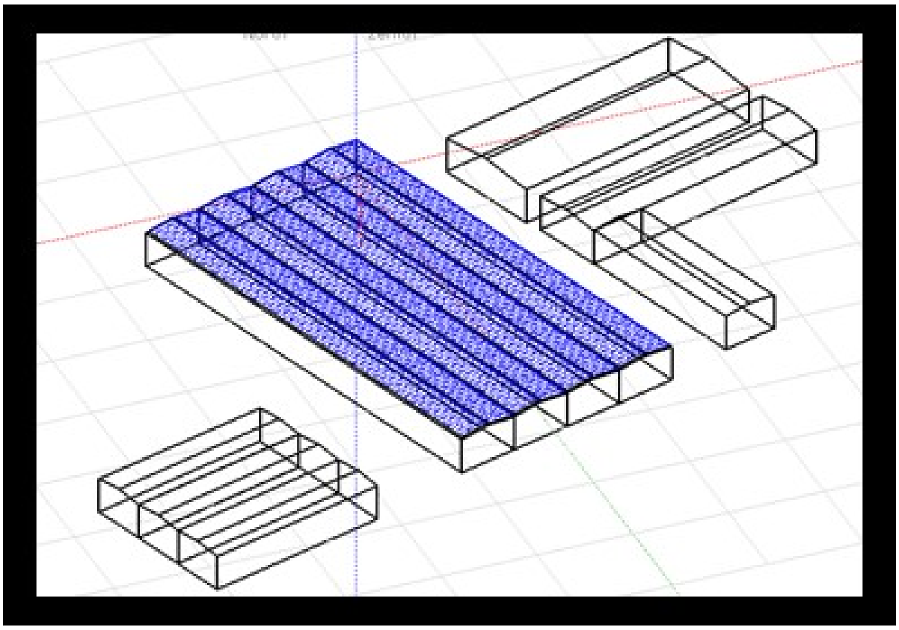

Figure 4: 3D Modelling done in PVsyst simulation tool.

According to the design, 5184 panels in total were placed on the roof (Table 2).

Table 2: Calculation of PV panels.

Total Area = 7860 m^2
Usable Area = 7014 m^2
1 PV Module Area= 1.35 m^2 (1638 x 0.826)
7014/1.35=5184 Panels

The installed power of the planned mechanism is 1374 kWp. The inverters have a total power of 1025 kWac, 513 kWac for each direction. The annual amount of energy supplied to the grid by the system has some energy losses due to shadow factor, panel efficiency, temperature and inverter lose. The annual energy production decrease to 1723 MWh/year, although the amount of energy produced is 1972 MWh/year. Figure 5 shows the annual loss and gain diagram obtained from the PVsyst program, showing where all the losses are coming from.

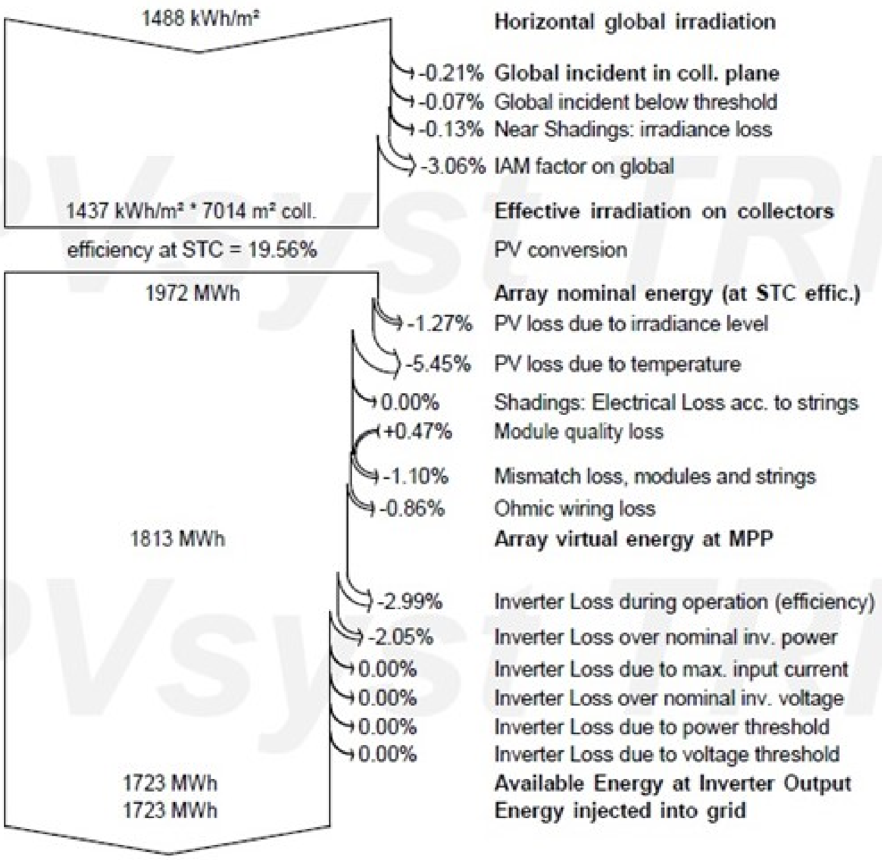

Figure 5: System loss diagram derived from PVsyst tool.

Due to the temperature increase, the energy efficiency of the PV modules decreases over a certain value. As seen in the Figure 6, system performance decreases from May to September. However, energy production is higher during the warmer months than the colder months. According to the simulation result report, the average performance rate of the system is 84.49%.

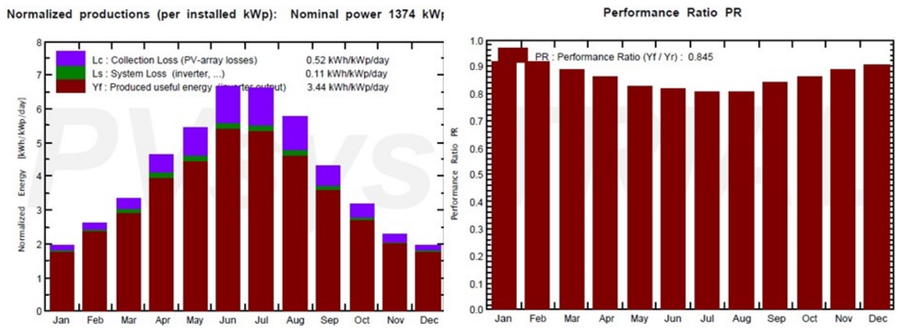

Figure 6: System performance / performance ratios by months obtained from the PVsyst tool.

Cost Calculation:

According to the calculation method mentioned in section 3, the costs shown in the Table 3 have emerged.

Table 3: System Cost. Table is derived from Guven, Kilic's (2018) study [5].

System Cost	
One Solar Panel Price	125$
Total Panel Price	648000$
Invertor Price	5150$
Construction	200$
Setup-Transport	250$
Wiring	290$
Other (Repair-Maintenance)	1100$
Total	654950$

Total Cost according to the table 3 is \$654950. In this case, payback period account is calculated with the ratio of the total cost to the annual earnings (Equation 1). The exchange rate has been accepted as 6.85 TL according to its value on 04.07.2020. The unit price of electricity was taken as 0.36 TL based on the invoice information obtained from the owner of the factory. Canadian Solar panel and inverter prices are taken from "Sunwatt" solar panel manufacturer [10].

1 year energy production= 1723 MWh. 1 MWh=1000 kWh, 1kWh=0,36 TL
1723000 x 0.36 = 620280 TL. (The gain of the system in 1 year) (1)
654950 x 6.85 = 4486408 TL. (Cost in TL)
Payback Period = 4486408 / 620280 =7.23 year (Total cost/ Annual gain)

According to the payback period calculation, the initial investment cost of the PV panel system pays back approximately within 7 years. 2019 electricity consumption of the amount of electricity consumed by the factory in one year is 2668103 kWh. After calculating the investment cost and payback period of the system, it has been evaluated whether it is suitable for application according to NPV calculation (Equation 2). NPV account formula is shown below. In the formula, the economic life of the system is 25 years and the interest rate is 10%.

NPV=R1/(1+i)1+R2/(1+i)2+R3/(1+i)3...Rn/(1+i)n-C (2)
NPV=620280/(1+0.1)+ 620280/(1+0.1)2+...620280/(1+0.1)25 - 4486408 >0
R=Cash flow, C=Cost of capital n=Economic life, i=Interest rate
According to the NPV method is positive, the system is considered applicable.

Conclusion

In this study, the situation of meeting the electricity need of a factory in Afyonkarahisar with photovoltaic systems was discussed. It is aimed to calculate the amount of energy that can be produced from the system and the system performance in the simulation tool. For this purpose, the PVsyst V6.7.8 simulation tool was chosen and the performance analysis of the designed photovoltaic system was made.

It was observed that the global irradiation amount at the location reached the lowest effective irradiance value on the panel surface in January, and the highest effective irradiance value in July.

It is predicted that the annual total energy amount that can be transferred to the network after deducting the system losses will be 1723 MWh. In this case, 64% of the annual energy consumed can be met from the PV system.

According to the electricity bill, it has been calculated that the electricity consumption unit price is 0.36 TL / kWh and the system will gain approximately 620,280 TL in the annual electricity bill.

By taking the methods used in this study as an example, energy generation estimates of a PV system to be designed can be made. Evaluations of the system can be made as described in this study and the most appropriate and profitable designs can be created before the system is implemented. If the efforts are increased in order to benefit from the renewable energy source, the sun, and if photovoltaic systems become widespread for electricity generation, the damages caused by fossil fuels will be reduced.

References

[1] Knowles, R. L. (2003). The solar envelope: its meaning for energy and buildings. Energy and Buildings, 35(1), 15–25. `https://doi.org/10.1016/s0378-7788(02)00076-2`

[2] Freitas, S., Catita, C., Redweik, P., & Brito, M. C. (2015). Modelling solar potential in the urban environment: State-of-the-art review. Renewable and Sustainable Energy Reviews, 41, 915–931. `https://doi.org/10.1016/j.rser.2014.08.060`

[3] Aksangor, N. N., Martin, K., & Boran, K. (2019, April). PVsyst Simulasyon Araci Kullanarak Ankara'da Fotovoltaik Gunes Sistemlerin Performans Analizi. SETSCI Conference Proceedings, 217–220.

[4] Sayın, S. (2006). Yenilenebilir Enerjinin Ulkemiz Yapi Sektorunde Kullaniminin Onemi ve Yapilarda Gunes Enerjisinden Yararlanma Olanaklari, Selcuk University, Konya, Turkey.

[5] Guven, F., Kilic, S. (2018). Armutlu Devlet Hastanesinin Enerji Ihtiyacinin Gunes Enerjisiyle Karsilanmasi ve Maliyet Analizi. 3th International Conference on Multidisciplinary Sciences, 131-140.

[6] Cunkas, M., Demirkol, Z. (2014). Afyonkarahisar Ili Yenilenebilir Enerji Potansiyeli, Selcuk Universitesi Muhendislik, Bilim ve Teknoloji Dergisi.

[7] Demirbugan, A. (2008). Yatirim Projelerinin Degerlendirilmesinde Net Bugunku Deger(Nbd) ve Ic Karlilik Orani(Iko) Yontemlerinin Karsilastirilmasi. Afyon Kocatepe Universitesi, I.I.B.F. Dergisi.

[8] `http://www.yegm.gov.tr/anasayfa.aspx` [Access date: 09 June 2020]

[9] `http://www.yegm.gov.tr/MyCalculator/` [Access date: 09 June 2020]

[10] `https://sunwatts.com/2-5kw-solar-kit-canadian-320-enphase-micro-inverter/` [Access date: 03 July 2020]

Preparation of Effective Ni-Ti-B Triple Catalysts for Hydrolysis Reaction of Sodium Boron Hydride and Investigation of Kinetic Properties

Julide Hazal Turkcan[1], Kadir Sagir[2], Oguz Kaan Ozdemir[3]
[1]j.hazalturkcan@gmail.com, Department of Metallurgical and Materials Engineering,
Yildiz Technical University, Istanbul, Turkey
[2]kadir.sagir@tau.edu.tr, Department of Materials Science and Technology,
Turkish-German University, Istanbul, Turkey
[3]kozdemir@yildiz.edu.tr , Department of Metallurgical and Materials Engineering,
Yildiz Technical University, Istanbul, Turkey

Abstract

Hydrogen, which has high efficiency value, is a renewable and clean energy source. Due to its high hydrogen content (10.8 wt%), sodium boron hydride ($NaBH_4$) is one of the compounds that can be used as hydrogen storage medium. In the mentioned study, Ni-Ti-B ternary catalysts were developed by using chemical reduction method, for hydrolysis reaction of the $NaBH_4$. Moreover, the catalytic performances were investigated according to the effect of Ti doping into the Ni-B catalyst structure by performing the hydrogen releasing test. Additionally, the elemental analyses were obtained by performing SEM-EDS characterization method.

Keywords: Hydrogen Production, Hydrogen Storage, Sodium Borohydride, Ternary Systems, Ni-Ti-B Catalyst.

Introduction

Fossil fuels, which are used more than other energy sources, have limited resources and cause negative environmental effects [1]. For this reason, interest in fuel cells, which are renewable and efficient energy sources, is increasing. Fuel cells in which hydrogen is used as fuel have a high percentage of energy conversion [2]. As a clean and renewable energy source, hydrogen can be stored in methods such as liquefied, compressed in pressure tubes and chemical bonded [3, 4]. Chemical hydride compounds, which are safer and more efficient than other storage methods, are preferred as hydrogen sources. Due to its high hydrogen content (10.8 wt%), $NaBH_4$ is particularly suitable for use in portable proton exchange membrane fuel cells (PEMFC). In addition, the catalyst part involved in the reduction and oxidation reactions that take place in the PEM fuel cells is an important component that affects the efficiency [5, 6]. Although noble elements such as platinum (Pt) with high catalytic activity, are preferred in the PEMFC, their use is limited by high cost. [7]. Research over time has focused on relatively cheaper transition metals, such as cobalt (Co), nickel (Ni) and iron (Fe), that provide high catalytic activity [8, 9]. In this study, Ni-Ti-B triple catalysts were prepared by chemically reduced Ni and Ti cations and its catalytic properties were investigated.

Materials And Methods

Synthesis of Ni-B and Ni-Ti-B Triple Catalysts for Hydrolysis Reaction of $NaBH_4$

In experimental studies, Ni-B and Ti-doped Ni-Ti-B catalyst have been developed to obtain the pure hydrogen required for the PEM type fuel cell by the hydrolysis reaction of $NaBH_4$, which has a high hydrogen storage capacity. The "Chemical Reduction Method" was used for the preparation of the catalysts. Firstly; 28 ml of $NiCl_2.6H_2O$ (Sigma Aldrich, 97%) was mixed with distilled water in a beaker. For the preparation of the Ni-Ti-B ternary catalyst 3 ml and 6 ml of titanium chloride ($TiCl_3$, Sigma Aldrich, 99%) and EDTA (Merck) were also added during this stage. The parameters for the synthesis of the Ni-B and Ni-Ti-B Triple Catalysts, were given in Table 1.

After that, the beaker was immersed in a water bath (Heidolph, Small Chiller) with a temperature that adjusted to 5 °C under the stirring conditions. When the desired (8-9 °C) temperature was obtained, the reduction process was started by using a reducing agent that contains sufficient amount of $NaBH_4$ (Merck, 98%) and distilled water. At the end of the process "the black precipitate" was obtained.

The centrifugation process (Nuve, NF800) at 8000 rpm for 5 minutes was applied and repeated for all solutions. Then, the precipitated catalysts washed twice respectively with distilled water and ethanol, dried in a vacuum oven (Nuve, NF800) at 105 °C for 2 hours and grinding process was applied by using an agate mortar.

Table 1: Parameters for the preparation of Ni-B and Ni-Ti-B triple catalysts.

Catalyst Name	Contents	Reducing Agent	Fuel
N1	$NiCl_2$ Distilled Water	$NaBH_4$ Distilled Water	1g NaOH (5wt%) 1g $NaBH_4$ (5 wt%)
T1	$NiCl_2$ (28 ml) $TiCl_3$ (3 ml) Distilled Water EDTA	$NaBH_4$ Distilled Water	1g NaOH (5wt%) 1g $NaBH_4$ (5 wt%)
T2	$NiCl_2$ (28 ml) $TiCl_3$ (6 ml) Distilled Water EDTA	$NaBH_4$ Distilled Water	1g NaOH (5wt%) 1g $NaBH_4$ (5 wt%)

Hydrogen Releasing Test

Within the scope of the characterization studies, the amount of the hydrogen that produced was measured. During the process the magnetic stirring kept constant at 600 rpm and a 250 ml reactor was placed in a water bath (JSR, JSIB-100T) which had the temperature adjusted to 65 °C. Then, the 20 mg of the catalyst was added into the reactor and fuel, which contains $NaBH_4$ (5 wt%) and NaOH (5 wt%), was added quickly. The volume of the hydrogen gas released during the reaction was measured via the decreasing of the water level in the gas burner, after passing through the wash bottle. During these experiments, both the total reaction time and the hydrogen generation time were measured separately. The amount of the hydrogen produced every 1 minute was noted and graphs of hydrogen amount produced by volume (ml) versus time were created.

Results and Discussion

The Ni-B binary and Ni-Ti-B triple catalysts that contains 28 ml/0,02 M $NiCl_2$ and 80 ml distilled water and 3 ml-6 ml of $TiCl_3$ were tested by using alkaline $NaBH_4$ solution ($NaBH_4$ (5 wt%) and NaOH (5 wt%)) at 338 K. Hydrogen generation rate (HGR) and efficiency of catalysts reaction were given in Table 2 and the released hydrogen volume (ml) as a function of reaction time for N1 coded Ni-B catalyst was given in Figure 1.

Table 2: Determination of total reaction time and efficiency (%) of catalysts.

Catalyst Name	Reaction Time(s)	Volume of H_2 (ml)	Efficiency (%)
N1	1500	832	59.33
T1	4260	925	77
T2	4560	875	73

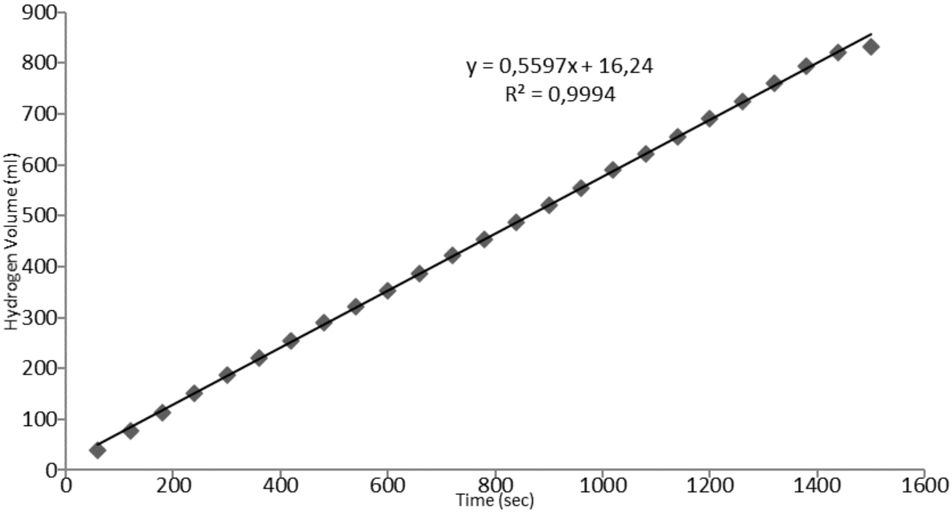

Figure 1: Released hydrogen volume (ml) as a function of reaction time for N1.

From the Figure 1 it can be predicted that the hydrogen generation starts instantly after the addition of the fuel. Besides, the hydrogen generation amount is almost linearly (R^2=0,9994) that indicates the constant hydrogen generation and stability of the catalytic activity.

The synthesis of the Ni-Ti-B triple catalysts were done by using synchronous chemical reduction of nickel and titanium metals. The EDTA was used as a complexing agent in order to bring the reduction potentials of the Ni and Ti cations closer to each other. Figure 2 shows the EDS analyses of the Ni-Ti-B ternary system. As given in the spectrum the nickel and titanium were obtained without presence of oxygen and sulphur and also, oxidizing.

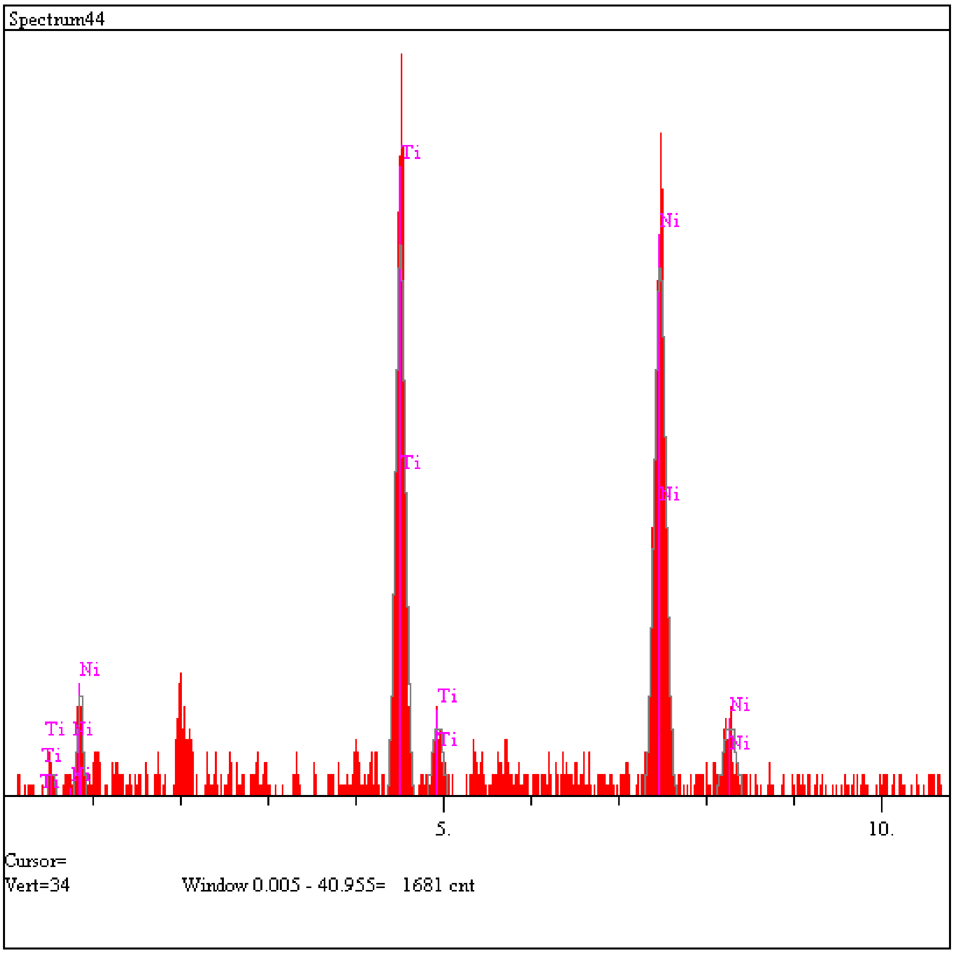

Figure 2: EDS spectra of Ni-Ti-B catalysts.

Figure 3 shows the released hydrogen volume (ml) as a function of reaction time for both Ni-B binary and Ni-Ti-B ternary catalysts.

From the Figure 3 it can be evaluated that, titanium doped catalysts decrease the hydrogen production rate per unit time, whereas the efficiency (amount of hydrogen produced) of the catalysts increase. Also, the titanium reinforced catalysts have longer durability and hydrogen production rate. The Ni-B catalyst has a shorter durability, but the amount of hydrogen produced per unit time is higher than the titanium-added catalysts.

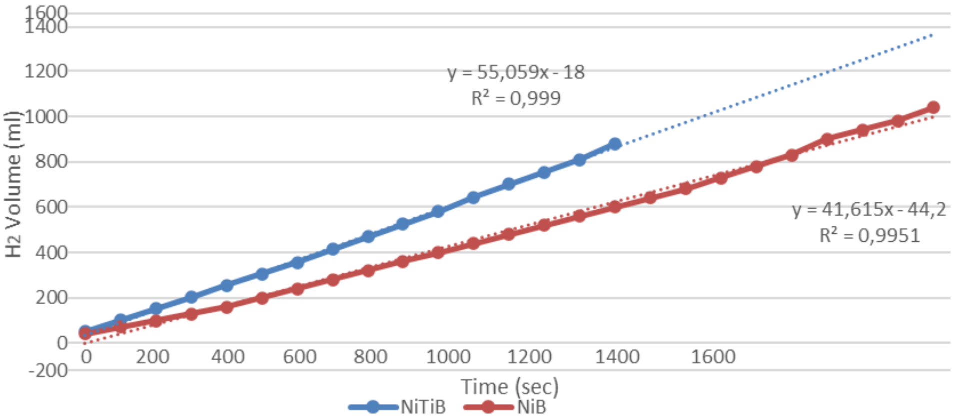

Figure 3: Released hydrogen volume (ml) as a function of reaction time of N1, T1 and T2.

Conclusions

Within the scope of the mentioned study, Ni-Ti-B ternary systems were prepared with doping of titanium into the catalyst structure by chemical reduction method for hydrolysis reaction of alkaline $NaBH_4$ solutions. From the results it can be concluded that addition of Ti increases both the catalytic activity and efficiency. Also, the SEM-EDS spectrums prove that, without presence of undesired elemental peaks, reduction of Ni and Ti cations were completed. Consequently, the Ti-doped catalysts that have higher hydrogen production rate, efficiency and durability, are promising for the future investigations.

Acknowledgements

This research was supported by Scientific and Technological Research Council of Türkiye (TUBITAK) under the contract 119M756.

References

[1] Yuan, X., Song, C., Wang, H., & Zhang, J. (2014). Electrochemical Impedance Spectroscopy in PEM Fuel Cells: Fundamentals and Applications (2009th ed.). Springer.

[2] Chalk, S. G., & Miller, J. F. (2006). Key challenges and recent progress in batteries, fuel cells, and hydrogen storage for clean energy systems. Journal of Power Sources, 159(1), 73–80. `https://doi.org/10.1016/j.jpowsour.2006.04.058`

[3] Barthelemy, H., Weber, M., & Barbier, F. (2017). Hydrogen storage: Recent improvements and industrial perspectives. International Journal of Hydrogen Energy, 42(11), 7254–7262. `https://doi.org/10.1016/j.ijhydene.2016.03.178`

[4] Durbin, D. J., & Malardier-Jugroot, C. (2013). Review of hydrogen storage techniques for on board vehicle applications. International Journal of Hydrogen Energy, 38(34), 14595–14617. `https://doi.org/10.1016/j.ijhydene.2013.07.058`

[5] Chen, Y., & Kim, H. (2010). Preparation and application of sodium borohydride composites for portable hydrogen production. Energy, 35(2), 960–963. `https://doi.org/10.1016/j.energy.2009.06.053`

[6] Kim, T. (2012). Fully-integrated micro PEM fuel cell system with NaBH4 hydrogen generator. International Journal of Hydrogen Energy, 37(3), 2440–2446. `https://doi.org/10.1016/j.ijhydene.2011.09.150`

[7] Zhang, L., Zhang, J., Wilkinson, D. P., & Wang, H. (2006). Progress in preparation of non-noble electrocatalysts for PEM fuel cell reactions. Journal of Power Sources, 156(2), 171–182. `https://doi.org/10.1016/j.jpowsour.2005.05.069`

[8] Faur Ghenciu, A. (2002). Review of fuel processing catalysts for hydrogen production in PEM fuel cell systems. Current Opinion in Solid State and Materials Science, 6(5), 389–399. `https://doi.org/10.1016/s1359-0286(02)00108-0`

[9] Ou, L. (2014). The origin of enhanced electrocatalytic activity of Pt–M (M=Fe, Co, Ni, Cu, and W) alloys in PEM fuel cell cathodes: A DFT computational study. Computational and Theoretical Chemistry, 1048, 69–76. `https://doi.org/10.1016/j.comptc.2014.09.017`

Potential Applications and Characterization of Rice Husk

Nazli Turkten[1], Zekiye Cinar[2]
[1]nazli.turkten@ahievran.edu.tr, Department of Chemistry, Kirsehir Ahi Evran University, Kirsehir, Turkey & Department of Chemistry, Yildiz Technical University, Istanbul, Turkey
[2]cinarz@yildiz.edu.tr, Department of Chemistry, Yildiz Technical University, Istanbul, Turkey

Abstract

Rice husk (RH) is an agricultural waste available widely in rice producing countries worldwide. In recent years, this low-cost and environmentally friendly waste has been commonly used as a biomass for an alternative source of energy generation. Moreover, the ash product formed by the combustion of RH has potential applications in various industries. In this study, the structure of the RH was identified by using FTIR, SEM, XRD, XPS, and DTA-TGA techniques. As well, the characterization of rice husk ash (RHA) was studied. The functional groups of RH and RHA were determined by FTIR. The organic part of RH was composed of cellulose, lignin, and hemicellulose. FTIR and DTA-TGA results indicated that lignin is thermally more stable than cellulose and hemicellulose. The characteristic of amorphous silica band was detected in XRD diffractogram of RH.

Keywords: Biomass, Rice Husk, Rice Husk Ash, XRD.

Introduction

The global energy demand is increased due to the development of industrialization and enhancement on the population growth. In this concern, biomass is an important alternative energy with availability of various sources such as rice husk (RH), rice straw, sugarcane, and bagasse [1, 2]. RH is one of the most consumed food worldwide and mainly used with sugarcane as biomass [1, 3]. Hence, evaluating this low-cost agricultural waste has been attracted a great interest especially RH production countries such as Thailand [4]. RH is used to produce steam for generator turbine to generate power. The widely used two energy conversion technologies for energy production are combustion heating and direct combustion power generation. It is known that approximately one ton of RH can produce 800 kW h of electric power. In addition to energy production from RH, there are available potential applications such as biochar preparation, synthesis of silica, and silicon materials manufacture, etc. Moreover, rice husk ash (RHA) is used in power plants. Amorph silica obtained from RHA is used in concrete production while crystalline silica used in steel industry as an insulator [1, 2, 4].

RH is the outer part of the paddy grain achieved by milling process. RH consists of 25% mass of the rice grain. The major components of RH are cellulose, hemicellulose, lignin, and silica. Besides, soluble and moisture can be found. These components and amounts can vary for different RH samples due to the parameters such as geographical and climate conditions, paddy year and soil chemistry. Addition to these parameters the ignition conditions affects RHA production [1, 5–7]. White RHA is obtained by a controlled combustion of RH in air. This white ash contains almost pure silica and it is an important silica source for commercial use. The pyrolysis of RH results a black RHA containing carbon and silica with high porosity. This ash can be used for the synthesis of silicon carbide and silicon nitride [5].

The aim of this study was to identify the structure of RH which was obtained from the Anatolian part of Turkey. Besides, the structure of RHA was also investigated.

Materials And Methods

Materials. Prior to use, RH was ground and sieved. Afterwards, RH washed with distilled water and then dried at 105 °C in an air oven for 24 h. RHA was calcined in a muffle furnace at three different calcination temperatures (350 °C, 500 °C, and 600 °C) for 3h.

Characterization Methods. Fourier transform infrared (FTIR) measurements were perfomed by Perkin Elmer Spectrum One spectrometer. SEM-FEG PhilipsXL-30 instrument was obtained for the micrographs of RH and RHA samples. The X–ray powder diffraction (XRD) patterns were recorded on a Rigaku-D/MAX-Ultima diffraction spectroscope. The thermogravimetric analysis of RH samples was achieved on a EXSTAR TG/DTA 6300 thermal analyser. The heating rate was 10 K min^{-1} in nitrogen atmosphere. X-ray photoelectron spectroscopy (XPS) measurements were carried out by using a Thermo Scientific K-Alpha X-ray Photoelectron Spectrometer.

Results and Discussion

FTIR Spectroscopy

FTIR spectra of the RH at room temperature and RHA samples calcined at 350 °C, 500 °C, and 600 °C for 3h are displayed in Figure 1.

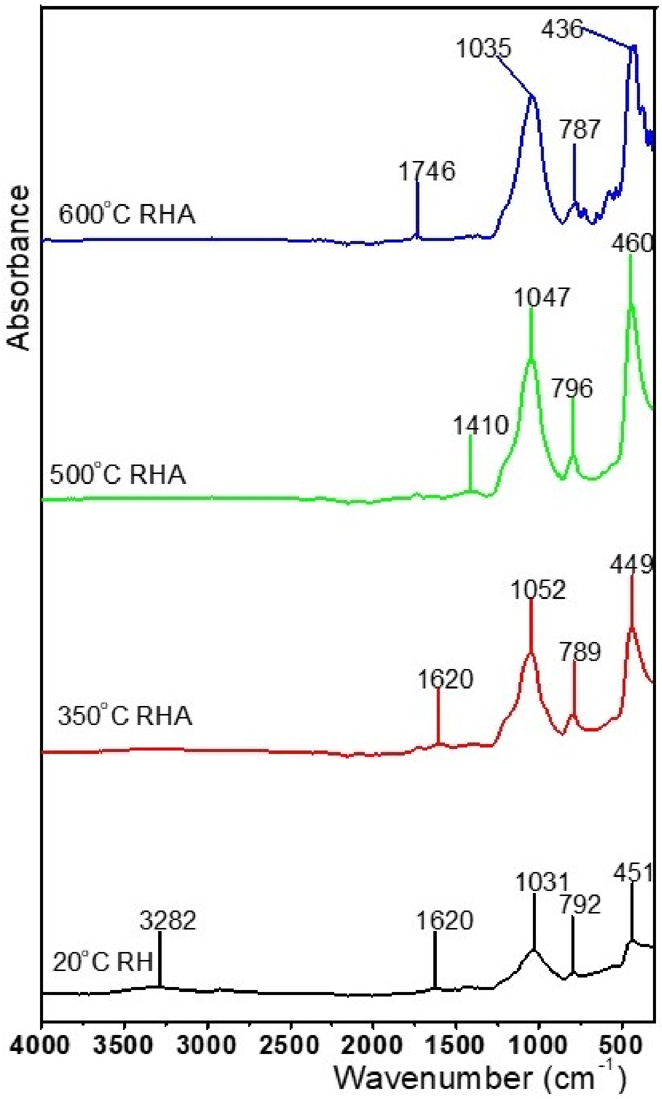

Figure 1: FTIR spectra of RH and RHA samples.

In the RH spectrum, a wide peak centred at 3282 cm^{-1} corresponds to the stretching vibration of intermolecular hydrogen bonded –OH groups in cellulose, hemicellulose and lignin and the stretching vibrations of –OH bonds in adsorbed water [5,8]. The peak located at 1735 cm^{-1} is assigned to C=O stretching modes in ketones, aldehydes and lactones. The peaks at 1420 and 1620 cm^{-1} are related to CH_2 and aromatic C=C stretching vibrations respectively. The intensities of these peaks are decreased with increasing temperature and completely disappeared at 600 °C. The reason can be explained by the decomposition of the $–CH_2$ and $–CH_3$ groups in cellulose and hemicellulose in an earlier stage compared to the aromatics in lignin [9]. The strong peak at 1031 cm^{-1} belongs to stretching Si-O-Si bond. This peak shifts to a higher wave number ($\approx$ 1050 cm^{-1}) with increasing temperature in RHA spectra due to the widening of O-Si-O angle and this may result a decrease in the densification of the structure. [9,10]. The two peaks at 792 cm^{-1} and 451cm^{-1} correspond to the stretching vibration of Si-H bond [5,10].

As can been seen from Figure 1, the intensity of these peaks increases at higher calcination temperatures indicating the silica amount is enhanced with increasing temperature in RHA [11].

Thermal Analysis

In Figure 2, TG and DTA curves of RH are presented. The first stage with 6% weight loss with an endothermic peak at around 100 °C may be attributed to dehydration of adsorbed water. The second stage is followed by a great weight loss ≈50% with a broad exothermic peak in the temperature range 240-360 °C at ≈305 °C indicating the thermal decomposition of cellulose and hemicellulose with the weight loss due to volatiles escaping from RH. The third stage is a weight loss of ≈20% with an exothermic peak in the temperature range 360-450 °C centered at ≈410 °C signifying the thermal decomposition of lignin. This result supports the FTIR findings and demonstrates lignin is thermally more stable than cellulose and hemicellulose.

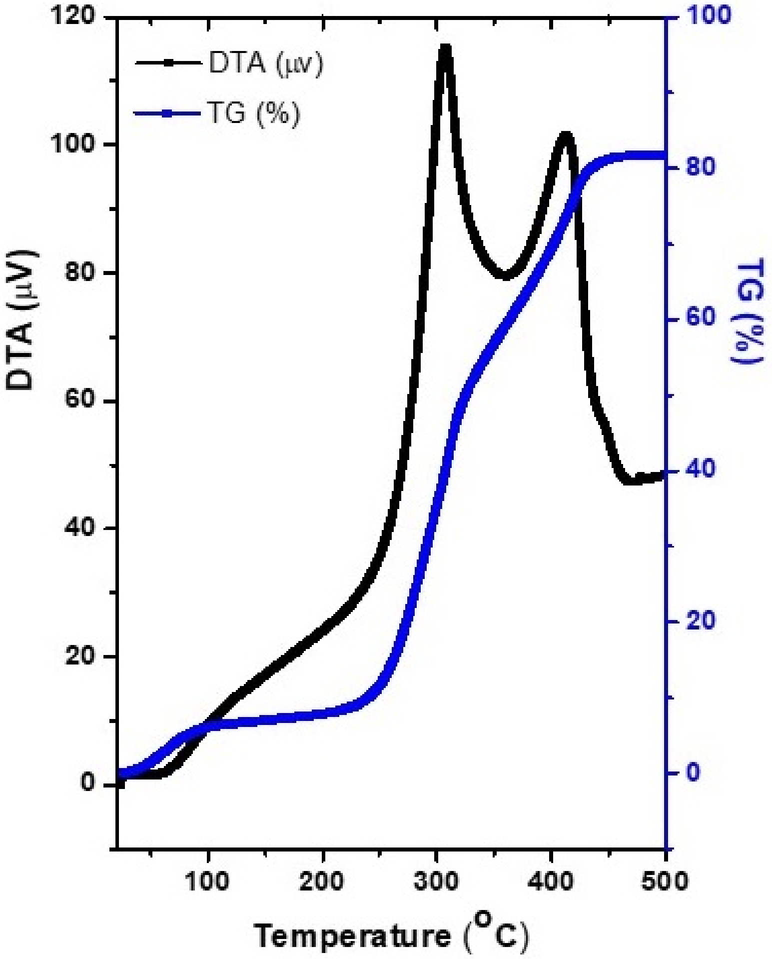

Figure 2: TG and DTA curves of RH.

XRD Spectroscopy

Figure 3 demonstrates XRD diffractograms of the RH at room temperature and RHA samples calcined at 350 °C, 500 °C, and 600 °C for 3h. The diffractogram of the RH shows a wide band in the region 15–30° with a maximum ≈22° indicating the characteristics peak of amorphous silica. In RHA diffractograms this peak shift to a lower angle due the broadening of the amorphous structure. This result is consistent with the FTIR results.

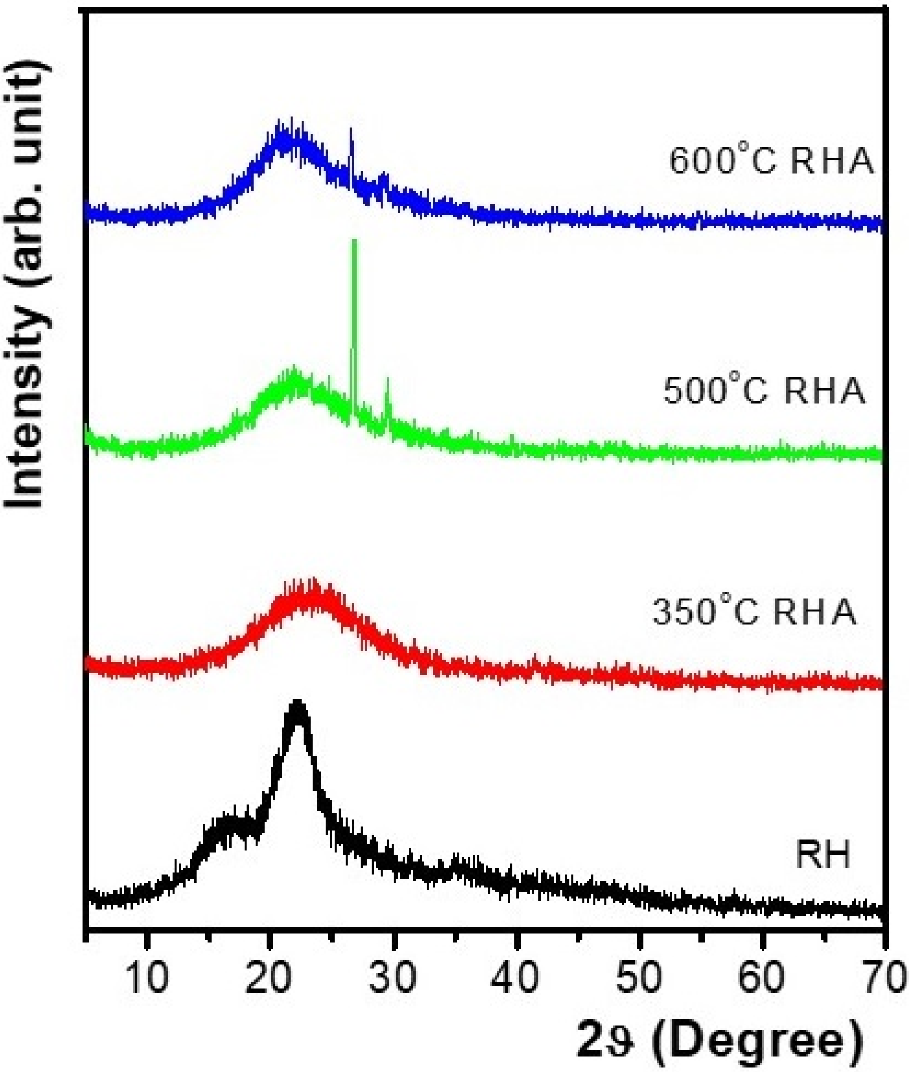

Figure 3: XRD diffractograms of RH and RHA samples.

Morphology

ESEM micrographs of RH and RHA calcined at 350 °C for 3h at are presented in Figure 4. The outer layer of RH reveals like a corn cob with silica tubes while the inner consists of a fibrous structure. In the ESEM micrograph of RHA, the structure of RH is almost protected with a slight morphological deformation as a result of thermal decomposition [9].

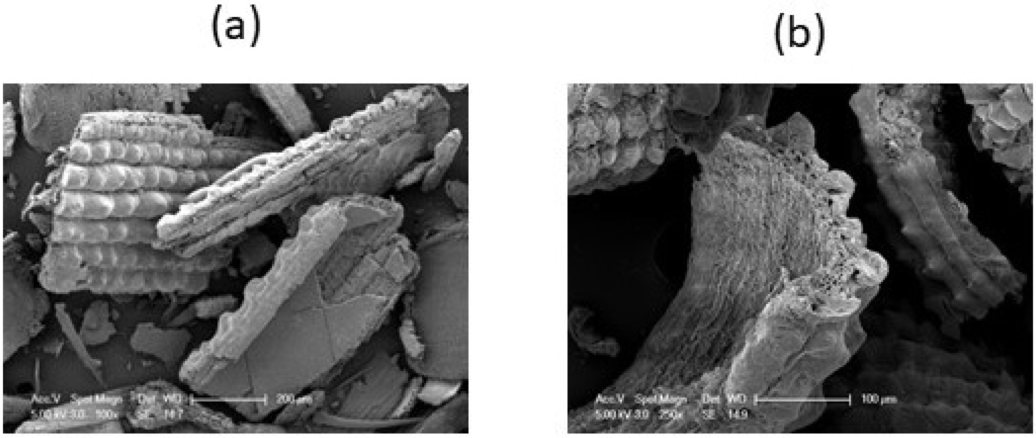

Figure 4: SEM micrographs of (a) RH and (b) RHA samples.

XPS

XPS spectra of the RH sample is presented in Figure 5. The spectra contain C1s region ≈285 eV, N1s region ≈400 eV, S2p region ≈155 eV and Si 2p region ≈102 eV [12–14]. The two peaks located at ≈284 and 285 eV are related to the 1s electrons of carbon in cellulose and hemicellulose [15, 16]. The peak at 102.72 eV is assigned to the photo-splitting electrons $Si^{4+}2p_{3/2}$ signifying that silisium is found in the form of Si^{4+} as in silicates [14].

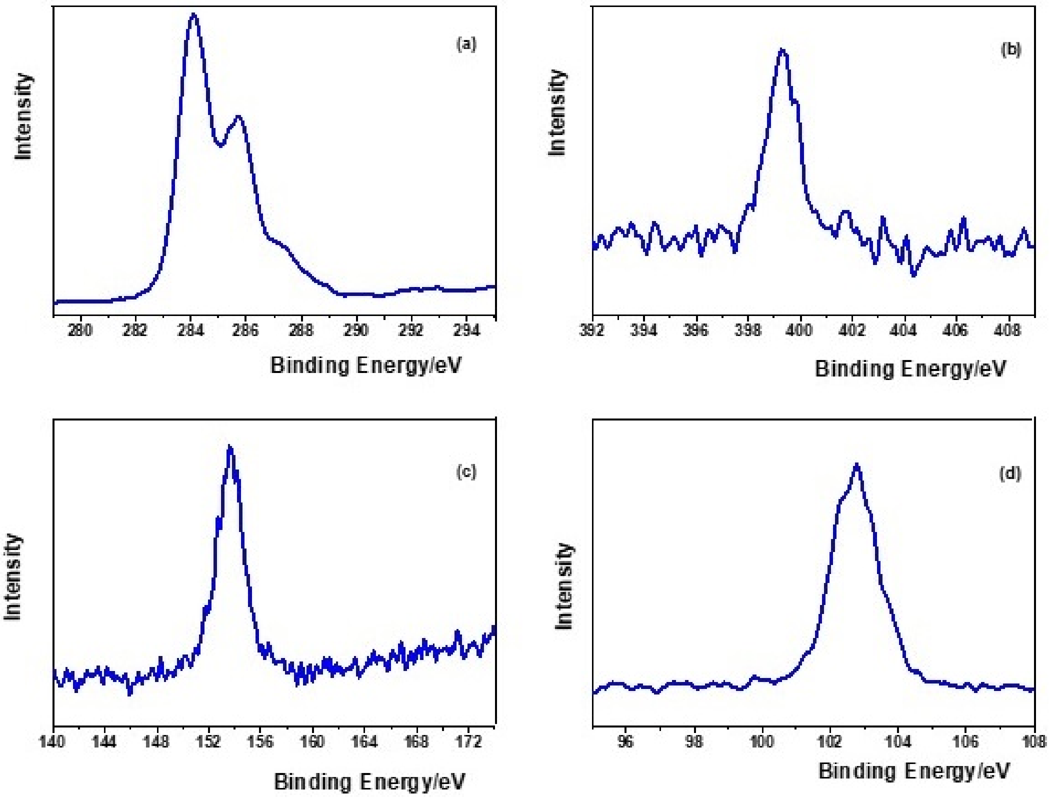

Figure 5: XPS spectra of RH sample (a) C1s, (b) N1s, (c) S2p (d) Si2p.

Conclusions

The structure of the RH was characterized by using FTIR, SEM, XRD, XPS, and DTA-TGA methods. Moreover, the structural and morphological changes of RHA were also investigated. FTIR results revealed that the presence of silica amount was higher with higher calcination temperatures. Amorphous silica peak was observed in RH while this peak shifted to a lower angle in RHA samples. The corn-cob like structure of RH was sligtly deformed with calcination process.

References

[1] Pode, R. (2016). Potential applications of rice husk ash waste from rice husk biomass power plant. Renewable and Sustainable Energy Reviews, 53, 1468–1485. `https://doi.org/10.1016/j.rser.2015.09.051`

[2] Lim, J. S., Abdul Manan, Z., Wan Alwi, S. R., & Hashim, H. (2012). A review on utilisation of biomass from rice industry as a source of renewable energy. Renewable and Sustainable Energy Reviews, 16(5), 3084–3094. `https://doi.org/10.1016/j.rser.2012.02.051`

[3] Fernandes, I. J., Calheiro, D., Kieling, A. G., Moraes, C. A. M., Rocha, T. L. A. C., Brehm, F. A., & Modolo, R. C. E. (2016). Characterization of rice husk ash produced using different biomass combustion techniques for energy. Fuel, 165, 351–359. `https://doi.org/10.1016/j.fuel.2015.10.086`

[4] Prasara-A, J., & Gheewala, S. H. (2017). Sustainable utilization of rice husk ash from power plants: A review. Journal of Cleaner Production, 167, 1020–1028. `https://doi.org/10.1016/j.jclepro.2016.11.042`

[5] Genieva, S. D., Turmanova, S. C., Dimitrova, A. S., & Vlaev, L. T. (2008). Characterization of rice husks and the products of its thermal degradation in air or nitrogen atmosphere. Journal of Thermal Analysis and Calorimetry, 93(2), 387–396. `https://doi.org/10.1007/s10973-007-8429-5`

[6] Stefani, P. M., Garcia, D., Lopez, J., & Jimenez, A. (2005). Thermogravimetric analysis of composites obtained from sintering of rice husk-scrap tire mixtures. Journal of Thermal Analysis and Calorimetry, 81(2), 315–320. `https://doi.org/10.1007/s10973-005-0785-4`

[7] Moayedi, H., Aghel, B., Abdullahi, M. M., Nguyen, H., & Safuan A Rashid, A. (2019). Applications of rice husk ash as green and sustainable biomass. Journal of Cleaner Production, 237, 117851. `https://doi.org/10.1016/j.jclepro.2019.117851`

[8] Daifullah, A. A. M., Girgis, B. S., & Gad, H. M. H. (2003). Utilization of agro-residues (rice husk) in small waste water treatment plans. Materials Letters, 57(11), 1723–1731. `https://doi.org/10.1016/s0167-577x(02)01058-3`

[9] Yuzer, N., Cinar, Z., Akoz, F., Biricik, H., Yalcin Gurkan, Y., Kabay, N., & Kizilkanat, A. B. (2013). Influence of raw rice husk addition on structure and properties of concrete. Construction and Building Materials, 44, 54–62. `https://doi.org/10.1016/j.conbuildmat.2013.02.070`

[10] Nakbanpote, W., Goodman, B. A., & Thiravetyan, P. (2007). Copper adsorption on rice husk derived materials studied by EPR and FTIR. Colloids and Surfaces A: Physicochemical and Engineering Aspects, 304(1–3), 7–13. `https://doi.org/10.1016/j.colsurfa.2007.04.013`

[11] Liou, T.-H. (2004). Preparation and characterization of nano-structured silica from rice husk. Materials Science and Engineering: A, 364(1–2), 313–323. `https://doi.org/10.1016/j.msea.2003.08.045`

[12] Yalcin, Y., Kilic, M., & Cinar, Z. (2010). The Role of Non-Metal Doping in TiO2 Photocatalysis. Journal of Advanced Oxidation Technologies, 13(3), 281–296. `https://doi.org/10.1515/jaots-2010-0306`

[13] Sankar, S., Sharma, S. K., Kaur, N., Lee, B., Kim, D. Y., Lee, S., & Jung, H. (2016). Biogenerated silica nanoparticles synthesized from sticky, red, and brown rice husk ashes by a chemical method. Ceramics International, 42(4), 4875–4885. `https://doi.org/10.1016/j.ceramint.2015.11.172`

[14] Hello, K. M., Hasan, H. R., Sauodi, M. H., & Morgen, P. (2014). Cellulose hydrolysis over silica modified with chlorosulphonic acid in one pot synthesis. Applied Catalysis A: General, 475, 226–234. `https://doi.org/10.1016/j.apcata.2014.01.035`

[15] Haensel T., Comouth A., Lorenz P., Ahmed, S. I. U., Krischok, S., Zydziak, N., Kauffmann, A., & Schaefer, J. A. (2009) Pyrolysis of cellulose and lignin. Appl. Surf. Sci. 255, 8183–8189.

[16] Sgriccia, N., Hawley, M. C., & Misra, M. (2008). Characterization of natural fiber surfaces and natural fiber composites. Composites Part A: Applied Science and Manufacturing, 39(10), 1632–1637. `https://doi.org/10.1016/j.compositesa.2008.07.007`

Energy Storage Performance Analysis of Fuel Cells and Supercapacitors with Material Characteristics

Umut Yagcioglu
yagcioglu93umut@gmail.com, Department Energy Systems Engineering, Ankara Yildirim Beyazit University, Ankara, Turkey

Abstract

This study provides better knowledge to understand the energy storage performance analysis of fuel cells and supercapacitors with material characteristics. In today's world, certain forms of energy are utilized everywhere such as in lighting, heating, running of machines and storing of appliances, etc. Energy demand increases gradually with increasing the human population. Therefore, energy supplying and energy storing are significant processes pertinent to each other. One of the most important parameters for energy storage issue is the examination and development of material properties used energy storage devices. Developments and investments in energy storage process must keep pace with the energy demands. There are many problems which are faced by fuel cells and supercapacitors such as low energy density, production cost, low voltage per cell and high self-discharge, etc. To overcome these types of problems, novel materials need to be improved for them. In order to improve their performances and efficiencies, electrochemical properties must be scrutinized in terms of electrode materials and designed by following some technological processes.

Keywords: Energy Storage, Material Characteristics, Fuel Cells, Supercapacitors.

Introduction

Energy has become one of the most important requirements all over the world. Economic and technological developments are directly related to the energy sources. Fossil fuels are rapidly depleted due to the increasing in the population, industrial improvements, and produce greenhouse gases and cause climate change. This situation leads to be found out renewable energy sources. But, they can vary from location of country to another and can not be predicted. Therefore, scientists are attaching importance to the energy storage devices. Energy storage will contribute to reduce the energy problem. These devices refer to store energy produced at a certain time for later use. Fuel cell is an energy storage device that converts chemical energy of a fuel such as hydrogen, methanol etc. into electrical energy without combustion. Fuel cells use hydrogen and oxygen in the air as fuel source. Supercapacitor is an energy storage device that can have larger capacitance and store much higher energy than other type of capacitors. Fuel cells and supercapacitors are most preferred energy storage devices because of their large fuel conversion efficiency, quiet operation, their low-cost, environmental friendly and their ability of higher energy storage.

Research Findings

The Used Materials In Fuel Cells

Graphene:

Graphene exhibits outstanding properties like large conversion efficiency, high power delivery, low-cost, large chemical stability and electrochemical activity, long life span, working safely. Graphene is carbon allotrope and composes of sp^2-hybridized carbons.

Table 1: Properties of graphene [1]

Optical Absorbance (absorption of visible light)	2.3%
Electrical Conductivity	10^6S.cm^{-1}
Thermal Conductivity	3000Wm^{-1}K^{-1}
Theoretical Specific Capacity	744 mAh/g
Specific Capacitance	550 F/g
Charge Mobility	230000 cm^2/V.s
Breaking Strength	42 N/m
Young Modulus	1 Tpa
Density	< 1gcm^{-3} in 2630m^{2}g^{-1}
Theoretical Specific Surface Area	2600 m^2/g

Graphene has 2 dimensional structure. Carbon atoms are located in a hexagonal design. Graphene nanostructure contains an atom thick layer of graphite that has approximately thickness of 0.34 nm. Each carbon atom has covalent bonds with three other carbon atoms. Because of the durability of the covalent bonds between carbon atoms, they prove the stability and tensile strength of the graphene. Graphene has higher electron mobility than other materials, excellent electronic properties. The electronic conductivity of the graphene is proportional to the quality of the graphene. Defect density of its crystal lattice must be low in order to improve the quality of graphene. Graphene is conducts electricity and heat very well.

Perovskites Based Electrodes (ABO_3):

This material improves the kinetics of reactions in electrodes with temperature and is also low-cost. This material is known as Calcium Titanium Oxide mineral. Perovskites are abundant, large absorption coefficient, superconductivity, charge ordering, colossal magnetoresistance, large thermopower, long-range ambipolar charge transport, low exciton-binding energy, large dielectric constant, ferroelectric properties.

Porous Ni/YSZ Cermet:

This material is used as anode material because of its low-cost, good chemical stability, excellent electrical conductor and possess large corrosion resistance to the fuel. Usage of only Ni particles leads to anode degradation. In order to prevent this problem, Ni particles are combined with YSZ (Yttria-stabilized zirconia).

Table 2: Comparison of thermal expansion coefficient between Nickel and YSZ [2]

Materials	**Thermal Expansion Coefficient (TEC)** (K^{-1})
Nickel	16.9*10$^{-6}K^{-1}$
YSZ	11.0*10$^{-6}K^{-1}$

Cermet is obtained by combining ceramic (cer) material with metal (met). The most important properties of cermet are high temperature resistance, strength and hardness. Porous Ni/YSZ cermet exhibits closer TEC with that of YSZ electrolyte. The porous structure contributes to carry out diffusion and permeation for fuel gas. The electrical conductivity of Ni/YSZ cermet anode depends on nickel content and size ratio between YSZ and Ni. Electrical conductivity is proportional to the nickel content and size ratio.

$LaMnO_3$ (Lanthanum Manganite):

This material is most widely used as cathode materials because of the excellent and valanced consideration of electrical conductivity, chemical reactivity electrocatalytic activity, and TEC. Lanthanum manganite is an inorganic compound and a type of perovskites. The main reason of notation of $LaMnO_{3-\delta}$ is that $LaMnO_3$ possesses often Lanthanum vacancies and neutron scattering occurs.

Table 3: Properties of Sr-doped Lanthanum Manganite [2]

	TEC (x10^{-6}K^{-1})	œ$_{\text{e}}$(Scm^{-1})
La$_{0.6}$Sr$_{0.4}$MnO$_{3-\text{ffi}}$	13 (800)	130
La$_{0.7}$Sr$_{0.3}$MnO$_{3-\text{ffi}}$	12.8 (25-1100)	265 (947)

Cobalt-Based Electrodes:

These materials present more excellent and higher ionic and electronic conductivities than other materials. Moreover, these materials exhibit also high thermal expansion coefficient. Sr-doped $La_{0.6}Sr_{0.4}CoO_3$ presents the highest electrical conductivity of $\sigma = 4.4\text{x}10^3$ S.cm^{-1}.

The Used Materials In Supercapacitors

Activated Carbon (AC):

This material can be used in Electrical Double Layer Capacitors as electrode because of their high surface area, excellent electrical properties, good electrochemical performance, low-cost, and perfect oxidizing behaviour. AC provides a good management of pore sizes that can change from lower 5 nm to larger than 50 nm. Therefore, both ion size and pore size of electrolyte must be compatible with each other in order to obtain excellent electrochemical performance in a capacitor. AC are produced from many substances that include a large carbon content like coal, wood. AC contains the strongest physical adsorption forces and the largest volume of adsorbing porosity. It can also possess a surface that is larger than 1000 m^2/g. AC exhibits various physiochemical properties with good improved surface areas that reach to 3000 m^2/g [3]. There are three types of porous structure of AC and these structures are produced from activation processes. Porous structure of AC contain micropores (<2 nm), mesopores (2–50 nm) and macropores (>50 nm) [3].

Table 4: Specific capacitances of activated carbon in different electrolytes [4]

Electrolytes	**Specific capacitances of AC** (Fg^{-1})
Aqueous Electrolytes	Between 100 and 200 F/g
Organic Electrolytes	50 and 150 F/g
Aqueous Electrolytes (with KOH-treated AC)	160 and 225 F/g

Carbon Nanotubes (CNTs):

CNTs can be classified into two types; Single walled carbon nanotubes (SWCNTs) and multi-walled carbon nanotubes (MWCNTs). CNTs exhibit good properties like high specific capacitance, stability under large current loads, low internal resistance, excellent pore structure, perfect mechanical and thermal stability, good electrical properties, excellent tensile strength and thermal conductivity, light weight, intrinsic flexibility, large surface area (1600 m^2g^{-1}), and excellent electrical conductivity (105 $S.cm^{-1}$) [5]. These materials are produced by rolling up graphene. The conductivity in CNTs is provided by making use of ballistic transport. In this transport, charge carriers possess a very large mean free path and face no scattering [6]. SWCNTs possess an excellent flexibility and large surface area with the sizes of 5 nm. MWCNTs have also higher defects in their structure than that of SWCNTs. This situation can also lead to alter their structure. CNTs are the most strongest materials in terms of tensile strength and elastic modules because of the covalent sp^2 bonds. CNTs possess also mesopores which are interconnected. The specific capacitance of CNTs is between 15 and 200 F/g [4].

Table 5: The properties of CNTs [7]

	Properties
Density For A Solid	1.3 to 1.4 g/cm^3
Specific Strength	48,000 $kNmkg^{-1}$
Strength (Individual CNT Shells)	100 gigapascals (15,000,000 psi)
Electric current density (metallic nanotubes)	410^9 A/cm^2
Thermal conductivity (an individual SWNT)	3500 $Wm^{-1}K^{-1}$

Conducting Polymers (CPs):

CPs are used as electrode material because of their low-cost, simple production, excellent conductivity and higher capacitance than carbon-based electrode materials. Conducting polymers provide the conduction of electricity via a conjugated band matrix. They display also larger energy density than metal oxides.

Aqueous Electrolyte:

This electrolyte is used as electrolyte materials because of its low-cost and abundance. H_2SO_4, KOH, and KCl are the most preferred aqueous electrolytes.

Table 6: Properties of different types of electrolytes [4]

Electrolyte	**Density** (g/cm^3)	**Resistivity** (Ωcm)	**Cell Voltage (V)**
KOH	1.29	1.9	1
Sulfuric Acid	1.2	1.35	1
Propylene Carbonate	1.2	52	2.5–3
Acetonitrile	0.78	18	2.5–3
Ionic liquids	1.3–1.5	125 ($25°C$) 28 ($100°C$)	3.25-4

Aqueous electrolyte exhibits usually excellent conductivity (e.g., 0.8 $S.cm^{-2}$ for 1 M H_2SO_4 at 25 °C) [5]. The main purposes of electrolytes in supercapacitor is to prevent leakage, increase capacitance and provide easy handling. In order to achieve these purposes, Aqueous electrolytes can be modified by combining with different gels in order to obtain an excellent stable electrolytic system. Wang et al. soaked polyacrylamide gel (PAM-G) into a aqueous solution of 6 M KOH for about 60 h and they obtained electrolytic system with perfect cycling stability, rate capability, and high specific capacitance (196 Fg^{-1} at GCD (Galvanostatic charge discharge) 1 Ag^{-1}) [5].

Ionic Liquids (ILs):

Organic electrolytes have not become potential candidates for supercapacitors at temperatures that are higher than 70 °C due to their low ignition and detonation temperatures [5]. Boiling temperature of water has a great affect on aqueous electrolytes in terms of limitation of usage of aqueous electrolytes. Supercapacitors can not significantly make use of aqueous electrolyte above 80 °C. Therefore, ILs have become one of the most preferable electrolyte materials for supercapacitors at very high temperatures due to their high chemical and thermal stabilities, with wide working voltage ranges, negligible vapour pressure, and non-flammability. ILs consist of solvent-free molten salts in liquid form at room temperature that is because of their low melting temperatures. They are non-toxic, non-flammable and present also the widest voltage window (0 to 3-5 V), lack of thermal or chemical instability. These electrolytes have also large chemical and thermal stabilities with wide operating voltage ranges. ILs can also be heated up to 300 °C and any vaporization does not take place [4].

Organic Electrolyte:

This electrolyte has become one of the most useful materials due to their large working electric potential window. Main purpose of usage organic electrolytes is to provide the utilization of cheap materials as current collectors and packages. The organic electrolytes is one of the most outstanding conductive salts like tetraethylammonium tetrafluoroborate ($TEABF_4$).

Transition Metal Oxides (TMOs):

Manganese Oxide (MnO_2): This material is used as electrode material due to its good physical and chemical properties, high specific capacitance, low-cost, environmental friendliness, abundant reserve, high capacitive performance in aqueous electrolytes.

Table 7: Specific capacitances of different manganese oxide materials [8]

Materials	**Specific Capacitance** (Fg^{-1})
$Li - Mn_{1-x}Ru_xO_2$	$360Fg^{-1}$
MnO_2@GCs@MnO_2	390 Fg^{-1} at 0.5 Ag^{-1} in 6 M KOH electrolyte
Hollow MnO_2 nanospheres	299 Fg^{-1} at 5 mVs^{-1}
Mn_3O_4	261 Fg^{-1}
The MnO_2 electrode	178 Fg^{-1} at 5 mVs^{-1}

Ruthenium oxide (RuO_2): Ruthenium oxide is an inorganic compound and is the most used electrode material due to its high conductivity, large thermal stability [8]. They have long life cycle and good reversibility.

$RuO_2 + xH^+ + xe^- = RuO_{2-x}(OH)_x$ (0<x<2) (Energy storage mechanism of RuO_2) [8]

Table 8: Specific capacitances of different types of RuO_2 [8]

Material	**Specific Capacitance** (Fg^{-1})
Anhydrous RuO_2	24 Fg^{-1}
Hydrated $RuO_20.5H_2O$	342 Fg^{-1}
Amorphous RuO_2	1580 Fg^{-1}

Results and Conclusions

This paper consists of four parts. In introduction part, general information about fuel cells and supercapacitors are described like definition of these energy storage devices. In the second part, the used materials in fuel cells and their properties are explained and in the third part, the used materials in supercapacitors and their properties are given. In conclusion part, the obtained results are indicated. Briefly, the main purpose of this paper is to give information about fuel cells, supercapacitors and the used materials in them. According to the performances and properties of used materials in fuel cells and supercapacitors, these energy storage devices present outstanding advantages for future power generation plants and many applications. Additionally, they offer cleaner, more sustainable and reliable power generation source. High-quality materials were utilized in fuel cells and supercapacitors in order to improve their performance, be low-cost and provide more usage in future applications. These used materials provide excellent electronic conductivity and contribute to improve their durability. Conducting polymers exhibit large specific capacitance. Graphene presents a great advantage for fuel cells. Metal-oxide base supercapacitive electrodes provide improvement of the capacitance of supercapacitors. Each of metal oxides materials presents larger energy density than carbon-based materials with Electrical Double Layer Capacitance (EDLC). But MO-based exhibits sometimes low conductivity and slow ion transfer and this situation leads to some important problems that are related to cycle stability.

Acknowledgements

I would like to express my sincere gratitude to my supervisor, Assoc. Prof. Dr. Metin AKTAS who helped me to prepare my thesis project of "Energy Storage Performance Analysis of Fuel Cells and Supercapacitors with Material Characteristics".

Secondly, I would also like to thank you who held this conference and selected me for this conference.

References

[1] Hossain, S., Abdalla, A. M., Suhaili, S. B. H., Kamal, I., Shaikh, S. P. S., Dawood, M. K., & Azad, A. K. (2020b). Nanostructured graphene materials utilization in fuel cells and batteries: A review. Journal of Energy Storage, 29, 101386. `https://doi.org/10.1016/j.est.2020.101386`

[2] A., H., F. Santos, J. A., Z., R., & Matencio, T. (2011). Ceramic Materials for Solid Oxide Fuel Cells. Advances in Ceramics - Synthesis and Characterization, Processing and Specific Applications, 423–446. `https://doi.org/10.5772/18297`

[3] S. Iro, Z. (2016). A Brief Review on Electrode Materials for Supercapacitor. International Journal of Electrochemical Science, 10628–10643. `https://doi.org/10.20964/2016.12.50`

[4] Kim, B. K., Sy, S., Yu, A., & Zhang, J. (2015). Electrochemical Supercapacitors for Energy Storage and Conversion. Handbook of Clean Energy Systems, 1–25. `https://doi.org/10.1002/9781118991978.hces112`

[5] Raza, W., Ali, F., Raza, N., Luo, Y., Kim, K.-H., Yang, J., Kumar, S., Mehmood, A., & Kwon, E. E. (2018). Recent advancements in supercapacitor technology. Nano Energy, 52, 441–473. `https://doi.org/10.1016/j.nanoen.2018.08.013`

[6] Najib, S., & Erdem, E. (2019). Current progress achieved in novel materials for supercapacitor electrodes: mini review. Nanoscale Advances, 1(8), 2817–2827. `https://doi.org/10.1039/c9na00345b`

[7] Wikipedia contributors. (2020, September 7). Carbon nanotube. Wikipedia. `https://en.wikipedia.org/wiki/Carbon_nanotube` Last Access: 19.09.2020

[8] Dr. Zhang, J., Dr. Cui, Y., Prof. Dr. Shan G. (2019). Metal oxide nanomaterials for pseudocapacitors. arXiv:1905.01766. `https://arxiv.org/abs/1905.01766` [physics.app-ph]

Analysis of the Seasonal Energy Production of a Sample Wind Turbine

Deniz Yilmaz
denizyilmaz@arel.edu.tr, Department of Mechanical Engineering, Istanbul Arel University, Istanbul, Turkey.

Abstract

Wind energy offers many advantages as one of the fastest growing energy sources in the world. Research efforts are aimed at solving the challenges to greater use of wind energy. In order to ensure the widespread use of wind energy, which is one of the renewable energy resources, it is necessary to research, areas with high wind potential and to encourage the use of wind energy in these areas. In this study, one-year energy production data of a sample turbine is analysed depending on wind speeds. Energy production data was collected for each month during a year and the annual energy production graph was created using the wind speed data collected from site. As a result of these investigations, it was determined that the most efficient period is winter. Beside this, there was a difference of more than 3.5 times between the maximum amount of energy produced in December and the minimum amount of energy produced in April.

Keywords: Wind energy, wind turbine, energy analysis.

Introduction

The importance of renewable energy sources is better understood when considering the limited usage periods of fossil fuels that meet a significant part of the world energy needs, the damage to the environment during the energy acquisition and the energy needs of the future generations. The widespread and wide-scale use of these resources depends on technological developments and the creation of a national and international information network that will determine the potential. One of the alternative energy sources that should be considered in the first place is wind energy. Wind energy source is one of the fastest growing sources of renewable energy sources. The installed capacity of wind power has increased in day by day. According to the World Wind Energy Association total capacity for wind energy globally is now over 651 GW, an increase of 10 per cent compared to 2018 [1]. Detailed information on wind energy has been studied extensively in the literature [2–9]. Studies on wind energy in the literature cover different areas; wind speed estimates [10–13], aerodynamic studies to increase energy production from wind [13–16], wind power generation potentials for different countries and regions [17–20] and wind farm investment decision analysis [21–24].

In this study, 20 wind turbines with similar characteristics and capacities were selected from a Wind Power Plant in the Eastern Thrace Region. Eastern Thrace Region located in the north-western Turkey and covering an area of more than 6000 square kilometres. Elevations of most land in this region range from 100 to 500 m above sea level (see Figure 1).

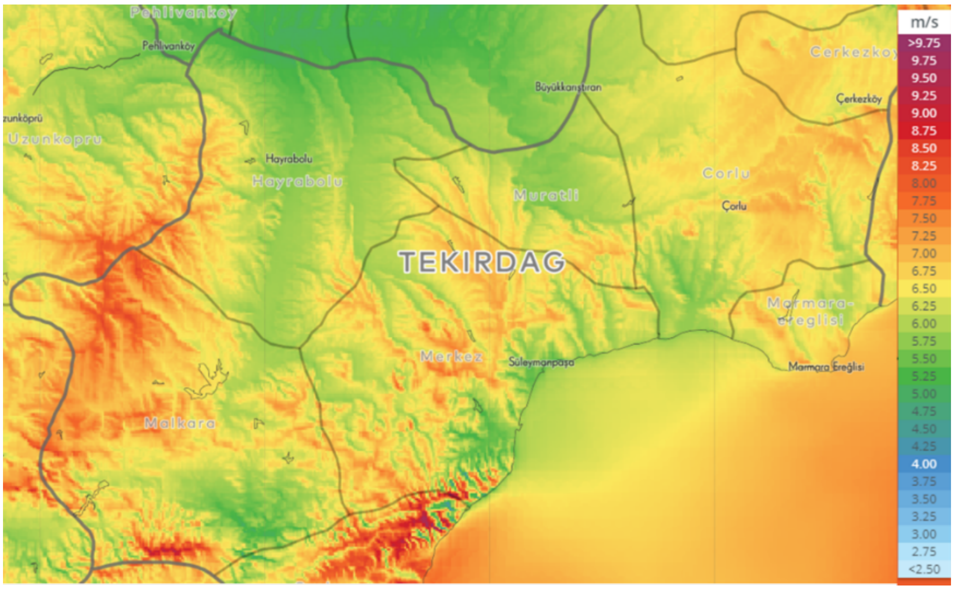

Figure 1: Map of the mean wind speed for the Eastern Thrace Region. (https://globalwindatlas.info/area/Turkey).

The researched wind power plant has Siemens 3.2 direct drive gearbox model turbines. For these types of wind turbines cut in speed is 3 m/s and cut out speed is 25 m/s. Since there is no belt and pulley, vibration is less and accordingly it is silent and durable. Power transfer is easy in these systems, which saves energy. The length of the turbines is 115 m and the wing length is 55 m. Their capacities are 3.2 MW. Number of blades is 3.

All data in the wind power plant were recorded hourly and 1-year real-time data was collected from the recording system. The energy obtained from the turbines was examined monthly and evaluated depending on the wind speed.

Results and Discussion

Monthly energy production for the sample turbine is presented in Figure 2. When the data obtained depending on the wind speed are examined, it is seen that the highest energy generation is in December.

Wind speed is the most effective parameter on the energy produced. As can be seen from the equation, power varies with the cube of wind speed. It is the energy obtained from wind turbines. The wind power available per unit area swept by the turbine blades is given as the following equation:

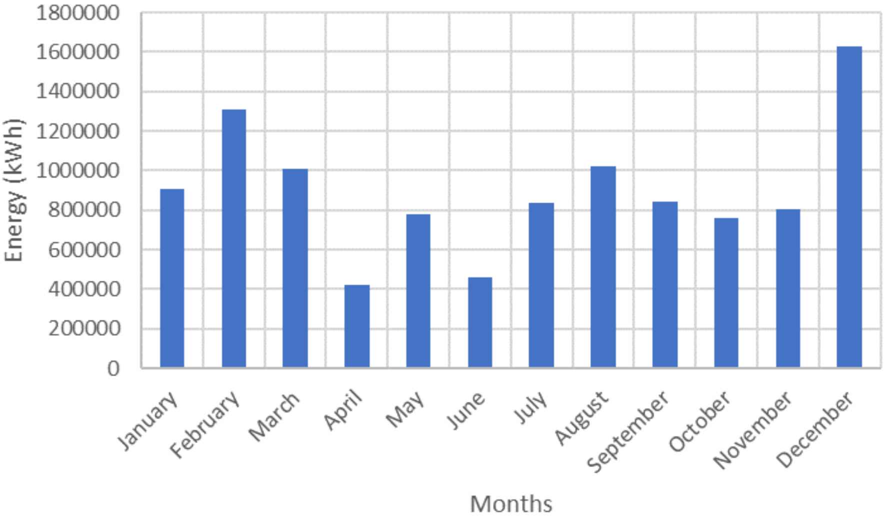

Figure 2: Histogram of the monthly produced energy distribution.

$$P = \frac{1}{2}\rho C_p \Sigma(V_i^3 t_i) \tag{1}$$

Where ρ is the air density, V_i is the mean wind speed for the i^{th} time interval, t_i the number of hours corresponding to the time interval divided by the total number of hours and C_p is a power coefficient. Annual energy production depending on average speeds is also shown in the Figure 3. For the minimum measured average velocity of 4.71 m/s, the monthly energy production obtained is 418,000 kWh, while the monthly energy production obtained for the maximum measured average velocity of 9.41 meter per second is approximately 1 600 000 kWh. As can be seen from the graph, the change of generating energy depending on the change in wind speed is almost linear.

When we examine the average wind speeds measured by months, it is seen that the speeds are high during the winter months (see Figure 4). And august follows the winter season. August winds are a characteristic feature of the region.

The variation of the capacity factor with wind speed is given in Figure 5. The highest monthly mean wind speeds occur during the months of winter with a maximum occurring in December. Generally, lower wind speeds are observed in the June. Figure 6 shows the change in monthly average wind speed during June, when the minimum daily variation of wind speed throughout the year, and December, when the maximum daily change in wind speed throughout the year was observed. The average wind speed during June was found to be 4.91 m/s and 10.15 m/s during December.

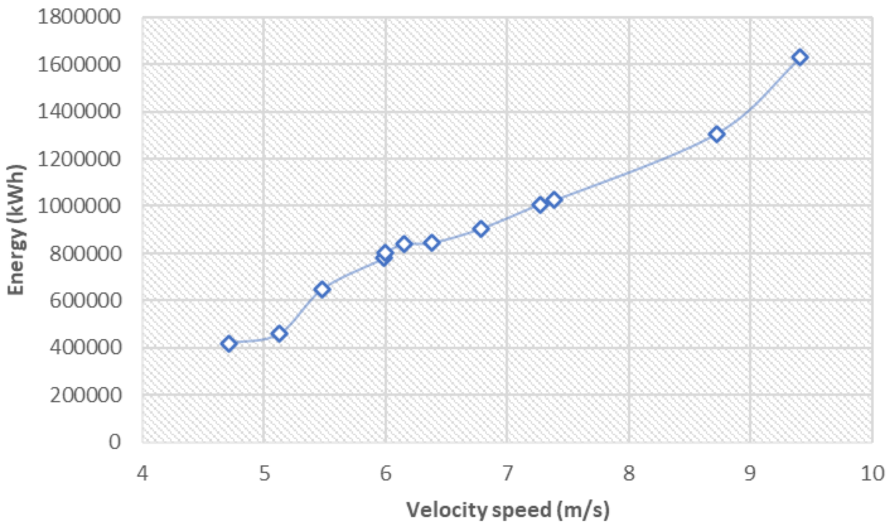

Figure 3: Change of monthly energy production depending on wind speed.

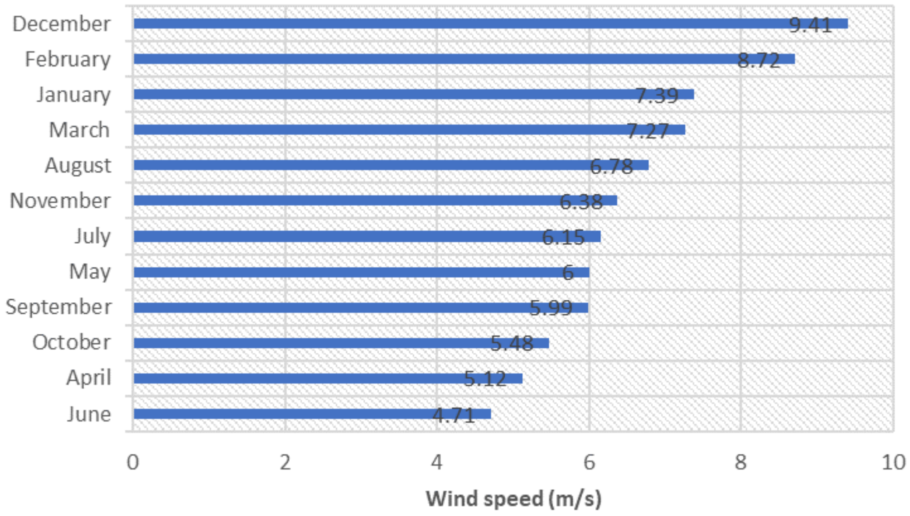

Figure 4: Annual average wind speed values by months.

Conclusions

Wind power electricity energy generation in the world is growing rapidly. In order to achieve environmentally benign sustainable energy programs, renewable energy sources should be promoted in every stage. The calculations of the mean values of the wind speeds 1 year and the daily, monthly, and annual mean of the extractable wind energy by turbines give an idea of the wind potential available in the Eastern Thrace Region Turkey. The values of the mean wind energy available are between 400 000 kWh (April and June) and 1 600 000 kWh (December).

In this study, potential of the produced energy of wind turbines was investigated for the selected site detailed knowledge of the wind characteristics, such as speed,

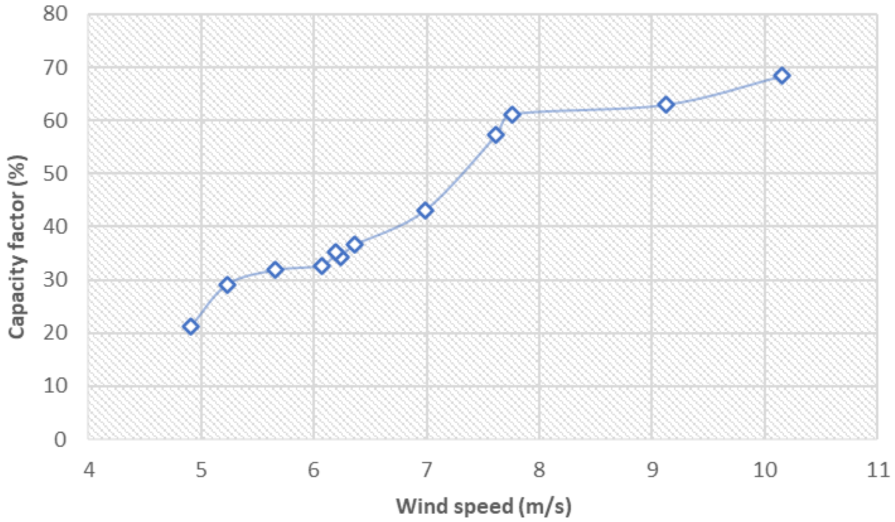

Figure 5: Capacity factors versus wind speed.

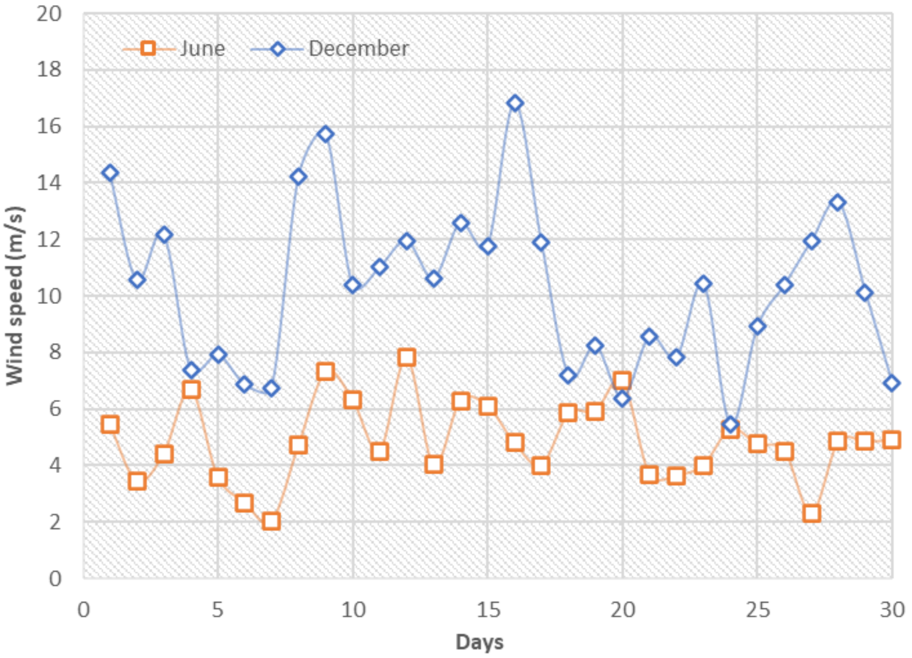

Figure 6: Variation of wind speed during June and December.

direction, and continuity. Also, wind speed changes were determined on a monthly and annual basis. There is about 2 times the difference between December when the average wind speed is maximum and June when it is minimum. Wind speeds vary widely within a month. The highest changes occur in December, while the least changes are in June.

References

[1] Maxwell J.C., A Treatise on Electricity and Magnetism, 3rd ed., vol. 2. Oxford:Clarendon Press, 68-73, 1892.

[2] Poor, V. H. (1985). An Introduction to Signal Detection and Estimation (Springer Texts in Electrical Engineering) (2nd ed.). Springer.

[3] Yorozu, T., Hirano, M., Oka, K., & Tagawa, Y. (1987). Electron Spectroscopy Studies on Magneto-Optical Media and Plastic Substrate Interface. IEEE Translation Journal on Magnetics in Japan, 2(8), 740–741. `https://doi.org/10.1109/tjmj.1987.4549593`

[4] Kabalci, E., Irmak, E., & Colak, I. (2010). Design of an AC-DC-AC converter for wind turbines. International Journal of Energy Research, 35(2), 169–175. `https://doi.org/10.1002/er.1770`

[5] Colak I., Kabalci E., Bayindir R., & Sagiroglu S., “The design and analysis of a 5-level cascaded voltage source inverter with low THD”, 2nd PowerEng Conference, Lisbon, pp. 575-580, 18-20 March 2009

[6] GWEC. Global wind report. Global Wind Energy Council; 2019.

[7] Pasqualetti, M., & Stremke, S. (2018). Energy landscapes in a crowded world: A first typology of origins and expressions. Energy Research & Social Science, 36, 94–105. `https://doi.org/10.1016/j.erss.2017.09.030`

[8] Gibbons S., “Gone with the wind: valuing the visual impacts of wind turbines through house prices”, J Environ Econ Manage, 72, 177–196, 2015. `https://doi.org/10.1016/J.JEEM.2015.04.006`

[9] Rand J., Hoen B.B., “Thirty years of North American wind energy acceptance research: What have we learned?”, Energy Res Soc Sci, 29, 135–148, 2017. `https://doi.org/10.1016/j.erss.2017.05.019`

[10] Dimitropoulos A., Kontoleon A., ”Assessing the determinants of local acceptability of wind-farm investment: a choice experiment in the Greek Aegean Islands”, Energy Policy, 37 (5), 1842–1854, 2009. `https://doi.org/10.1016/j.enpol.2009.01.002`

[11] Georgiou I., Francisco A., ”A real economic valuation of an offshore wind farm in Greece: the role of individual’s base-state influences and beliefs in the value formation process”, Renew Sustain Energy Rev, 52, 717–724, 2015. `https://doi.org/10.1016/j.rser.2015.07.178`

[12] Margarita V, Eva L, Dimitra GV., “GIS-based multi-criteria decision analysis for site selection of hybrid offshore wind and wave energy systems in Greece”, Renew Sustain Energy Rev, 73, 745–57, 2017. `https://doi.org/10.1016/j.rser.2017.01.161`

[13] Kotroni, V., Lagouvardos, K., Lykoudis, S., “High-resolution model-based wind atlas for Greece”, Renew Sustain Energy Rev, 30, 479-489, 2014. `https://proxy.arel.edu.tr:2072/10.1016/j.rser.2013.10.016`

[14] Strazzera E., Mura M., Contu D., “Combining choice experiments with psychometric scales to assess the social acceptability of wind energy projects: a latent class approach”, Energy Policy, 48, 334–347, 2012. `https://doi.org/10.1016/j.enpol.2012.05.037`

[15] Tascikaraoglu, A., Uzunoglu, M., “A review of combined approaches for prediction of short-term wind speed and power”, Renew Sustain Energy Rev, 34, 243-254, 2014. `https://proxy.arel.edu.tr:2072/10.1016/j.rser.2014.03.033`

[16] Tian, Z., “Short-term wind speed prediction based on LMD and improved FA optimized combined kernel function LSSVM. Engineering Applications of Artificial Intelligence”, 91, 103573, 2020. `https://proxy.arel.edu.tr:2072/10.1016/j.engappai.2020.103573`

[17] Ma, Z., Chen, H., Wang, J., Yang, X., Yan, R., Jia, J., Xu, W. Application of hybrid model based on double decomposition, error correction and deep learning in short-term wind speed prediction. Energy Convers Manage, 205:112345, 2020. `https://proxy.arel.edu.tr:2072/10.1016/j.enconman.2019.112345`

[18] Wei, X., Huang, B., Liu, P., Kanemoto, T., Wang, L., “Experimental investigation into the effects of blade pitch angle and axial distance on the performance of a counter-rotating tidal turbine”, Ocean Engineering, 110, 78-88, 2015. `https://proxy.arel.edu.tr:2072/10.1016/j.oceaneng.2015.10.010`

[19] Shen, X., Zhu, X., Du, Z., “Wind turbine aerodynamics and loads control in wind shear flow”, Energy, 36(3), 1424-1434, 2011. `https://doi.org/10.1016/j.energy.2011.01.028`

[20] Hayat, K., Ha, S. K., “Load mitigation of wind turbine blade by aeroelastic tailoring via unbalanced laminates composites”, Composite Structures, 128, 122-133, 2015. `https://proxy.arel.edu.tr:2072/10.1016/j.compstruct.2015.03.042`

[21] Thé, J., Yu, H., ”A critical review on the simulations of wind turbine aerodynamics focusing on hybrid RANS-LES methods”, Energy, 138, 257-289, 2017. `https://doi.org/10.1016/j.energy.2017.07.028`

[22] Arslan, O., “Technoeconomic analysis of electricity generation from wind energy in Kutahya,Turkey”, Energy, 35(1), 120-131, 2010. `https://proxy.arel.edu.tr:2072/10.1016/j.energy.2009.09.002`

[23] Serri, L., Lembo, E., Airoldi, D., Gelli, C., Beccarello, M., “Wind energy plants repowering potential in Italy: technical-economic assessment”, Renew

Energy, 115, 382-390, 2018. `https://doi.org/10.1016/j.renene.2017.08.031`

[24] Fyrippis, I., Axaopoulos, P. J., Panayiotou, G., "Wind energy potential assessment in Naxos Island, Greece", App Energy, 87(2), 577-586, 2010. `https://doi.org/10.1016/j.apenergy.2009.05.031`

Author Index